Small-scale variability associated with mixing in the Denmark Strait Overflow plume based on horizontally profiling observations

Master-Arbeit

im

-Masterstudiengang (M.Sc.) Climate Physics-

Meteorology and Physical Oceanography

der Mathematisch-Naturwissenschaftlichen Fakultät

der Christian-Albrechts-Universität zu Kiel

vorgelegt von

Janin Schaffer

837969

Erstgutachter: Prof. Torsten Kanzow

Zweitgutachter: Prof. Claus Böning

Kiel, den 04.10.2013

Abstract

The Denmark Strait overflow (DSO) contributes roughly half of the total volume transport of the Nordic overflows. The overflows double their volume by entraining ambient water as they descend into the subpolar North Atlantic and feed the deep branch of the Atlantic Meridional Overturning Circulation. In summer 2012 a multi-platform experiment was carried out in the pathway of the DSO plume on the continental slope of Greenland near 30°W (180 km downstream of Denmark Strait), to observe variability on (sub-)meso- and small-scales associated with entrainment into the DSO plume

In this study the focus is set on the observations of small-scale variability by horizontal profiling with an autonomous underwater vehicle (AUV) in the transition layer between the DSO plume and the ambient water. The AUV measurement system provides hydrographic data and microstructure measurements with a horizontal resolution of 6.4 m. Observations show enhanced temperature and salinity variances within distinct segments on wavelength between 13 m and 500 m. These scales reach from the turbulent regime into the internal wave regime. Spectral analysis was applied to the AUV-based temperature data to separate these two regimes. Increased temperature variance is found on wavelength between 21 m and 210 m with a wavenumber-dependence characteristic of turbulence in the inertial-convective subrange. Within the same periods elevated turbulent dissipation of $O(10^{-6})\frac{W}{kg}$ is observed (compared with $O(10^{-9})\frac{W}{kg}$ in the ambient water). The variances in temperature and isotherm displacement from the regular AUV-CTD agree with the dissipation rates from microstructure measurements. Both small-scale variability on turbulent scales as well as high dissipation rates imply strong vertical mixing.

Two major turbulent events were captured by the AUV. The first was supposedly a stationary feature on the upstream side of a topographic elevation. The second was transient, and associated with processes near the edge of an energetic eddy. Large vertical shear of horizontal velocities and critical Ri numbers from ship-lowered CTD/LADCP profiles support the AUV-inferred strong vertical mixing. At the same time moored current meters indicate advection of ambient water towards the shelf. The observations imply that eddy-driven horizontal advection and vertical mixing go hand in hand in entraining ambient water into the DSO plume.

Zusammenfassung

Das über die Schwelle der Dänemark Straße fließende „Overflow“ - Wasser (DSO) trägt etwa zur Hälfte zum Gesamtvolumentransport der „Overflows“ aus dem Polaren Nordmeer bei. Beim Hinabsinken in den subpolaren Nord Atlantik verdoppeln die “Overflows“, durch das Einmischen von umliegendem Wasser, ihr Volumen und speisen so den tiefen Zweig der Atlantischen Umwälzzirkulation. Im Sommer 2012 wurde ein Experiment mit verschiedenen Messplattformen im Bereich des „DSO-Plume“ auf dem Grönländischen Kontinentalhang nahe 30°W (180 km stromabwärts der Schwelle) durchgeführt, um Variabilität auf Mesoskalen und kleineren Skalen zu messen, welche mit dem Einmischen von Wasser in den Plume verknüpft wird.

In dieser Arbeit liegt der Fokus auf Beobachtungen von klein-skaliger Variabilität, welche mit einem horizontal-messenden unabhängigen Unterwasser-Messgerät (AUV) in der Übergangsschicht zwischen dem „DSO-Plume“ und umliegendem Wasser erfasst wurden. Das AUV Messsystem stellt hydrografische Daten und Mikrostruktur-Messungen mit einer horizontalen Auflösung von 6.4 m bereit. Beobachtungen zeigen innerhalb bestimmter Segmente auf Wellenlängen zwischen 13 m bis 500 m verstärkte Varianzen in Temperatur und Salzgehalt. Diese Skalen reichen vom turbulenten Bereich bis in den Bereich interner Wellen. Mit Hilfe von Spektralanalyse der AUV Temperaturdaten ist es möglich beide Bereiche voneinander zu trennen. Hohe Temperatur-Fluktuationen wurde auf Wellenlängen zwischen 21 m und 210 m gemessen mit einer charakterischen Wellenzahl-Abhängigkeit für Turbulenz im inertial-konvektiven Unterbereichs. Innerhalb derselben Abschnitte wurden erhöhte turbulente Dissipationsraten der Ordnung $O(10^{-6})\frac{W}{kg}$ aufgezeichnet (verglichen mit $O(10^{-9})\frac{W}{kg}$ im umliegenden Wasser). Die Varianzen von Temperatur bzw. von der Auslenkung von Isothermen basierend auf Messungen mit der AUV-CTD sind vergleichbar mit Dissipationsraten von Mikrostruktur-Messungen. Sowohl klein-skalige Variabilität auf turbulenten Skalen als auch hohe Dissipationsraten implizieren eine starke vertikale Vermischung.

Zwei turbulente Hauptereignisse wurden vom AUV eingefangen. Es wird angenommen, dass das erste ein stationäres Merkmal auf der stromaufwärtigen Seite einer topographischen Erhöhung ist. Das zweite kurzzeitige Ereignis wurde mit Prozessen, die am

Rand von einem energiereichen Wirbel ablaufen, in Zusammenhang gebracht. Große vertikale Scherungen von horizontalen Geschwindigkeiten und kritische Richardson Zahlen, basierend auf vertikalen CTD/LADCP-Profilen, stützen die vom AUV angedeutete starke vertikale Vermischung. Daten aus verankerten Strömungsmessern weisen gleichzeitig auf ein laterales Heranführen von umliegendem Wasser zum Schelf hin. Diese Beobachtungen implizieren, dass eine wirbel-getriebene horizontale Advektion und vertikale Vermischung beim Einmischen von umliegendem Wasser in den „DSO-Plume“ miteinander verknüpft sind.

Contents

Chapter 1

Introduction

The Atlantic Meridional Overturning Circulation (AMOC) ventilates the deep ocean by transporting warm, salty water at the surface northward and cold and dense North Atlantic Deep Water (NADW) southward (e.g., *Schmittner et al.* (2007) and references therein). The main driver of the AMOC is the deep water formation in the Nordic Seas (*Schott et al.*, 2004) and the Labrador Sea (*Mauritzen*, 1996).

Convective processes govern the formation of dense water. In the ocean a vertical exchange of fluid between the surface and the abyssal ocean is inhibited by the strong vertical density gradient of the thermocline. Deep convection can be initialized only under certain conditions. Classical definitions state that strong atmospheric forcing, weak stratification below the surface mixed layer, and cyclonic circulation are the relevant preconditioning processes (*Marshall and Schott*, 1999). As a result of the cyclonic circulation the weakly stratified water is brought up to the surface. Thus the stratification can be eroded by buoyancy loss at the surface due to strong wind forcing. Such conditions are found during winter in the Labrador Sea and Greenland Sea (*Marshall and Schott* (1999) and references therein). Observations in the Labrador Sea showed that convective cells reach down to 2300 m water depth (*Schott and Brandt* (2007) and references therein). Although deep convection induces turbulent mixing on the sides of the convective plumes, it can not be understood as a vertical mass transport. It is probable, that only those convective regions found adjacent to steep topography play a role for the mass transport and thus for the downwelling limb of the AMOC (*Schott and Brandt* (2007) and references therein).

The cold and dense deep water which originates from the Nordic Seas is shielded towards the North Atlantic by land and bottom topography (see map in Fig. 1.1). In order to exit the Nordic Seas dense water needs to overflow the sill regions of the Greenland-Scotland ridge. The overflows play an important role in driving the deep circulation in the North Atlantic and are hydraulically controlled (e.g. *Quadfasel and Käse* (2007)

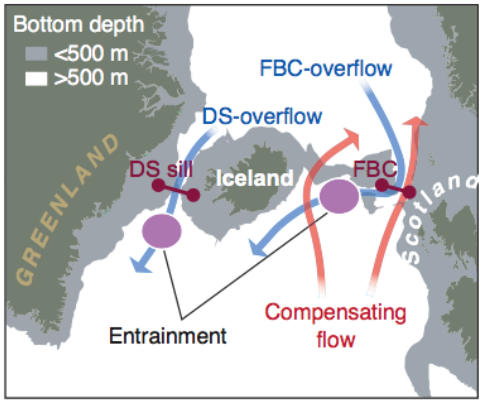

Figure 1.1: Sketch of the main overflows over the Greenland-Scotland Ridge. Marked are the locations of the Denmark Strait (DS) sill and the Faroe-Bank Channel (FBC) and the paths of the corresponding overflows. Highlighted in pink is the expected entrainment after the plumes descend from the sill. Grey colors indicate bottom depth < 500 m. From *Hansen et al.* (2004) (edited).

and references therein). The basic concept of hydraulic control (*Whitehead*, 1998) is sketched and described in Fig. 1.2 (left). In the Nordic Seas the flow conditions are critically controlled, especially at the sills of the Denmark Strait (DS) and at the Faroe-Bank Channel (FBC) (see Fig. 1.1). In this study the focus is set on the Denmark Strait Overflow (DSO) plume. Deep water formed by open-ocean deep convection in the Greenland Sea is largely shielded by the 640 m deep DS sill. Water of the density class found at the sill height can cross the sill. It slides down the sloping ocean topography as a relatively narrow dense gravity current (e.g. *Quadfasel and Käse* (2007) and references therein).

Compared to the internal Rossby radius the width of the DS is large and rotational effects are important. Consequently the DSO plume is banked against the Greenland slope. Near the DS sill the plume exhibits mainly a barotropic flow while further downstream (between 50 to 150 km) it undergoes a transition to a bottom-trapped baroclinic flow (*Käse et al.*, 2003). The DSO plume descends the Greenland continental slope and flows into the deep North Atlantic as Denmark Strait Overflow Water (DSOW). During its descent the maximal core density is reduced while the overall plume volume increases as shown for instance by numerical model simulations (*Käse et al.*, 2003), (see Figure 1.2, right). In a reduced gravity plume model rotation, friction, and entrainment are important to simulate the overflow plume dynamics (e.g. *Jungclaus and Backhaus* (1994)). Friction induces a stronger downslope velocity component while entrainment reduces the density contrast between the plume and the ambient water.

Here, entrainment is interpreted as the flux of momentum from ambient water into the plume by horizontal or vertical processes. Entrainment can be expressed by $E = \frac{w_E}{U_S}$ where w_E is the entrainment velocity and $U_S = \sqrt{U^2 + V^2}$ is the current speed (*Arneborg et al.*, 2007). The entrainment velocity is understood as the import of ambient water into the gravity current per unit area and time, expressed by

$$w_E = \frac{\partial H}{\partial t} + \frac{\partial UH}{\partial x} + \frac{\partial VH}{\partial y} \tag{1.1}$$

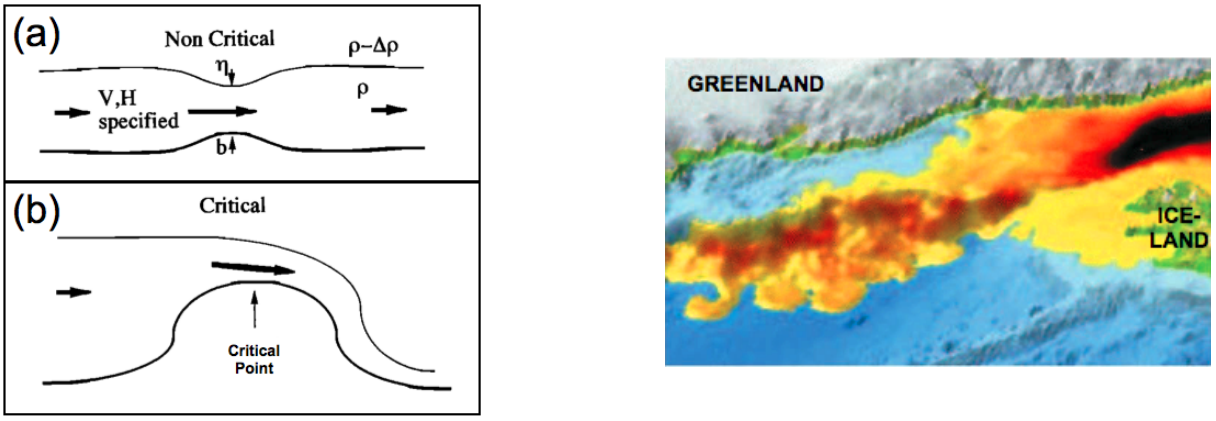

Figure 1.2: Left panel: The concept of hydraulic control. The upper panel (a) shows a frictionless fluid with velocity V and depth H that flows along a channel and encounters a bump with height b. Based on the conservation of volume the fluid is forced to speed up while passing the bump. This lowers the pressure and leads to a suppression of the free surface η. At a critical bump height this simple concept does not hold anymore because the surface would merge with the bump. Here, volume conservation is only achieved by either changing the velocity or the height of the flow. The lower panel (b) shows a hydraulically controlled overflow responding to a critical sill height. If dense water accumulates above the sill height, there is an outflow from one basin into the other. Above the sill, the flow height stays constant and the flow speeds up. When the flow enters the second basin it follows the sloping topography. Depending on its density it either stays at the level of equal density or spreads on the bottom of the basin. Steady state is achieved when the outflow rate equals the accumulation rate. From *Whitehead* (1998) (edited). Right panel: Modeled DSO plume bottom thickness. The color range yellow-red-black indicates the bottom layer thickness. It can be seen how the DSO plume slides down the Greenland continental slope. From *Käse et al.* (2003) (edited)

where H is the thickness of the plume (*Arneborg et al.*, 2007). For simplicity, the entrainment velocity is sometimes estimated by the rate of layer thickening due to entrainment (*Arneborg et al.*, 2007). Another approach separates the entrainment into isopycnal and diapycnal mixing parts. The isopycnal part of entrainment, the mixing along lines of constant density, implies a transport change in the absence of changes in density. Only entrainment based on diapycnal mixing, across lines of constant density, can cause both transport changes and density changes. Consequently entrainment by diapycnal mixing leads to a water mass transformation and can contribute to the downwelling limb of the AMOC. In general the two main entrainment mechanisms at the descending DSO plume are thought to be eddy-induced lateral fluxes and vertical fluxes driven by shear-instability at the upper interface of the plume (*Quadfasel and Käse*, 2007). The vertical fluxes act on length scales of meters to hundreds of meters, whereas the horizontal entrainment processes are relevant on horizontal length scales of several kilometers.

Eddy-induced lateral mixing is likely, due to meso-scale eddies observed downstream the DS sill (e.g., *Krauss and Käse* (1998)). Moored current measurements and temperature

records showed a high variability on time scales of 2 - 5 days close to the sill (*Bruce*, 1995) and 1 - 12 days about 500 km downstream from the DS sill (*Dickson and Brown*, 1994) associated with the passage of meso-scale eddies. Surface eddies observed in satellite

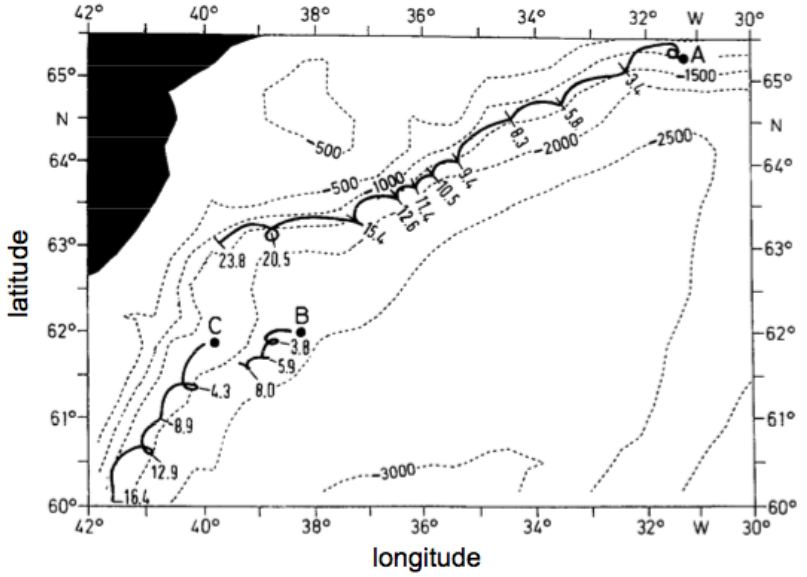

Figure 1.3: Trajectories of satellite-tracked buoys trapped in cyclonic eddies at the East Greenland continental slope. Tick marks give time in days. Dashed lines are bottom contours. From *Krauss* (1996).

altimetry (*Høyer and Quadfasel*, 2001) and by infrared imagery following drifters (*Bruce* (1995), *Krauss* (1996)) are supposed to be a surface manifestation of the variability in the deep plume (Fig. 1.3). The eddies have a diameter of 20 - 40 km, each throughout the whole water column and contain cold water (*Bruce* (1995), *Krauss* (1996)). The eddy formation is most probably caused by both vortex stretching and baroclinic instabilities of the shear flow (*Jungclaus et al.*, 2001). Vortex stretching is based on the theory that midlevel waters are stretched when the plume descends and the East Greenland Current (EGC) remains at the surface. This induces a very strong cyclonic relative vorticity (*Spall and Price*, 1997). Observations and modeling studies show that the DSO plume flows mainly between cyclonic and anticyclonic eddy chains (*Krauss and Käse* (1998), *Jungclaus et al.* (2001)). The anticyclonic eddies are found further to the shelf (upslope) and are expected to transport original overflow water (*Jungclaus et al.*, 2001). The cyclones, found on the offshore side (downslope), favor entrainment of ambient water (*Jungclaus et al.*, 2001). Consequently the cyclones are thicker and less dense.

In terms of water mass characteristics the DSOW represents the coldest and densest part of the NADW. In general, it is defined by densities with $\sigma_\Theta > 27.8\ \frac{kg}{m^3}$ and by potential temperatures of less than 2°C (e.g., *Quadfasel and Käse* (2007)). The DSOW is formed by various sources of the Nordic Seas (*Rudels et al.*, 2002). The main pathways to

reach the DS sill are the southward flowing EGC and currents of the Iceland Sea (*Rudels et al.* (2002), *Koehl* (2010)) (see map below in Fig. 1.5). Regarding the EGC two mixing products are light enough to cross the DS sill (*Rudels et al.*, 2002). The first mixing product is between Re-circulating Atlantic Water (RAW) and Arctic Atlantic Water (AAW). The second is between upper Polar Deep Water (uPDW) and Arctic Intermediate Water (AIW) from the Greenland Sea. These initial DSOW products are gradually homogenized by diapycnal mixing especially just north of the DS (*Rudels et al.*, 2002), where the EGC is encountered by the northward flowing Irminger current resulting in strong mixing of water from both components (*Rudels et al.* (2002), *Macrander et al.* (2007)). The different contributions from the EGC and the Iceland Sea to the DSOW are yet unknown and most likely vary in time depending on the atmospheric conditions (*Koehl*, 2010). Across the DS,

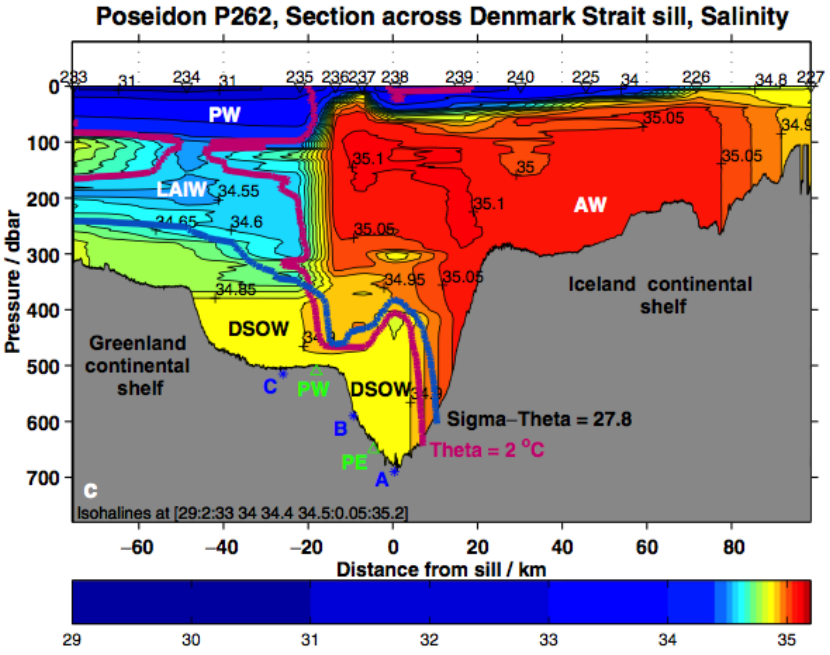

Figure 1.4: Salinity section across the DS in August 2002. The 2° isotherm and the 27.8 $\frac{kg}{m^3}$ isopycnal are indicated by the magenta and blue lines, respectively. Prominent water masses are labelled: Polar Water (PW), Lower Arctic Intermediate Water (LAIW), Atlantic Water (AW), and Denmark Strait Overflow Water(DSOW). From *Macrander et al.* (2007) (edited).

the DSOW covers the deepest parts (a 300 m thick layer) of the trough (Fig. 1.4). Two different water masses are identified above the DSOW. On the Icelandic side of the strait, warm, saline Atlantic water (AW) is found. On the Greenland side, cold, fresher water of polar origin covers the DSOW (Polar Water and Lower Arctic Intermediate Water, which is a typical mixing product of parts of the EGC and AW at the Icelandic shelf break (*Rudels et al.*, 2002)). The overflow characteristics in the descending DSO plume depend on the sources, their contributions, and the initial mixing in the plume. Additionally,

water entrained into the DSO plume changes the T/S[1]-characteristics. Entrainment of ambient water into the DSO plume was studied e.g., based on tracer analysis by *Tanhua et al.* (2005). In 1997 Middle Irminger Water (MIW) was found to be the most important water mass to entrain into the DSO plume between the sill and 350 km downstream of it (*Tanhua et al.*, 2005). MIW is characterized by an oxygen minimum and found at 1000 m to 1200 m deep on the Iceland slope. Further downstream Iceland-Scotland Overflow Water (ISOW) and Labrador Sea Water (LSW) are the most important water masses for entrainment (*Tanhua et al.*, 2005).

In general the DSO plume is found to be stratified and often covered by a low salinity lid (*Rudels et al.*, 1999). The low salinity lid is formed by Polar Intermediate Water (PIW), which is well-ventilated and originates most likely from the upper ($\Theta < 0\ ^\circ$) part of the Arctic ocean thermocline (*Rudels et al.*, 2002). It was observed at different sites close to the sill and even 200 km downstream. This indicates that entrainment of ambient water into the plume is not likely (*Rudels et al.*, 1999) or that entrainment is very patchy in time and space and allows the low salinity lids to survive in some places (*Dickson et al.*, 2008).

The assumption that entrainment plays a dominant role in the descending overflow plumes originates from classical transport studies. There are mainly two different methods to estimate entrainment in the descending DSO plume. The first is based on large scale observations of e.g. transport values or warming rates of the descending plume. The second are direct local measurements of turbulent motion by microstructure (MS) measurements to estimate the diapycnal part of entrainment. In the following all these methods will be introduced to give a better insight of both the role of entrainment and the different entrainment processes in the descending DSO plume.

Classical transport studies show that around 18 Sv ($1Sv = 10^6 \frac{m^3}{s}$) of NADW is transported southward from the subpolar North Atlantic in the lower limb of the AMOC (*Stahr and Sanford*, 1998). About one third originates from the Labrador Sea (*Schott et al.*, 2004), while the main sources of NADW are the dense overflow waters. The transport of DSOW and ISOW close to the sill is about 3 Sv each (*Schott and Brandt* (2007) and references therein). The Deep Western Boundary Current (DWBC) transport ($\sigma_\Theta > 27.8\ \frac{kg}{m^3}$) south of Greenland at Cape Farewell was estimated by Clarke in 1984 from hydrographic sections and a 60-day-long small array of current meters and amounts to 13 Sv (*Bacon and Saunders* (2010) and references therein). Based on the differences in the transport values of the overflows at the sills compared to those south of Greenland, it was assumed that strong entrainment doubles the plume transports (*Dickson and Brown*, 1994), (illustrated in Fig. 1.5). More recent studies based on a 10-month moored record

[1]T: temperature, S: salinity

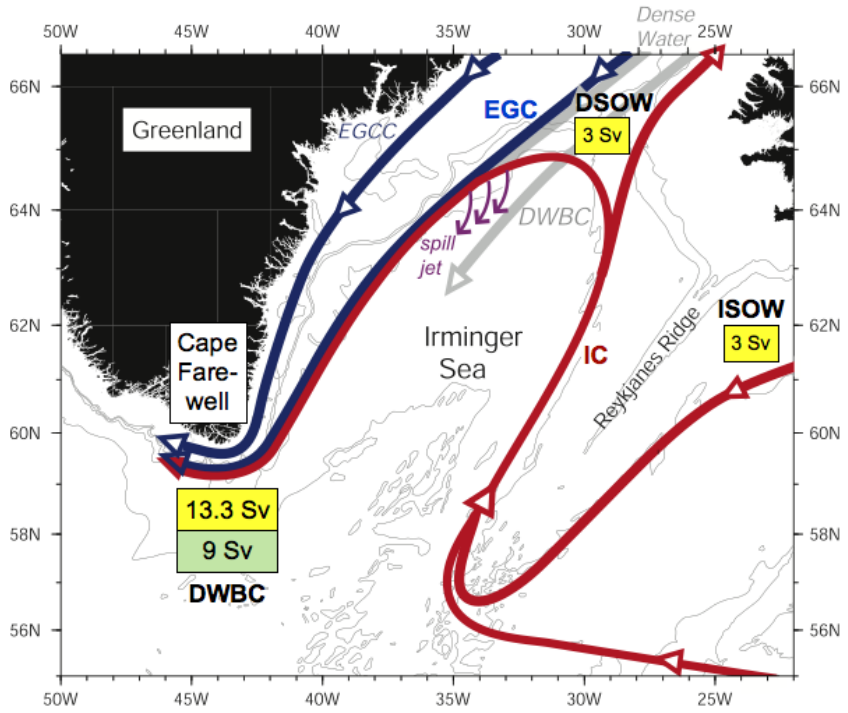

Figure 1.5: Sketch of the circulation and transports in the Irminger Sea. Given are the Irminger Current (IC) (red), the East Greenland Current (EGC) (blue), the East Greenland Coastal Current (EGCC) (blue), the East Greenland Spill Jet (purple) and the Deep Western Boundary Current (DWBC) (grey). Transport values in yellow are based on *Schott and Brandt* (2007), and in green based on *Bacon and Saunders* (2010). From *Brearley et al.* (2012) (edited).

in 2005/2006 at Cape Farewell yield a DWBC transport ($\sigma_\Theta > 27.8\ \frac{kg}{m^3}$) of only 9 Sv (*Bacon and Saunders*, 2010). This is also supported by transport studies along a section crossing the Irmiger Gyre. Herein the DWBC transport is estimated to be 9.6 ± 1.4 Sv (*Våge et al.*, 2011). The classical view, that entrainment increases DSOW by a factor of two, is reduced by the modern measurements (see Fig. 1.5).

Nevertheless, the ideal concept that water is entrained into the DSO plume on its way downstream from the sill is also implied based on warming rates of the plume. According to the findings of *Voet and Quadfasel* (2010), the heat budget from the overall plume warming rates cannot be closed by only eddy-driven lateral entrainment and Ekman pumping through bottom friction. The remaining heat is assumed to represent the effect of small-scale processes which cause diapycnal mixing like breaking internal waves. Following *Voet and Quadfasel* (2010) three different entrainment regimes can be defined. The regimes and their dominant entrainment mechanisms are illustrated in Fig. 1.6. The first regime (A) extends from the sill to about 125 km downstream. The barotropic structure of the overflow plume close to the sill implies little vertical turbulence. Here entrainment is estimated to be one order of magnitude smaller than further downstream

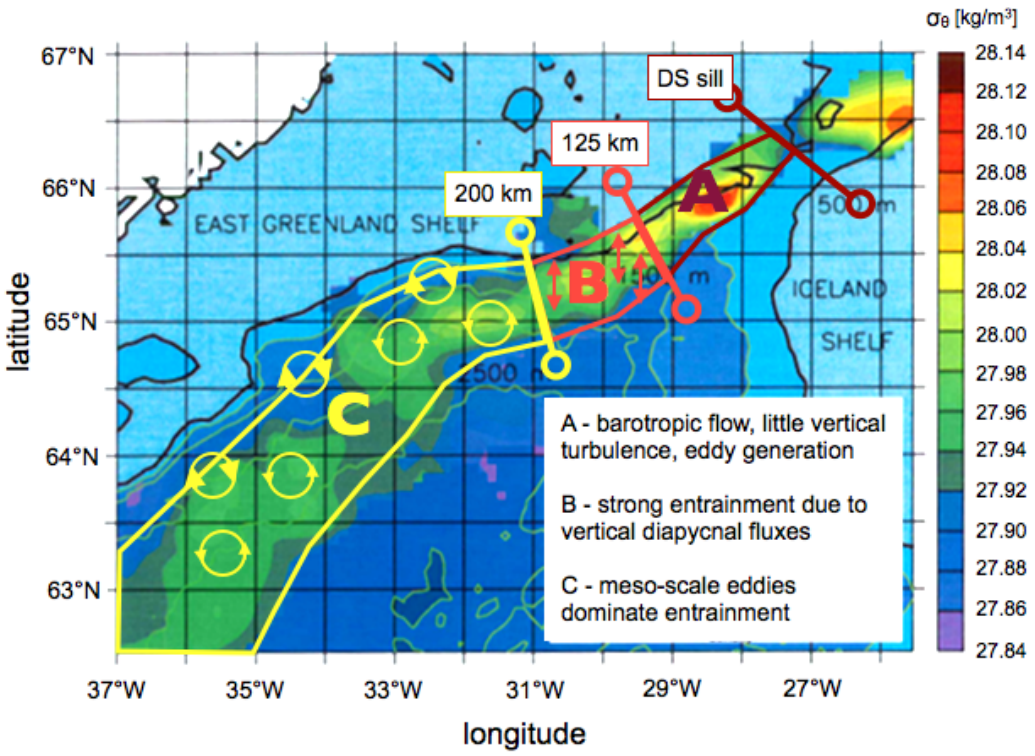

Figure 1.6: Composite bottom density from more than 400 CTD casts of the RV POSEIDON cruises in 1996-1998 implicating the DSO plume. Three different entrainment regimes (A - C) and their relevant mechanisms following *Voet and Quadfasel* (2010) are marked. From *Quadfasel and Käse* (2007) (edited).

(*Girton and Sanford*, 2003). The second regime (B) reaches to about 200 km downstream and is dominated by strong entrainment mainly due to vertical diapycnal fluxes. These are probably caused by large velocity shears resulting from high plume velocities and the transition to a baroclinic flow. Eddy mixing becomes the dominant process for entrainment beyond 200 km downstream (regime C). As the mean plume speed decreases, the velocity shear decreases and the effect of vertical turbulence diminishes further downstream.

A better estimate of entrainment, which accounts for the diapycnal mixing part, is achieved by direct local MS measurements. Here entrainment rates at chosen locations along the DSO plume can directly be estimated from high frequency shear measurements. In June 2012 several vertical MS profiles were collected at about 180 km downstream the sill (Fig. 1.6, regime B) penetrating into the DSO plume. The estimated entrainment was found to be much smaller than the bulk estimates calculated from *Voet and Quadfasel* (2010), (*Paka et al.*, 2013). In addition, bottom turbulence caused by bottom friction rather than turbulence in the layer above the well-mixed plume was found to be important for entrainment (*Paka et al.*, 2013).

The entrainment by vertical mixing may also be enhanced by the passage of meso-scale eddies. FBC observations showed intense diapycnal mixing near the bottom and at the

interface between a quiescent core and ambient water (*Fer et al.*, 2010). The dissipation rate of turbulent kinetic energy (TKE), which can be related to vertical mixing (see below in chapter 3), changed by a factor of 2 - 10 while an eddy passed (*Fer et al.*, 2010). This was supported by observations of shear and stratification profiles (*Darelius et al.*, 2011).

Despite entrainment other pathways of water, for instance contributions from the shelf, could enhance the transport of the DWBC. On the Greenland shelf the East Greenland Spill Jet was found to transport water as dense as DSOW during times when the EGC/Irminger Current front is located seaward of the shelf break (*Brearley et al.*, 2012). In addition an enhanced transport in the Labrador Sea e.g., due to entrainment processes could be relevant for the observed overturning.

In this work the DSO plume and possible entrainment mechanisms are studied in an area about 180 km downstream of the DS sill, where strong entrainment dominated by vertical diapycnal mixing is assumed by *Voet and Quadfasel* (2010) (Fig. 1.6). Embedded into a mooring array and lots of ship-lowered CTD[2] profiles the focus is set on data achieved by horizontal profiling with an autonomous underwater vehicle (AUV). This measurement system has not been used for physical oceanographic studies before. The AUV observations were supposed to catch the interface between dense plume and overlying ambient water to study small-scale turbulence associated with diapycnal mixing. The aim of this study is to answer the following questions: Is the AUV measurement system capable to measure time and space variability in the DSO plume? On which scales did the AUV capture variability in the DSO plume? What were the DSO plume conditions during observed small-scale variability? And finally, what does this locally implicate for the entrainment of ambient water into the DSO plume?

To answer these questions this thesis is structured as follows. In chapter 2 the data and analyzing methods are presented, whereby the focus is set on the processing of the CTD data from the AUV. Chapter 3 gives an introduction into the theory of small-scale turbulent motion in the ocean. Chapter 4 presents exemplarily data gained from AUV missions. The success of the CTD data as well as the potential to capture variability in time and space by different profiling modes is discussed. In chapter 5 the hydrographic AUV data is compared to MS data. The CTD data is analyzed with respect to small-scale turbulence taking advantage of the horizontal profiling instrument. The aim is to define length and time scales of small-scale variability. In chapter 6 the results from chapter 5 are embedded into the plume conditions observed by ship-lowered CTD/LADCP profiles and moored devices with respect to the passage of meso-scale eddies. Finally a conclusion and outlook is given in chapter 7. A list of used acronyms is given in the Appendix.

[2]CTD: conductivity - temperature - depth

Chapter 2

Data and Methods

2.1 Working area

All data were collected as part of a research cruise during June 2012 aboard the *RV Maria S. Merian* (MSM21/1b) between Iceland and Greenland (Fig. 2.1) . The project was a cooperative effort between GEOMAR, Helmholtz Centre for Ocean Research Kiel (Germany) and the Institute of Oceanography at the Centre for Marine and Atmospheric Sciences of Hamburg University (UH). The two main aims of the cruise were to characterize spatio-temporal variability of the Denmark Strait overflow plume and to identify entrainment processes downstream of the Denmark Strait sill. By using a multi-platform approach meso-, sub-meso- and small-scale variability was covered to study possible entrainment processes on a broad range of scales. The main study area (see Fig. 2.1, yellow

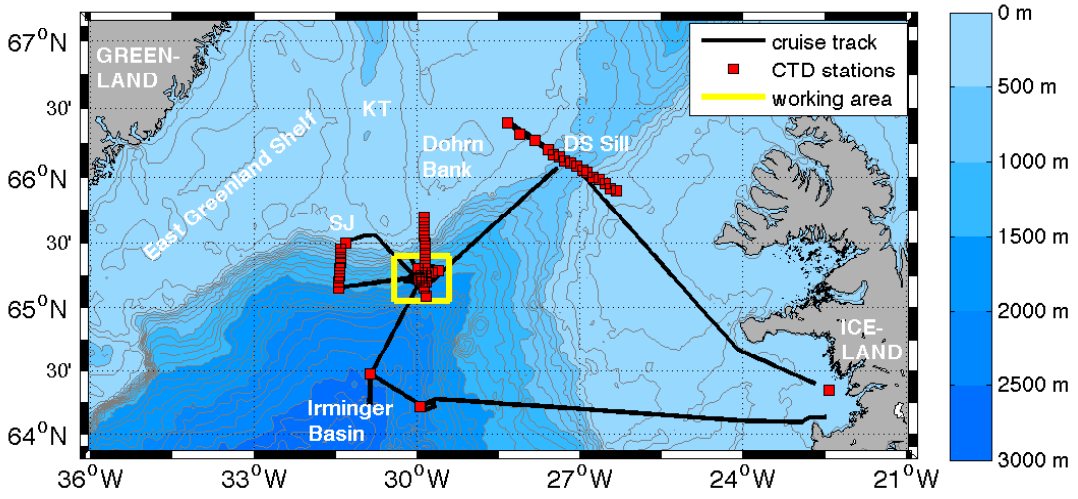

Figure 2.1: Research area of MSM21/1b. Marked are the cruise track (black line), CTD stations (red squares), and the main working area (yellow box). Grey lines indicate lines of constant topography in 100 m intervals. KT = Kangerdlugssuaq Trough, SJ = Spill Jet.

box) was centered around 180 km downstream of the DS sill on the Greenland continental slope south of the Dohrn Bank and upstream of the Kangerdlugssuaq Trough. It extends about 46.5 km east-west and 39 km north-south and covers depth levels from below 1000 m down to about 2000 m depth. The Dohrn Bank array was covered by CTD observations in earlier surveys e.g. analyzed by *Girton and Sanford* (2003) and *Rudels et al.* (2002). Some caution is required as different studies use the name 'Dohrn Bank array' for sections south of the Dohrn Bank 160 km, 180 km, and 200 km downstream the sill.

Almost all data were collected inside the main working area besides three long CTD sections (see Fig. 2.1). The first section was located along the DS sill. Both other sections were located across the Greenland continental slope. One was set about 250 km downstream the sill, named spill jet (SJ) section. The other was carried out about 180 km downstream the sill and extends into the main working area.

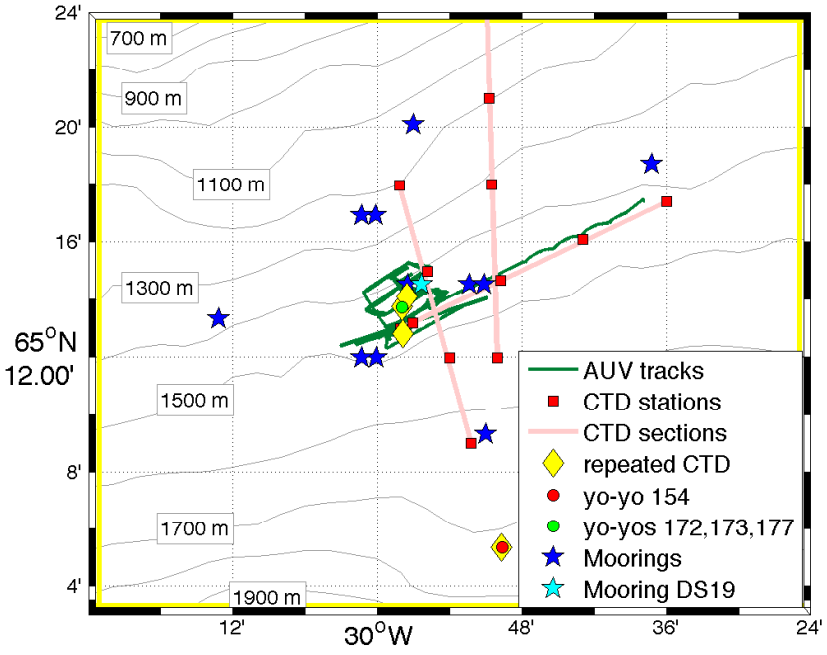

Figure 2.2: Map of the main working area (compare with yellow box in Fig. 2.1) showing all mooring sites (blue stars), repeated CTD stations (yellow diamonds), yo-yo CTD stations (red and green dots), CTD sections (red squares/light red lines), and AUV missions (dark green lines).

Headed by the UH an array of twelve moorings was deployed in the main working area during MSM21/1b. Detailed locations of the moorings, the CTD/LADCP/yo-yo-CTD stations, and the AUV dives in the mean working area are given in Fig. 2.2. In total 53 CTD stations were carried out in the mean working area. At the central location 34 lowered CTD/LADCP profiles and three yo-yo CTD at repeated stations were carried out. Two short CTD sections (of four CTD profiles each) were taken, one along and one across the Greenland slope. In addition eight AUV missions were run.

2.2 The horizontal profiling AUV

This study focuses on data collected by the REMUS 6000 AUV from Hydroid. The AUV was deployed to measure small-scale variability by CTD and MS data along horizontal tracks. In the following, a quick overview of all AUV missions in the main working area and of the general AUV measurement system is given.

2.2.1 AUV missions

In total, eight AUV dives (Abyss 91-98) were completed inside the main working area at the Greenland continental slope (see Figs. 2.1 and 2.3). During all missions the AUV tracks were programmed to follow depth contours. Thus the AUV was diving parallel to the mean flow direction. To achieve a smooth running AUV and capture small-scale variability the vehicle was programmed to follow tracks at constant depth or altitude levels. Specific information about the release and recovery times as well as the locations

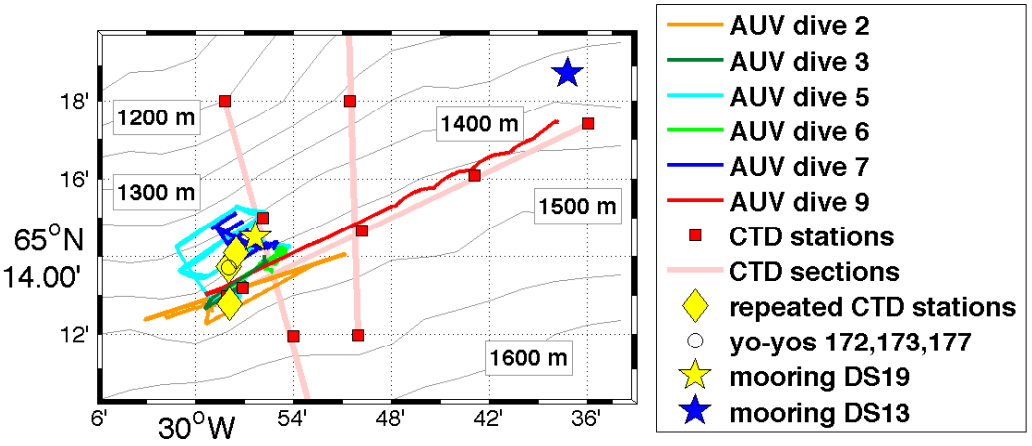

Figure 2.3: Map of all AUV missions as well as CTD stations and mooring sites close to the AUV missions. (See legend for further details.)

is given in Table 2.1 and in the map in Fig. 2.3. Only five of the eight dives were carried out successfully. Dive 4 was aborted quickly after its release due to a leak message. During dives 3 and 8 the AUV was not able to catch its next waypoint as strong counter currents reduced its speed to less than 1 knot which caused a timeout of the AUV system. To avoid this problem the AUV was ascending about 200 m above the seafloor for counter current tracks. In the five successful missions the AUV followed different programmed patterns (see Fig. 2.3). The missions lasted between 13 to 14.5 hours except for AUV dive 9 which lasted almost 7 hours.

Dive ID	AUV ID	launch date	launch (UTC)	recovery (UTC)	mean depth(dive 2)/height above seafloor (all others) [m]
2	91	12.-13.06.2012	22:01	11:11	1415/1365/1315/1265/1215/1165
3	92	14.06.2012	11:41	22:20	100 (timeout at $\sim$ 15:00)
4	93	16.06.2012	08:07	08:29	leak message
5	94	16.06.2012	13:20	02:44	100/200
6	95	17.06.2012	18:34	08:25	43/67/91/115/140/190
7	96	18.-19.06.2012	22:46	13:16	90/180
8	97	20.06.2012	06:06	07:49	timeout
9	98	20.06.2012	09:14	16:06	91

Table 2.1: List of all AUV missions in the main working area in June 2012 giving the date, the start and end times of each mission, and the mean depth or height above the seafloor along horizontal profiling tracks.

2.2.2 AUV measurement system

The AUV is 3.99 m long, has a diameter of 66 cm and weighs 240 kg, including its standard sensors (photos in Fig. 2.4). The AUV can dive with speeds up to 2.3 $\frac{m}{s}$. With two coupled yaw and pitch fins (photo B in Fig. 2.4) the vehicle can control its direction following a certain altitude, depth, yo-yo or track-line. Here all missions were programmed to dive with a constant speed of 1.5 $\frac{m}{s}$ through the water and follow horizontal tracks at either a certain depth or altitude level to resolve small-scale motion. By diving at constant speed with the flow the AUV measures the properties of the surrounding water. When the AUV changed its heading direction or accelerated to dive, e.g. upwards, the data might have been influenced. Thus only data from the horizontal tracks are considered in this study.

Sensors attached to the AUV

Several standard sensors were attached to the AUV (Table 2.2). CTD data was measured by a SBE[1] 49 FastCAT CTD installed on the right upper side of the vehicle (Fig. 2.4, photo B). Additionally a Paroscientific pressure sensor and navigation instruments were attached to the vehicle. The CTD can achieve high spatial resolution with a sampling frequency of 16 Hz. For all AUV missions during MSM21/1b the CTD system was sampling with a frequency of 4 Hz. This change in the settings was chosen by mistake. The CTD system used since 2007 was last calibrated in 2009. CTD data cannot be corrected using these calibration coefficients due to the non-linear behavior of drifts. This can cause small deviations of the absolute temperature and salinity values.

In addition to the standard sensors, a MicroRider 6000 horizontal microstructure pro-

[1]Sea-Bird Electronics

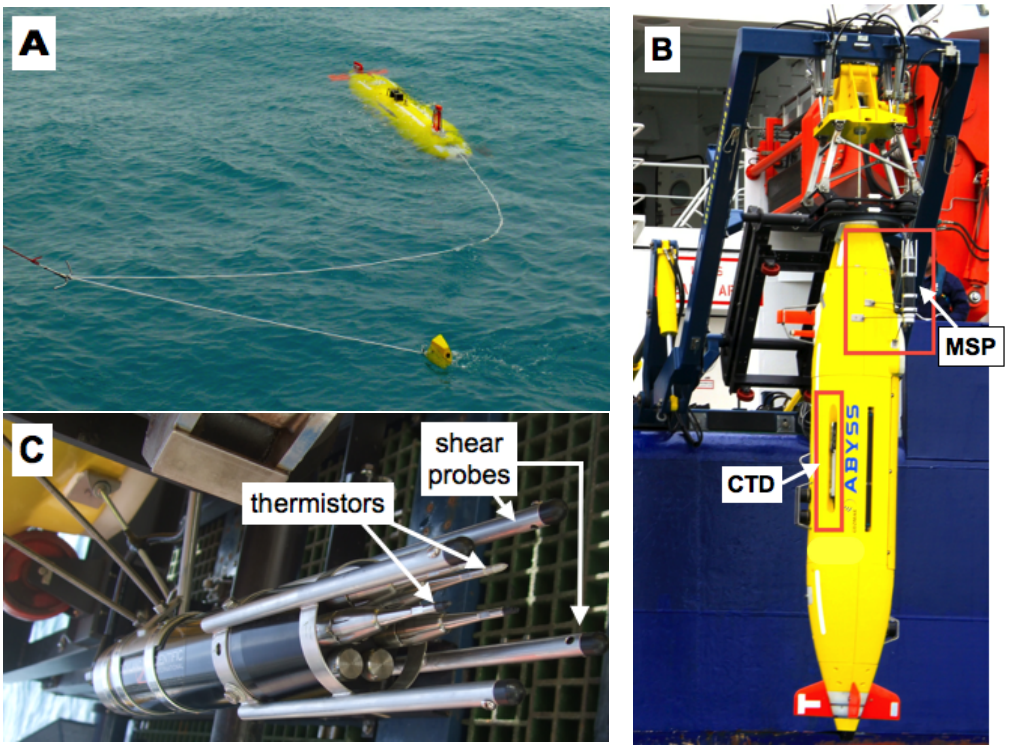

Figure 2.4: The AUV system used during MSM21/1b. Photo A (top left) shows the AUV diving on the water surface and its recovery through the float which popped off from the vehicles nose. Photo B (right) shows the recovery of the AUV on board of the research vessel. Marked are the CTD and the MSP attached to the AUV (red boxes). Photo C (bottom left) shows the MS sensors. Highlighted are the shear probes and the fast thermistors. All photos have been taken during MSM21/1b by the AUV ABYSS team from GEOMAR (A, B) and Sandra Tippenhauer (C) (edited).

filer (MSP) from Rockland Scientific was attached near the bow of the AUV (Fig. 2.4, photos B and C). It was mounted at a sufficient distance from the hull to avoid artificial turbulence caused by the motion of the AUV. Among others the MS measurement system was equipped with two microstructure turbulence shear probes which provide the estimation of dissipation rates (see Fig. (2.4), photo C, and Table (2.2)). Two high-accuracy accelerometers were used to remove platform vibration contamination from the shear measurements.

The photos from the AUV recovery during MSM21/1b give an idea of the application of the AUV (Fig. 2.4, photos A and B). Triggered through an acoustic signal the nose float of the vehicle pops off. It can drift on a 20 m long recovery line away from the AUV. Photo A shows how the line is snagged by a grapnel hook. On deck the line is connected to the launch and recovery system (LARS) winch and the vehicle is pulled up (Fig. 2.4, photo B).

instrument	sensor	sampling frequency [Hz]
pumped SBE 49 FastCAT CTD	1 temperature probe 1 conductivity cell 1 pressure sensor	4
Paroscientific 8B7000	1 pressure sensor	1
MicroRider 6000 (Rockland Scientific)	2 velocity shear probes (SPM-38-1) 2 fast response thermistors (FP07-38-1) 1 high-resolution pressure sensor 2 high-resolution accelerometers 1 tilt sensor	512

Table 2.2: List of all oceanographic measurement instruments installed on the AUV. Given are the sensors and the used sampling frequencies during MSM21/1b. (Navigation instruments are not listed.)

Navigation of the AUV

The AUV used a combination of three different navigation systems. The GPS is used to receive the initial position of the vehicle prior to each dive and to align the Inertial Navigation System (INS) on the water surface. Under water the vehicle cannot receive any GPS[2] signals and thus the INS continuously integrates the acceleration along the three axes to calculate the position of the vehicle. About 200 m above the bottom the AUV gets additional position information from the Doppler Velocity Log (DVL) based on data of a downward-looking ADCP[3]. If the DVL is in the range of the bottom it provides altitude data for the bottom-lock and measures speed over ground. To maintain its alignment the AUV used the input from the GPS in combination with the DVL. In addition the DVL receives CTD data to calculate sound speed for the Long Baseline Acoustic Navigation (LBL). The LBL system was used to achieve a more accurate positioning. It provides that the vehicle can compute and correct its position relying on triangulation between three moored acoustic transponders. The transponders were positioned in a row with a distance of about 4 km oriented across the Greenland slope to ensure that the AUV would be able to follow isobaths inside the LBL net with high accuracy.

2.2.3 AUV-CTD data processing

In order to resolve small-scale hydrographic properties by horizontal profiling with an AUV in the transition layer above the DSO plume there was a need for high-quality data. Thus a processing routine to test and correct the raw CTD data was developed using MATLAB. In the following, the corrections applied to the data are explained.

[2]GPS - global positioning system
[3]ADCP - Acoustic Doppler Current Profiler

Correction of the navigation data

As described above, the AUV used three different positioning systems. The navigation data from the descent and rise of the AUV relied on the integration from GPS data. The impact of current water speed can cause large deviations in those positions. At depth the LBL navigation was most accurate but covered only a certain range of a few kilometers. In cases where the AUV was out of the range of the LBL system, it relied on the DVL bottom-lock. When the AUV was in the range of the LBL again, it switched back to the high accurate LBL navigation. This caused artificial jumps in the position data. During the AUV missions of MSM21/1b these jumps ranged from tens of meters up to 430 m. A routine based on calculated distances from the navigation data accounted for this problem. All position data, which showed gaps larger than 15 m in the distance between two consecutive points, were corrected by linear interpolation. The longer the gap, the more steps back in time were chosen to interpolate the positions (latitude/longitude) in an appropriate way. An example is given in Fig. 2.5. During the descent of the AUV

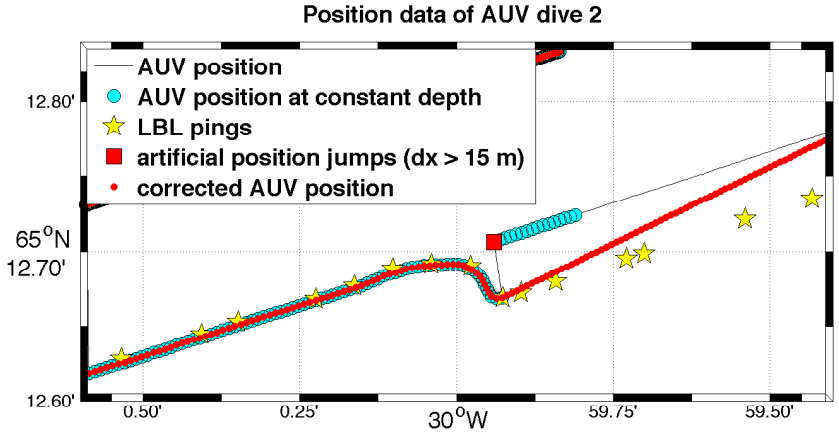

Figure 2.5: Position data of a chosen part in AUV dive 2. Shown is the original position data achieved from the combination of the three different navigation systems (black line). At times when the AUV was diving at constant depth the positions are marked by dots (cyan). The signals from the LBL data along the programmed track are indicated by yellow stars. The red square marks the point just before an artificial jump in the position data is detected. The line of red dots indicate the interpolated position data.

(black line) the vehicle does not get position data from the LBL or DVL. Thus it cannot follow the positions given from the LBL pings (yellow stars). At constant depth (cyan dots) the AUV first followed its track using the GPS and DVL positioning system. Then it received a signal from the LBL system and thus a jump in the position data occurs (red square). The corrected data (red dots) shows a smooth transition of the position data.

Performance of the pressure sensors

In total three pressure sensors were installed on the AUV (Table 2.2): one Paroscientific pressure sensor, the second as part of the CTD system and the third as part of the MSP. Due to historical reasons, the raw data output from the AUV provided depth converted from the original pressure data. It is important to note that the depth was internally calculated in different ways for the CTD and the Paroscientific pressure sensor. When the vehicle receives data from the Paroscientific sensor, it converted the pressure to depth by using the UNESCO routine (*Fofonoff and Millard.*, 1983). In contrast the pressure data [dbar] from the SBE 49 FastCAT was multiplied by a constant of 0.995828 to compute depth [m]. Pressure data from the MSP had not automatically been converted to depth.

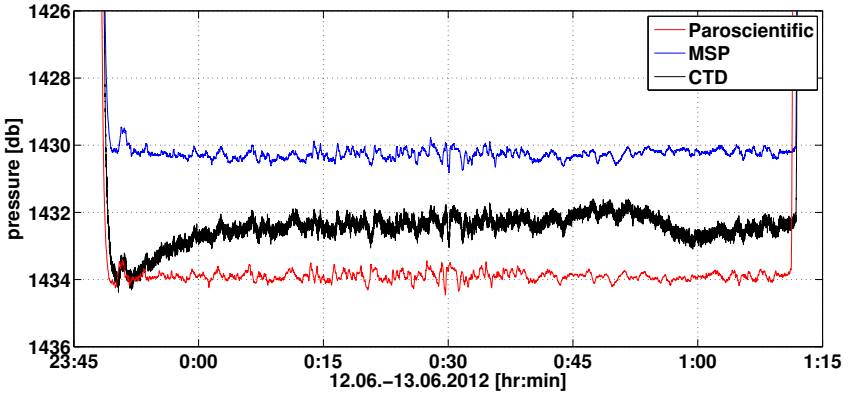

Figure 2.6: Pressure data collected by the three pressure sensors attached to the AUV at one depth level. Shown are data of a transect from AUV dive 2 from the raw Paroscientific pressure sensor (red line), the raw pressure from the CTD system (black line), and the interpolated pressure from the MSP (blue line).

The quality of the Paroscientific pressure sensor, which is supposed to be the most accurate system, was tested by comparison with pressure data collected by the other two systems. Offsets between the three pressure records were observed during periods when the AUV was programmed to keep tracks at constant depth level. The transect shown in Fig. 2.6 gives an example of the differences in pressure data. At about 23:50 the AUV dives down to the programmed depth level. It follows the constant depth for about 1 hr 20 min before it rises. Upon arrival at the largest depth the MSP and the Paroscientific pressure sensors adjust quickly to the constant depth level. The CTD-pressure overshoots and adjusts slowly to a constant depth level. At this depth level, the pressure of the CTD system is most of the time about (1 - 2) dbar smaller than the pressure sampled by the Paroscientific sensor. The MSP-pressure differs by about 4 dbar from the Paroscientific one, which showed smaller pressure values as well. The observed offsets are related to depth. At the surface the CTD-pressure shows a larger offset between -5 dbar and

-6 dbar while the MSP-pressure differs less than -1 dbar from the Paroscientific pressure values. As almost all constant tracks were carried out at about the same depth close to the bottom, no direct relation between the pressure values can be calculated with respect to depth. Nevertheless as the AUV system was turned on in the water, the sensors were expected to show a pressure of 0 dbar at the sea surface. Even though the Paroscientific pressure sensor had the lowest sampling frequency of 1 Hz (see Table 2.2), it appeared to be the most reliable of the three sensors providing readings with no offset at the sea surface.

Adjustment of temperature and conductivity data

In order to achieve highly accurate hydrographic properties of the same water sample one needed to account for the response time of the CTD sensors and their location in the pumped CTD system (Fig. 2.7). This was especially important as salinity is calculated from temperature, pressure, and conductivity data. The temporal and spatial mismatches of the raw temperature and conductivity raw data required corrections in order to capture the same water mass at all sensors at the same time.

The temperature was measured by a fast-response thermistor. The response time of the thermistor is short (< 1 s). Related to its cell thermal mass and boundary layer physics the conductivity cell has a longer time-scale response (order of 10 s) (e.g. *Johnson et al.* (2007)). To remove the time delay the thermistor is used as a recursive conductivity filter. It aims to match temperature and conductivity responses inside the conductivity cell. For the corrections the same formulas and constants as given in the Seabird Software (*Sea-Bird Electronics*, 2012) for the SBE 49 CTD based on the experiments of *Lueck* (1990) were used.

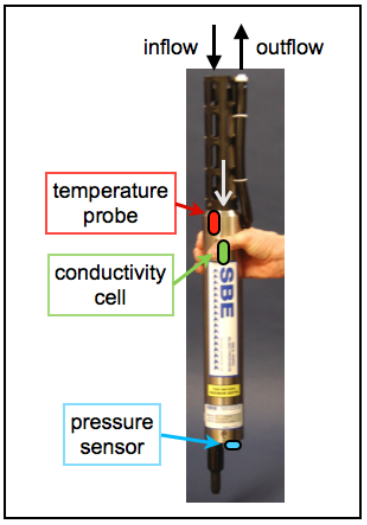

Figure 2.7: Photo of the SBE 49 FastCAT CTD with the approximate location of the pressure sensor (blue), the temperature probe (red), and the conductivity cell (green). The intake of the CTD is marked by the white arrow. Photo from *Sea-Bird Electronics* (2013) (edited).

The temperature probe is located near the intake and the conductivity cell downstream of the intake of the CTD (Fig. 2.7). The water pumped through the CTD first passes the temperature sensor and subsequently flushes the conductivity cell resulting in a delay between both sensors. Given a uniform flow rate the time lag can be estimated owing to the physical separa-

tion of the two instruments. The time offset was computed relying on a Matlab routine commonly used as a standard for lowered CTD systems (Gerd Krahmann (GEOMAR), personal communication). Based on lag correlation techniques the aim was to find the delay associated with the largest correlation. Since the time delays are expected to be smaller than 1 s, temperature and conductivity data were interpolated onto a time-grid with 10 times the original sampling resolution before the lagged cross-correlation was applied. Nevertheless no significant delays were found in the CTD system. Even when the resolution was increased by 50 times the conductivity delay was negligibly (< 0.002 s). This may have been caused by the use of a much lower sampling frequency of 4 Hz compared to 24 Hz used for the standard ship-lowered CTD applications.

The choice of a cutoff frequency

In order to reduce high frequency noise in the CTD data a butterworth low-pass filter was applied. As small-scale variability was of interest, it was important to use a cutoff frequency which efficiently removes noise but still retains sufficient energy in the high frequency limit. Spectral analysis (theory in chapter 2.5) was used in order to distinguish signals from random noise.

Both time series were normed by their standard deviation (std) in order to compare the energy of the temperature and salinity data with each other. It is assumed that the temperature and salinity signals should be coherent and thus should be similarly

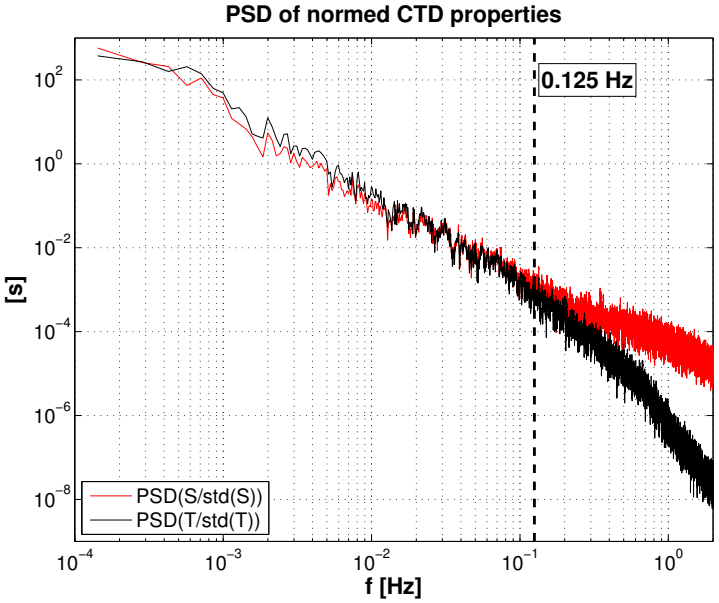

Figure 2.8: Power spectral density (PSD) of normed temperature (black) and salinity (red) time series from AUV dive 2. The noise level, which is set to the cutoff frequency, is chosen to be at 0.125 Hz (black dashed line).

represented in the spectrum. The example of AUV dive 2 shows that at frequencies below 0.125 Hz the normed spectra show comparable values (Fig. 2.8). For higher frequencies the energy of the normed temperature falls off more rapidly. The higher energy in salinity on large frequencies is an indicator for more noise in the data. A cutoff frequency of 0.125 Hz was chosen to account for this noise. Severals test were carried out to validate the lowpass filtered data: Filtered time series were compared to the original ones, the sensibility of the $\Theta - S$-plots was tested, and the variance between the original and the filtered data was calculated (not shown). The chosen filter performed well. It fulfilled the given criteria to reduce noise but still resolve variability on low frequencies.

Despike altitude and salinity

In the time series of salinity and altitude freak values were observed and removed from the data. The spikes were detected based on two criteria. The first was given by the choice of a reasonable range applied to the data. The second criterium accounted for chunks between adjacent values. Here, the standard deviation of the difference in adjacent values was calculated. If the values exceeded a chosen tolerance range, they were not considered for further analyses.

Estimate current velocity

It is desirable to calculate current velocities from the AUV to study small-scale turbulence with respect to DSO plume velocities. Based on the motion of the AUV through the water it is possible to estimate the current velocity in the direction of the AUV. In principle the velocity of the AUV above the ground can be calculated from the positions of the AUV provided by the navigation data. The velocity of the AUV through the water into the direction of the AUV can be estimated from its thruster. Several tests were carried out by Sandra Tippenhauer (GEOMAR) in order to achieve reliable velocity data based on the thruster data. The mean AUV velocity through the water was found to be 1.6 $\frac{m}{s}$ which slightly deviates from the given programmed value of 1.5 $\frac{m}{s}$ (see above). From the difference of the velocities through the water and the velocities from the AUV positions it is possible to estimate the current velocity at the AUV depth and in the direction of the AUV track. Thus from dives at a constant depth along the continental slope (aligned with the DSO plume) the absolute plume velocity at that depth can be estimated. During phases of the descent or rise of the AUV such estimates tended to get noisy and were not considered in this study.

Dissipation rates from the MSP

The dissipation rate describes the energy conversion from kinetic energy of turbulent motion to heat and thus can be understood as a measure of small-scale turbulent mixing. This data provided by the AUV-MSP give additional information to the hydrographic CTD data to describe small-scale variability in the DSO plume. Dissipation rates are estimated from the velocity fluctuations measured by the shear probes (see Fig. 2.7, photo C). The theory is based on the occurrence of universal spectra in the turbulent ocean (see below in chapter 3). In general the observed microstructure shear velocity record from the shear probes is divided into six-second-long segments to calculate wave number spectra. These shear spectra were integrated and compared to the empirical Nasmyth universal spectrum (*Thorpe* (2005, p. 175) and references therein) to estimate rates of the dissipation of kinetic energy. These dissipation rates are directly related to the vertical turbulent exchange coefficients and may serve as a measure for the diapycnal contribution of entrainment (the theory is given below chapter 3).

Processed dissipation rates derived from the two pairs of shear probes were provided by Sandra Tippenhauer (GEOMAR). The comparison of the dissipation rates derived from both shear probes showed similar values during most AUV missions. They correlated with r ≥ 0.9 (with the exception of dive 6) and show a negligible offset in the range of the background noise (with the exception of dive 5, offset of O(10^{-3})$\frac{W}{kg}$). For dives 5 and 6 the data only from one shear probe is used for further analyses, chosen by visual inspection.

Final processing file and data resolution

After all above given corrections were applied, all data was interpolated onto a common time grid with a constant time step. This time step was chosen to be 4 s which is half of the cutoff period to resolve periodic signals. The corresponding spatial resolution is about 6.4 m as the AUV pursued the measurement with a speed of about 1.6 $\frac{m}{s}$ through the water. Potential temperature (Θ [°C]), salinity (S), pressure (p [dbar]), potential density (ρ_θ [$\frac{kg}{m^3}$]), and distances from navigation data were calculated using the Sea water library provided by GEOMAR. In the following the density anomaly (σ_Θ) is considered, which is the difference between the actual density ρ_Θ and a reference value $\rho_{ref} = 1000\frac{kg}{m^3}$ ($\sigma_\Theta = \rho_\Theta - \rho_{ref}$).

A Matlab-based routine for the processing of the hydrographic, navigation, and microstructure measurements of the AUV was developed in cooperation with Sandra Tippenhauer (GEOMAR), which can easily be adjusted to future AUV missions.

2.3 Vessel-based observations

2.3.1 Ship-lowered CTD/LADCP profiles

Profiles of CTD and LADCP[4] data were used to study hydrographic characteristics and current velocities of the overflow plume and the ambient water in the vertical. In addition the ship-lowered CTD data was used to validate the hydrographic AUV-based CTD measurements.

In total 92 lowered CTD casts were carried out during MSM21/1b. A standard CTD SBE 911+ system equipped with two pairs of temperature, conductivity, and oxygen sensors with a sampling frequency of 24 Hz was used. The conductivity and oxygen sensors were calibrated with water samples taken by Niskin bottles. The processed data provides CTD profiles with a vertical resolution of 1 dbar extending from the surface down to approximately 10 m above the seafloor.

During all casts two LADCPs were mounted on the CTD rosette system, one upward- and one downward-looking, for ocean current measurements. The data was processed in a Matlab routine based on version 10.16 of GEOMARs LADCP processing (following *Fischer and Visbeck* (1993)). Due to communication errors no data was recorded during four CTD casts (at stations 141, 142, 148 and 153). The processing failed for station 171 due to missing raw data. The successfully processed data provides zonal and meridional velocity components with a vertical resolution of 10 dbar. For the DSO plume analysis it is desirable to rotate the coordinate system to achieve along-stream and cross-stream velocity components. The along-stream component is defined as the velocity into (downstream) the plume direction along constant lines of topography. The cross-stream component is perpendicular to the mean plume direction. In the central part of the mean working area the zonal and meridional velocity were rotated by -75° to achieve cross-stream and along-stream components, respectively. The mean angle was calculated based on the topography.

As mentioned before three main CTD sections were carried out during MSM21/1b (see map in Fig. (2.1)). In the mean working area two short CTD sections (four profiles each), several CTD casts at repeated positions, and four yo-yo- casts provide a high temporal resolution of vertical CTD data (see Fig. 2.2). Three spots of repeated CTD stations were close to each other in the central working area (here referred to as the same spot) reaching down to about a depth of 1430 m depth inside the DSO plume. This data is used to define plume conditions during the AUV dives. A fourth spot of repeated CTD profiles was further downslope in the deepest part of the working area reaching down to about 1760 m deed on the offshore edge of the DSO plume.

[4]LADCP: lowered acoustic doppler current profiler

To observe changing characteristics of the overflow plume four CTD yo-yos were carried out. The yo-yo data were linearly interpolated onto a regular space-time grid to illustrate the changes in time by an interpolated contour field (dp = 1 dbar, dt = 1 min). A gaussian mean over 15 depth levels was applied to filter the hydrographic data. The salinity data were not only vertically but also horizontally filtered with a gaussian mean over 15 minutes. This treatment was chosen not only to resolve the transition zone between the ambient water and the DSO plume but also to account for small errors in the vertical caused by the alternately upward and downward profiling.

During 25 CTD casts the CTD rosette was additionally equipped with a free-falling Baklan microstructure probe. The MSP was released in the upper boundary of the interfacial layer above the plume to estimate entrainment velocities into the plume (see *Paka et al.* (2013)).

2.3.2 DSO plume layers

With regard to measure small-scale variability with the AUV in the transition zone of the plume and the ambient water, there is the need to define plume layers. Based on the CTD/LADCP profiles at repeated stations close to the AUV missions the approximate plume height can be defined and thus be linked to the AUV missions.

In general the DSO plume is characterized by a well mixed bottom plume layer (BL). It is colder, saltier, and oxygen enriched compared to the ambient water ($\Delta\Theta$ = (1.5 - 4)°C, ΔS = (0.05 - 0.15), Δoxygen = (15 - 45) $\frac{\mu mol}{kg}$). The absolute velocities range from approximately 0.4 $\frac{m}{s}$ to 1.1 $\frac{m}{s}$ in the mixed DSO plume. Consequently a layer with strong density and velocity gradients separates the plume from the ambient water. This layer is referred to as stratified interfacial layer (IL). The overall plume depth varied during MSM21/1b approximately between 40 m and 200 m. For analyzing entrainment processes caused by vertical mixing it is desirable to evaluate the plume and interfacial layer thicknesses in the working area and their evolution with time. Here the robustness of criteria for defining the layer boundaries of the DSO plume are tested.

Fer et al. (2010) defined criteria for plume analysis regarding the FBC overflow plume. In their study the upper boundary of the mixed plume bottom is calculated as the height above bottom where the difference in potential density from the bottom-most value exceeds 0.01 $\frac{kg}{m^3}$. The depth above the upper interface of the bottom layer where the vertical gradient of potential density first drops below $5 \cdot 10^{-4} \frac{kg}{m^4}$ is defined as the upper interface of the interfacial layer (IL_1). The same criteria were applied to the CTD data in the mean working area. Two examples of potential density and velocity profiles at stations 132 and 182 are given in Figure (2.9). In all profiles the bottom layer (shaded green) matches the well mixed plume layer indicated by high densities and strong velocities. The

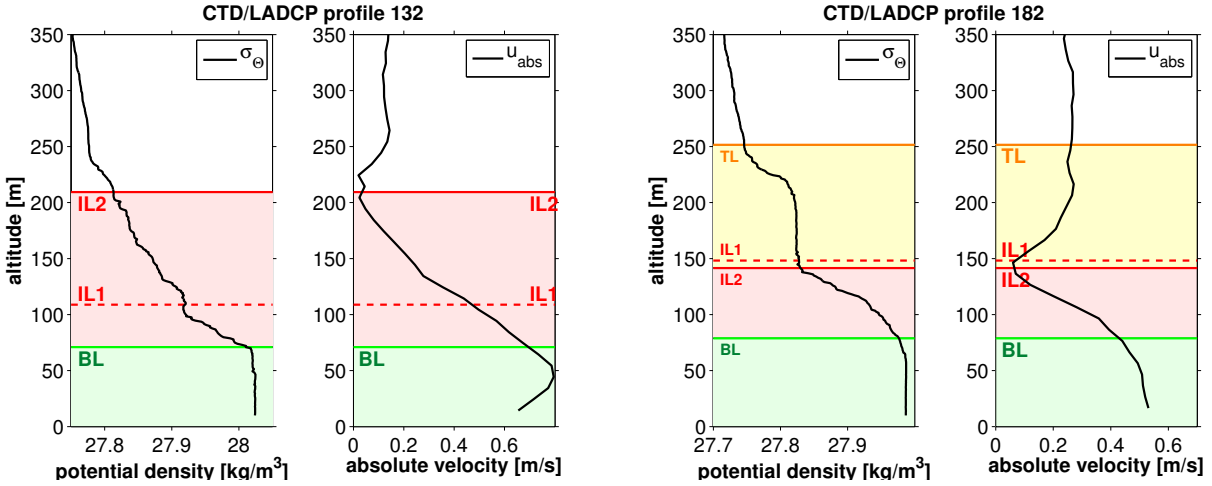

Figure 2.9: Vertical profiles of potential density and absolute velocity at CTD stations 132 (left) and 182 (right). The profiles range from the seafloor to 350 m above it. Marked are the bottom layer (green shading) and its upper interface according to 0.01 $\frac{kg}{m^3}$ (green line), the interfacial layer (red shading) and its upper interface based on the density gradient criterium (IL_1, red dashed line) and based on the velocity criterium (IL_2 , red line), and the transition layer (yellow shading) with its upper interface (TL, orange line), respectively.

interfacial layer (shaded red between green line and red dashed line) covers the zone of strong density and velocity gradients above the BL. However using the density criterium to calculate the upper interface of the interfacial layer (IL_1, red dashed line) does not always work reliably as visual inspection reveals. For instance in profile 132 the upper boundary of the interfacial layer is found at about 105 m above the seafloor (Fig. 2.9, left). This is caused by an approximately 20 m thick homogeneous layer. Above, a strong gradient in density and velocity indicates that the interfacial layer extends even further. Thus another criterium based on LADCP current velocity[5] data is tested to achieve more reliable results. The upper interface of the interfacial layer is defined as the depth above the bottom layer (BL +10 m) where the vertical gradient of absolute current velocity first drops below 0.1 $\frac{cm/s}{m}$. The threshold of 0.1 $\frac{cm/s}{m}$ has been chosen by visual inspection. In profile 132 the upper interface of the interfacial layer based on the velocity criterium (IL_2, red line) is found 100 m higher above than the one calculated by the density criterium (IL_1, red dashed line) (Fig. 2.9). In contrast, in profile 182 the interfacial layer calculated by the two different criteria results in rather similar thicknesses (Fig. 2.9, right). Although, a second thick homogeneous layer can clearly be distinguished both from the plume and from the ambient water. Thus a third layer is defined referred to as transition layer (TL). The upper interface of the transition layer is defined as the depth where the vertical potential density gradients first exceed a value of $(5 \cdot 10^{-4})$ $\frac{kg}{m^4}$ in the range of 50 to 200 m above the upper boundary of the interfacial layer (marked in Fig.

[5]A running mean over 20 m was applied to the LADCP profiles.

2.9 by the orange lines). Thus only homogeneous layers with a thickness larger than 50 m are taken into account. In profile 182 the transition layer is about 100 m thick (Fig. 2.9, right).

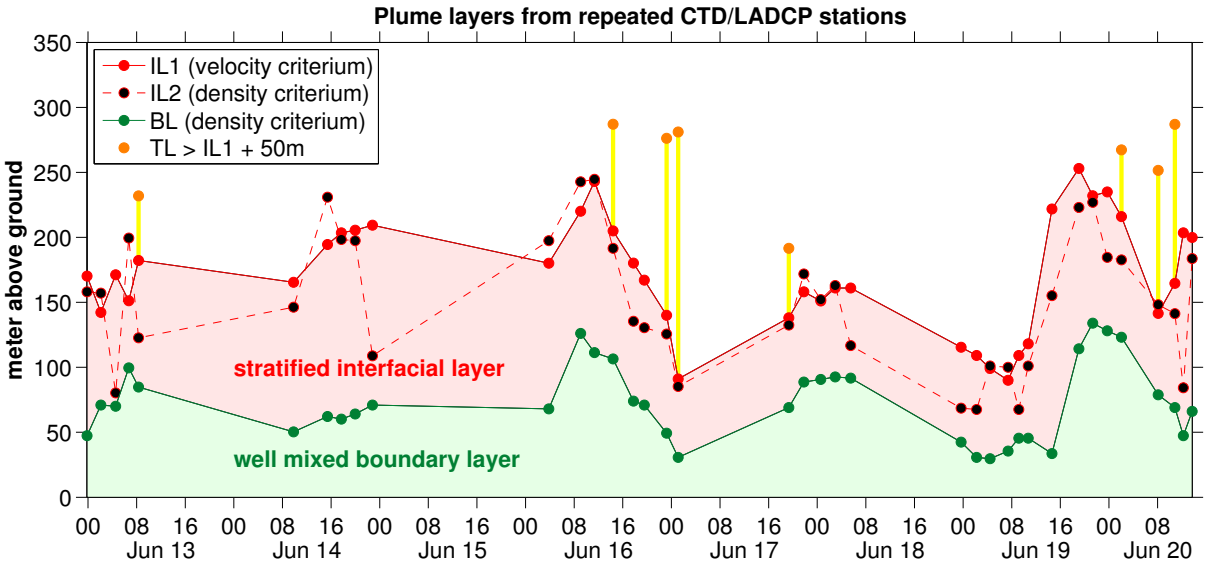

Figure 2.10: Evolution of the boundary layer (green), the interfacial layer(red) and the transition layer (orange dots) computed from all repeated CTD stations (dots). (See caption of Fig. 2.9 for explanation.)

Figure 2.10 shows the interfaces calculated from all CTD profiles carried out at the two repeated CTD stations in the mean working area. The interfaces are marked in the same way as in Fig. 2.9. The comparison of the interfacial layer based on the two given criteria (IL_1 and IL_2) often shows similar thickness but the IL_2-based interface is positively correlated with the upper interface of the bottom layer in time and thus gives physically more reasonable results. For further analyses of the plume layers the interfacial layer is based on the IL_2-criterium.

2.4 Moored observations

Moored instruments were used to study the meso-scale variability in the mean working area. This additional information is of interest as the passage of eddies changes the hydrographic plume characteristics and can cause lateral entrainment.

Moorings anchored on the seafloor are used to obtain time series from oceanographic sensors in the water column. Such stationary observatory systems sample water characteristics based on the Eulerian approach: changes in time of fluid characteristics are observed at a fixed point in space. In total twelve moorings were deployed during June 2012 inside the working area (see Fig. 2.2). It is beyond the scope of this work to use the

whole dataset from the mooring array. To analyze meso-scale variability mooring DS19 located in the mean working area and mooring DS13 further upstream were taken into account (see Fig. 2.2).

2.4.1 Moored instruments

The mooring DS19 provides current speed, temperature, and salinity data in and above the DSO plume in the mean working area from June 17 to August 7, 2012 (see map in Fig. 2.3). The mooring was equipped with one 1200 kHz RDI[6] acoustic Doppler current profiler (ADCP) and four point current meter (Nortek Aquadopp), six MicroCATs (MC) collecting temperature, conductivity, and pressure data, and four temperature recorders (T-recorders) (details are given in Table 2.3). All these devices were moored between 54 and 194 m above the seafloor[7]. The mooring DS13 was located 16.7 km upstream (approximately 50 m further upslope) compared to the central mooring DS19 (see Fig. 2.3). The velocity data is used in comparison with the data at the central mooring to estimate the travel time, for instance of propagating eddies in the DSO plume. The

Instrument	company	sampling rate [s]	lowpass-filter cutoff [min]	height above ground [m]	depth [m]
ADCP 1200 kHz	Teledyne RD Instruments	5	5	112	1297
Aquadopp 1	Nortek AS	12	5	107	1302
Aquadopp 2				100	1309
Aquadopp 3				93	1316
Aquadopp 4				85	1324
SBE 37SM MicroCAT	Sea-Bird Electronics	20	T: – S: 10 p: –	144	1265
				113	1296
				105	1304
				98	1311
				91	1318
				54	1355
T-recorder (TR1050/ TR1060)	RBR	10	–	194	1215
				134	1275
				124	1285
				86	1323
RCM 11	Aanderaa	10	–	24	1339
SBE 37SM MicroCAT	Sea-Bird Electronics	20	– –	23	1340

Table 2.3: Technical details of the instruments used in the central mooring DS19 (top) and in mooring DS13 (bottom).

[6]Teledyne RD Instruments

[7]The mooring design is given in the Appendix.

mooring design included one recording Doppler current meter (Aanderaa RCM 11) and a SBE 37 CTD (Table 2.3). They were placed right on top of each other about 20 m above the seafloor.

In principle current velocities and directions are obtained with the ADCP and Aquadopps using the Doppler shift of acoustic beams. All raw velocity data were lowpass filtered with a cutoff rate of five minutes to account for noise. The hydrographic time series collected by the MCs and T-recorders are used to construct an interpolated potential temperature and salinity field[8] with a time resolution of 20 s. This was desirable to account for the suppression of the moored devices due to strong current speeds. The salinity data was low-pass filtered with a cutoff of 10 min to reduce noise.

2.4.2 The performance of moored current measurements

Problems for the moored current measurements were encountered during events of high current velocities exceeding $\sim 0.8\ \frac{m}{s}$. Such large current speeds lead to blowdowns of the

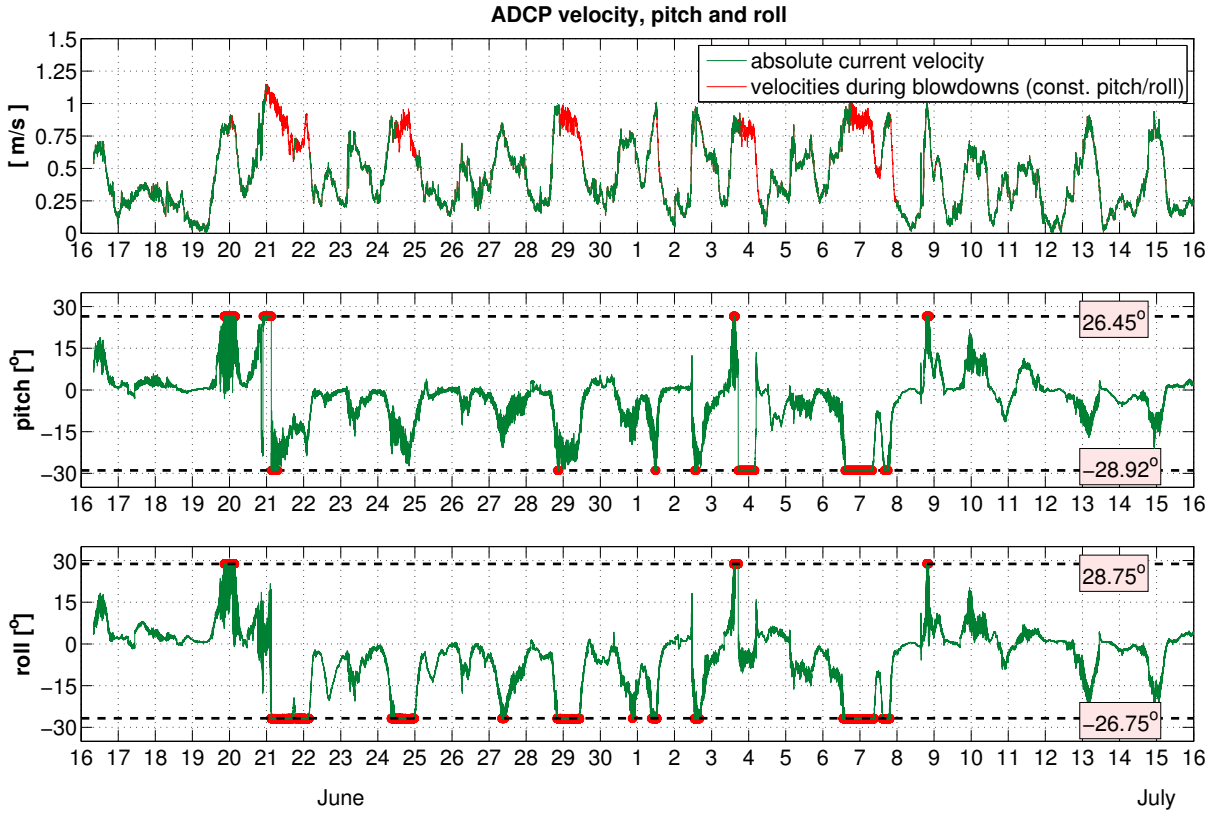

Figure 2.11: ADCP timeseries (top), pitch (middle), and roll (bottom) during the first month of the deployment of mooring DS19. Black dashed lines mark the thresholds (numbers are given in the red shaded boxes) for pitch/roll beyond which the velocity data is discarded (red parts of the graph).

[8]The interpolated data sets were provided by Kerstin Jochumsen (UH).

moorings. During these events all moored devices were tilted. With increasing sensor tilt the estimate of horizontal velocity as a function of depth becomes increasingly unreliable. Fig. 2.11 shows the ADCP (DS19) velocity time series together with the pitch, (i.e., the angle of rotation about the x-axes) and roll (i.e., the angle of rotation about the y-axes), of the instrument. During strong blowdowns the angles of either pitch or roll reach a plateau near 26° to 29°. Such values are physically not plausible and cause errors in the calculation of current speeds. By defining thresholds for pitch and roll such events were excluded from the velocity time series (marked in red). The same procedure was applied to correct data of the Aquadopps.

The ADCP data was compared with the velocity data collected by the four Aquadopps to check the consistency of the datasets. All devices were placed in the mooring DS19 close to each other in a range between 85 m and 112 m above the seafloor (see Table 2.3). Fig. 2.12 illustrates the absolute velocity and current direction from the ADCP

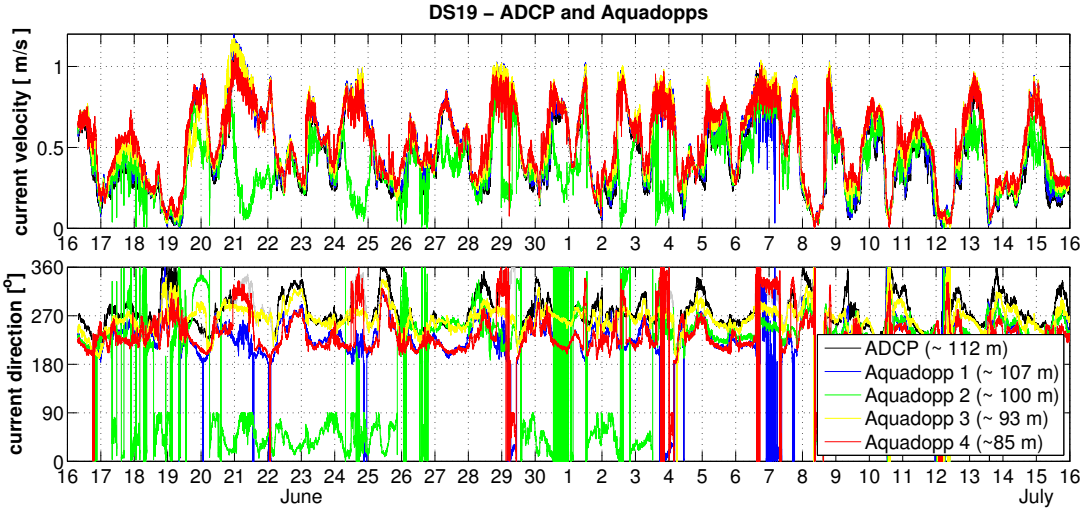

Figure 2.12: ADCP current speed (upper panel) and current direction (lower panel) compared to data collected by the four Aquadopps.

	ADCP correlated with			
	Aquadopp 1 (∼ 100 m)	Aquadopp 2 (∼ 95 m)	Aquadopp 3 (∼ 89 m)	Aquadopp 4 (∼ 82 m)
current velocity	0.9	0.63	0.87	0.83

Table 2.4: Correlation coefficients of the absolute velocity from the ADCP and each Aquadopp.

and the Aquadopps collected during one month after the deployment. All instruments show comparable results in current speed except of the Aquadopp 2. It is suggested that this Aquadopp had a leakage at its deployment which caused errors in the velocity data

especially during the first five days after deployment. Table 2.4 gives the correlation coefficients of current velocities calculated over the whole time series between the ADCP and each Aquadopp. Significant correlation coefficients ($p < 0.05$, two sample student's t-test) between 0.83 and 0.9 in current speed show that the velocity data is consistent. The correlation between the ADCP and Aquadopp 2 is much lower, about 0.63.

The current direction also gives consistent variations in time, but offsets between the data from all devices were detected. Approximately similar values were detected for the ADCP and Aquadopp 3 as well as for the Aquadopp 1 and Aquadopp 4, respectively. The offset between these is $\sim 70°$. Again the Aquadopp 2 performs not as well as all the other sensors. During the first 3 weeks the current direction of Aquadopp 2 showed almost no relation to the data of all other devices. From July 4 the current direction seems to be consistent with the others. As the instruments were placed within 25 m such large velocity shears as indicated by the offsets are physically not plausible. The magnetic field from the batteries might induce errors (Nuno Nunes (UH), personal communication). Freak values might be linked to compass errors which especially arise for situations where the sensors are knocked down.

As the data of the moored current profiler is consistent it provides a reliable dataset to quantify the variability on meso- and sub-meso-scales in the mean working area and a consistent picture of the DSO plume. The ADCP sampled with the smallest sampling rate of 5 s (see Table 2.3) and thus is considered for further analysis.

2.4.3 Comparison of moored with LADCP current measurements

The moored ADCP (DS19) current measurements are fixed in space and yield data only over a vertical range of 37 m. The LADCP profiles observed within the mean working area were often collected closer to the AUV dives and provide data of the whole water column with a vertical resolution of 10 m. Combining both velocity data sets can help to obtain more detailed conditions of the velocity field during the AUV dives. Here the consistency of both datasets is tested.

The ADCP based velocity time series is compared to LADCP data obtained at stations inside the mean working area (Fig. 2.13). Nominally the ADCP had been placed at about 112 m above the seafloor. In order to cover this depth level the LADCP data is given from about 120 m (red dots) and 100 m (yellow dots) above the seafloor. Even though the LADCP stations were not exactly at the mooring site, current speed and direction both show comparable values to the data collected by the ADCP.

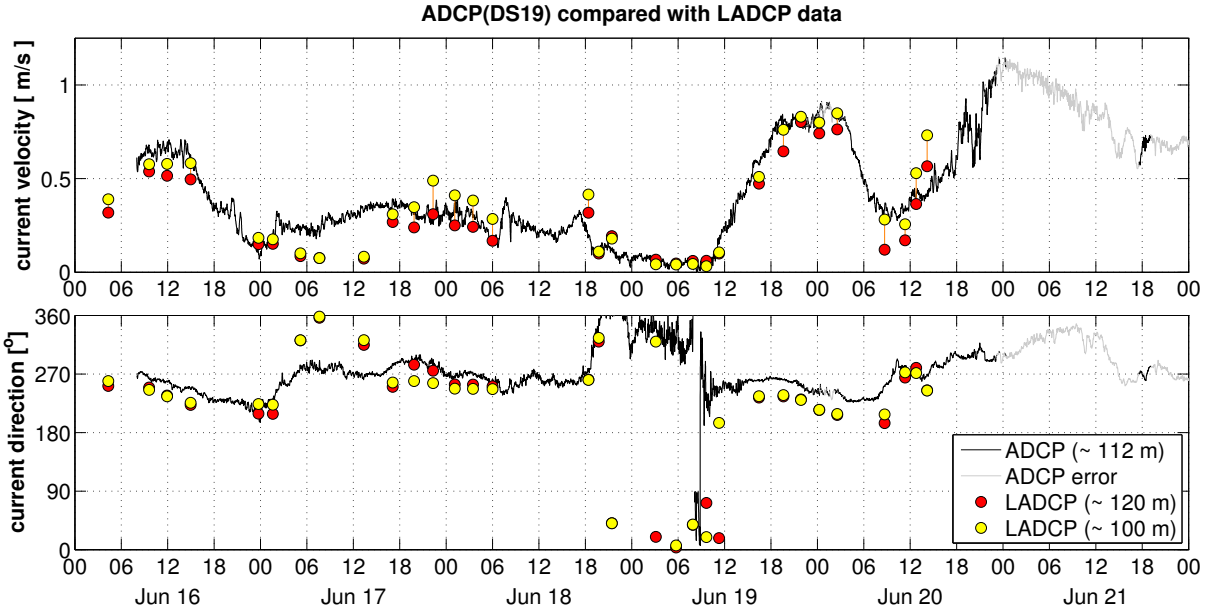

Figure 2.13: ADCP current speed (upper panel) and current direction (lower panel) compared to LADCP data from about 120 m (red) and 100 m (yellow) above the seafloor at CTD stations inside the working area (see map in Fig. 2.2).

2.5 Time series analysis

Time series analysis is a powerful tool to analyze time and length scales of variability. In this study, it is applied to analyze small-scale variability from temperature and salinity data of the AUV-CTD and meso-scale variability from the moored velocity data. The theory given below is based on lecture notes of *Dommenget* (2008, pp. 69-70), literature of *Emery and Thomsen* (2001, pp. 404-417) and *Torrence and Compo* (1998).

Spectral analysis

Spectral analysis is based on the idea that a stationary time series $x(t)$ can be decomposed into a combination of sines and cosines with random coefficients A and B. A periodic time series can be given by

$$x(t) = Asin(2\pi\omega t) + Bcos(2\pi\omega t) \tag{2.1}$$

where A and B are uncorrelated, ω is the frequency, the mean of $x(t)$ is zero, and the variance of the time series equals one. The autocovariance of the time series is given by the sum of sinusoids with corresponding frequencies by

$$x(t) = \sum_{j=1}^{k}(A_j sin(2\pi\omega_j t) + B_j cos(2\pi\omega_j t)). \tag{2.2}$$

This is the Fourier representation of a time series. The power of $x(t)$ is gained by adding up all contributions of each frequency component ω_j. Computation yield that the power is simply given by the Fourier coefficients with $\frac{1}{2}(A^2 + B^2)$.

Considering the same time series with a time lag of τ, the autocovariance γ of $x(t)$ with $x(t + \tau)$ is given by

$$\gamma(\tau) = \sum_{j=1}^{k} (A_j^2 + B_j^2) cos(2\pi\nu_j\tau) \tag{2.3}$$

The Wiener-Khinchin theorem directly relates the autocovariance function to the power spectrum via the Fourier transform. The Fourier transform is the transform from time to frequency domain. Thus the power spectrum (PS) of the time series $x(t)$ is the Fourier transform of the autocovariance function γ:

$$PS(\omega) = \sum_{\tau=-\infty}^{\infty} \gamma(\tau) exp(-i2\pi\tau\omega) \tag{2.4}$$

for all $\omega \in$[-$\frac{1}{2}$, $\frac{1}{2}$]. Here the largest frequencies that a time series with a time step 1.0 can resolve is $\omega = \frac{1}{2}$. Since γ is an even function of τ

$$PS(\omega) = \gamma(0) + 2 \sum_{\tau=1}^{\infty} \gamma(\tau) cos(2\pi\tau\omega) \tag{2.5}$$

This definition of the spectrum is similar to the definition of the covariance between $\gamma(\tau)$ and $cos(2\pi\tau\omega)$. The spectrum can therefore be interpreted as the covariance between the autocovariance function and the cosine function at different frequencies. If the $\gamma(\tau)$ projects well onto a specific cosine-function, than this frequency will be the dominant frequency of the spectrum.

The spectrum is continuous and describes the distribution of variance across time scales. In particular the variance of the time series $Var(x(t))$ equals the integral of the spectrum over various frequency bands

$$Var(x(t)) = \gamma(0) = 2 \int_0^{\frac{1}{2}} PS(\omega) d\omega \tag{2.6}$$

This is known as the power spectral density (PSD) and describes how the spectrum decomposes energy into different frequency components.

Here PSDs have been calculated with a Matlab routine provided by Johannes Hahn (GEOMAR). This routine is based on the Matlab routine 'spectrum_n.m' following the standard method of a power spectral analysis (*Emery and Thomsen*, 2001, pp. 417-425). In praxis the PSD of a signal vector is estimated using Welch's averaged periodogram

method. Depending on the problem the signal can be divided into a chosen number of overlapping[9] sections. The spectrum of the time series is calculated from the Fast Fourier transform. Herein the Fourier coefficients are assumed to be chi-square distributed.

The achieved spectrum represents the distribution of energy across different time scales. For example a record of temperature over a period of time can be converted to a frequency spectrum by the standard methods of power spectral analysis. The PS shows how variations at different frequencies $\omega = \frac{2\pi}{\Delta t}$ (where Δt is a time scale) contribute to the variance of temperature. Similarly this can be applied to spatial scales. Here spectral analysis will yield a spatial spectrum PS(k) where $k = \frac{2\pi}{\lambda}$ is the wave number corresponding to the spatial scale λ. In practice it is rather difficult to measure spatial coordinates. Thus a frequency spectrum at a fixed point is commonly transformed into a wave number spectrum based on the Taylor hypothesis (e.g., *Simpson and Sharples* (2012, pp. 121-122) and references therein). Here a spatial pattern cannot evolve in time as the temperature fluctuations are assumed to be swept past a fixed sensor as a frozen field. This is only valid when the mean flow is large compared to the variance of the fluctuations. The spatial and time scales are then simply related through the advection in the mean flow at speed U by

$$\Delta t = \frac{\lambda}{U}, \omega = \frac{2\pi}{\Delta t} = \frac{2\pi U}{\lambda} = kU. \tag{2.7}$$

This relation can be used to convert the frequency PS into the wave number PS. In this study this is applied to spectral analysis of temperature fluctuations of the AUV (chapter 5). The vehicle dives with a speed of about 1.6 $\frac{m}{s}$ through the water (see section 2.2.3). Thus the velocity of the vehicle is suggested to be large compared to the fluctuations and can be used for the transformation from time to spatial scales.

Wavelet analysis

Wavelet analysis is applied to the CTD temperature and salinity time series of the horizontal AUV tracks to study the amplitude of small-scale hydrographic variability within the time series and how this amplitude varies with time. The idea of wavelet analysis is to decompose a time series into time and frequency space simultaneously (*Torrence and Compo*, 1998). This allows a detailed study of non-stationary time-dependent signals.

The wavelet W_n of a discrete time series $x_{n'}$ is the convolution of x_n with a scaled wavelet function Ψ:

$$W_n = \sum_{n'=0}^{N-1} x_{n'} \Psi \left(\frac{(n'-n)\delta t}{s} \right) \tag{2.8}$$

[9]The standard overlap is 50 %.

where the wavelet power spectrum is defined as $|W_n(s)|^2$. Typically a Morlet wavelet is

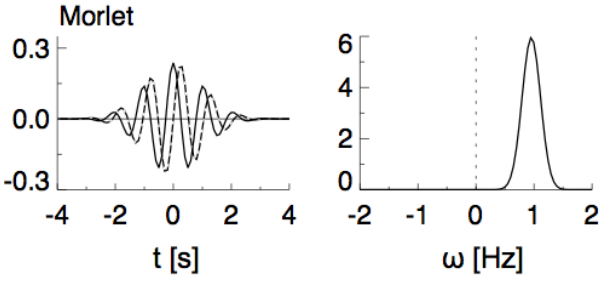

Figure 2.14: Morlet wavelet. The left plot gives the real part (solid) and imaginary part (dashed) for the wavelet in the time domain. The plot on the right gives the corresponding wavelet in the frequency domain (scaled by $10\delta t$). From *Torrence and Compo* (1998) (edited).

chosen for the mother Wavelet function Ψ (Fig. 2.14). It corresponds to the product of an exponential wave and a Gaussian envelop (Fig. 2.14, left). Its mean is zero and the function is localized in both time and frequency space. It has the advantage of incorporating a wave of certain period and being finite in extent. Thus edge effects as introduced by a window function can be avoided. By varying the scale s and going along the localized time index n the resulting image shows both amplitudes of any frequency pattern and how these amplitudes vary with time. A two-dimensional picture of the variability can be constructed by plotting the wavelet amplitude and phase (an example is given below in Fig. 5.11). The sum of energy at each time step over the whole time range gives the total energy on each frequency band, named global wavelet power spectrum.

Here a Matlab routine provided by Johannes Hahn (GEOMAR) based on the practical guide from *Torrence and Compo* (1998) is used to estimate the variance preserving wavelet transforms of temperature and salinity time series.

Chapter 3

Theoretical background: Small-scale turbulence in the ocean

Based on the horizontal profiling measurements of the AUV the aim is to study small-scale variability associated with mixing in the DSO plume. In the following a short overview of the energetics of turbulence and spectral subranges of turbulent motion in the ocean will be given. The theory is based on the literature of *Thorpe* (2005, pp. 19-29, 80-104, 172-184) and *Simpson and Sharples* (2012, pp. 115-127) and references therein.

3.1 Turbulence and dissipation

Turbulence is known as an energetic, rotational, and eddying state of motion. By this momentum, heat, and solutes are transported at rates clearly exceeding those of molecular processes. It is characterized by generating relatively large gradients of velocities at small-scales (a few millimeters). Turbulence involves the transfer of energy from large-scale motion through a series of smaller eddies to scales at which energy is converted to heat by molecular friction known as the forward energy cascade (see below in chapter 3.2). Thereby it promotes conditions in which relatively rapid viscous dissipation transfers kinetic energy of turbulent motion into heat. The transport of energy from small-scale motion to large-scales is known as the inverse energy cascade, which is not considered here.

The transition from a laminar to a turbulent flow was first studied by Reynolds (*Thorpe*, 2005). In the classic Reynolds experiment water is pushed through a long pipe. By increasing the average velocity the destabilizing force of inertia will increase. At a critical value it will overcome the stabilizing force of viscosity and initialize turbulence.

The Reynolds number expresses the balance of the inertial force and the viscosity ν by

$$Re = \frac{Ud}{\nu}. \tag{3.1}$$

where U is the velocity of the flow and d is the diameter of the pipe. The kinematic viscosity ν has a typical value of $10^{-6}\frac{m^2}{s}$. If $Re \gg 1$ a disturbance can propagate to the pipe wall. Otherwise it will be eliminated by viscosity and turbulence cannot expand over the entire flow. In the ocean, the water depth may be taken as the relevant length scale. In a homogeneous ocean the Reynolds number would be very large (U = O(10^{-1})$\frac{m}{s}$, d = O(10^3)m gives Re = O(10^8)) and turbulence would dominate everywhere. The real ocean is stratified and buoyancy rather than viscosity determines the onset of turbulence. The buoyancy acts to suppress turbulence by extracting kinetic energy from the flow through vertical mixing. The stratification is described by the buoyancy frequency:

$$N^2 = -\frac{g}{\rho}\frac{\partial \overline{\rho}}{\partial z} \tag{3.2}$$

where g is the gravitational acceleration and $\frac{\partial \overline{\rho}}{\partial z}$ is the mean vertical density gradient of the water column. The larger N the faster a vertically displaced particle will get back to its initial position. Thus for weak stratification it is easier to initiate turbulence. To sustain turbulence the total energy supply by the velocity shear ($S_v = \frac{\partial U}{\partial z}$) of the mean flow must outcompete the influence of stratification. The balance of the buoyancy versus the shear production of turbulence is commonly described by the Richardson number:

$$Ri = \frac{-\frac{g}{\rho}\frac{\partial \overline{\rho}}{\partial z}}{(\frac{\partial U}{\partial z})^2} = \frac{N^2}{S_\nu^2} \tag{3.3}$$

Starting from an initial laminar motion the necessary condition for the development of turbulence is $Ri < 0.25$. Experiments of stability analyses of shear flows showed that for these critical values the growth of instability is possible. The generation of more or less regular train billows is assumed to be the most relevant mechanism involved in the transfer of momentum and energy into the turbulent velocity field (see Fig. 3.1).

In the stratified ocean interior most often internal waves mediate mixing. The internal wave shear (i.e., the vertical gradient of horizontal velocities) counteracts the stabilizing effect of density stratification. Kelvin-Helmholtz (KH) instability characterized by the development of distinct finite-amplitude billows generates turbulence at critical Ri.

A more general description of the mechanisms transporting, generating and eroding

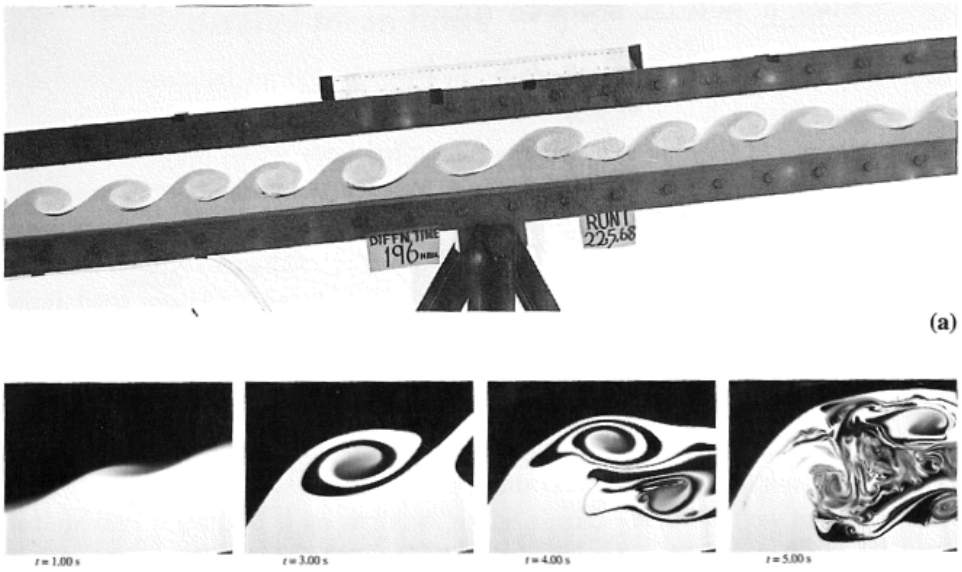

Figure 3.1: Snapshots of a tank experiment studying the development of turbulence through the formation of billows. By tilting the tank the fluid accelerates and billows develop (top panel). The lower panel shows different stages in the transition to turbulence in a stratified fluid. From *Thorpe* (2005, p. 94).

turbulent kinetic energy (TKE) is given by the TKE-equation. The TKE is expressed by

$$TKE = \frac{1}{2}(u'^2 + v'^2 + w'^2) \tag{3.4}$$

where u', v' and w' describe velocity fluctuations in the three dimensional space domain. It can be changed by advection and diffusion and can be produced and dissipated in the fluid motion. The TKE-equation is studied in a local equilibrium by assuming steady state ($\frac{\partial TKE}{\partial t} = 0$) and neglecting diffusion. Herein the turbulent kinetic energy is produced and consumed in the same location by dissipation and mixing given by:

$$\underbrace{N_z \left[\left(\frac{\partial U}{\partial z} \right)^2 + \left(\frac{\partial U}{\partial z} \right)^2 \right]}_{P} + \underbrace{\frac{K_z g}{\rho_0} \frac{\partial \overline{\rho}}{\partial z}}_{B} - \epsilon = 0. \tag{3.5}$$

The energy supply by velocity shear is discribed by the production term (P). The mixing term (B) expresses the work done against or by buoyancy forces and ϵ is the rate of dissipation of kinetic energy by the turbulent motion.

In other words ϵ is the rate of loss of the kinetic energy of the turbulent motion per unit mass through viscosity (ν) to heat and can be expressed as

$$\epsilon = \frac{\nu}{2} \langle s_{ij} s_{ij} \rangle. \tag{3.6}$$

Based on the velocity components (u_1, u_2, u_3) in three orthogonal directions (x_1, x_2, x_3) the tensor s_{ij} is given by

$$s_{ij} = \left(\frac{\partial u_i}{\partial x_j} + \frac{\partial u_j}{\partial x_i} \right). \tag{3.7}$$

The products in Eqn. (3.6) are taken over repeated suffixes from $i, j = 1 - 3$. The spatial gradients imply that the rate of loss of energy is enhanced by high rates of velocity shear which can be generated by small-scale eddying motion of turbulence. From measurements of dissipation and buoyancy frequency the eddy diffusivity can be estimated based on the Osborn method (e.g., *Paka et al.* (2013)). Thus the turbulent dissipation rate can be linked to enhanced diapycnal mixing and can be a measure for entrainment by diapycnal mixing, which is used in this study. In the turbulent ocean the dissipation rate is in the range of about $10^{-10} \frac{W}{kg}$ in the abyssal plains (in the absence of rough topography) and $10^{-1} \frac{W}{kg}$ in the most active turbulent regions. Such highly turbulent regions are found in surf zones or fast tidal currents through straits, for instance.

The rate of loss of temperature variance is the related parameter dicribing the effect of turbulence on the fluid temperature field. It leads to a smoothing of the temperature field by mixing. Assuming an isotropic temperature field the rate of loss of temperature variance (χ_T) is given by the mean square gradients of temperature

$$\chi_T = 6\kappa_T \left\langle \left(\frac{\partial T'}{\partial z} \right)^2 \right\rangle \tag{3.8}$$

where κ_T is the molecular thermal diffusivity coefficient (about $1.4 \cdot 10^{-7} \frac{m^2}{s}$ in seawater) which describes the molecular conductivity of heat. In the ocean χ_T ranges from $(7 \cdot 10^{-10}) \frac{(^\circ C)^2}{s}$ to $(10^{-4}) \frac{(^\circ C)^2}{s}$. High values are found in regions with energetic turbulence and strong stratification.

There are different ways to estimate ϵ as well as χ_T. The rate of loss of temperature variance χ_T can be directly estimated from fast thermistors. The most direct measurements of the turbulent dissipation rate ϵ is given by shear-probes. From MS measurements ϵ can be derived by

$$\epsilon = \frac{15}{2} \nu \left\langle \left(\frac{dw}{dx} \right)^2 \right\rangle \tag{3.9}$$

where $\langle ... \rangle$ represents the average value of variance of any spatial derivative of a velocity component in a direction normal to it. Another indirect method to estimate ϵ is based on comparing observed wave number spectra of velocity to the theoretical universal spectrum in the inertial sub-range of turbulence. The theoretical background for this indirect method will be described in the following section 3.2.

The advantage of horizontal profiling is that it is expected to identify turbulence and

internal waves better on horizontal scales than on vertical scales due to the aspect ratio. Thus it provides the possibility to use less-specialized vehicles and sensors to determine turbulent dissipation rates in the ocean (*Klymak and Moum*, 2007a). The AUV measurement system used in this study equipped with a regular CTD and turbulence probes provides the instrumentation to test this method.

3.2 The Kolmogorov energy cascade

Andrey Kolmogorov proposed that the kinetic energy in the ocean and atmosphere is transferred between different scales of motion through a wave number spectrum of velocities. The spectrum (see chapter 2.5) describes how energy is transported along decreasing length scales from large-scale motion via small-scale eddies to turbulent motion, which eventually is dissipated to heat on the lowest length scales. The spectrum of kinetic energy is associated with a single component of velocity fluctuations. Thus multiple steps of this energy cascade can be studied using spectra of velocity variations. Summing up the spectrum over all k yields the total TKE:

$$TKE = \frac{1}{2}(u'^2 + v'^2 + w'^2) = \int_0^\infty \Phi_u(k)dk. \tag{3.10}$$

Herein, Φ_u is the velocity spectral density which describes the amount of energy per unit mass within a wave number interval dk.

Wave number spectra of velocity (Φ_u)

In general the forward energy cascade covers three regimes (I-III) (see Table 3.1).

I. The first regime is characterized by an energy input through a strong mean flow. Following the forward energy cascade the energy is transferred from the large-scales of the mean flow via eddies of decreasing size to smaller scales. As discussed before, in stratified conditions the vertical extension of eddies is opposed by buoyancy forces. Thus the maximum wave number is reached when the TKE is completely converted to potential energy in the overturning motion. The Ozmidov length scale L_O expresses this limiting scale on dimensional grounds by

$$L_O = \left(\frac{\epsilon}{N^3}\right)^{\frac{1}{2}}. \tag{3.11}$$

Thus the regime covers small wave numbers of $k \leq k_O$ corresponding to large time and length scales ($L \geq L_O$). As large eddies are strongly influenced by currents, the motion is anisotropic (i.e., the spectrum is dependent on the direction of the wave number vector). As observed spectra would depend on the sampling no equilibrium spectrum can be defined.

	velocity spectrum Φ_u $[(\mathrm{m/s})^2\ \mathrm{cpm}^{-1}]$	temperature spectrum Φ_T $[(^\circ C)^2\ \mathrm{cpm}^{-1}]$	isothermal slope spectrum $\Phi_{d\zeta/dx}$ $[\mathrm{cpm}^{-1}]$
I.	**large-scale anisotropic motion**		
	-	-	I(i). internal wave subrange $\Phi^{IW}_{d\zeta/dx} \approx \Phi_0 k^{-1/2}$
II.	**inertial subrange of turbulence**		
		II(i). inertial-convective subrange	
	$\Phi^{IC}_u = A\epsilon^{2/3}k^{-5/3}$	$\Phi^{IC}_T = B_1\chi_T\epsilon^{-1/3}k^{-5/3}$	$\Phi^{IC}_{d\zeta/dx} = C_1\chi_\zeta\epsilon^{-1/3}k^{1/3}$
	more general:	- - - - - - - - - - - - - - -	- - - - - - - - - - - - - - -
		II(ii). inertial-diffusive subrange	
	$\Phi_u = F(k\eta_\nu)\epsilon^{2/3}k^{-5/3}$	$\Phi^{ID}_T = B_2\chi_T\nu^{1/2}\epsilon^{-1/2}k^{-1}$ (*Batchelor spectrum*)	$\Phi^{ID}_{d\zeta/dx} = C_2\chi_\zeta\nu^{1/2}\epsilon^{-1/2}k$
III.	**viscous-diffusive subrange**		

Table 3.1: Universal equilibrium spectra for velocity Φ_u (*Simpson and Sharples* (2012, p. 123) and references therein), temperature Φ_T (*Grant et al.* (1968) and citations), and isothermal slope $\Phi_{d\zeta/dx}$(*Klymak and Moum*, 2007a) all related to the horizontal wavenumber $k = k_x$ (isotropic motion). k defines the slope of the spectra. A, B, and C are empirical constants and yield in combination with ν, χ, and ϵ the amplitude of the spectra, respectively.

II. At higher wave numbers it can be assumed, that towards the transition to turbulence the motion becomes independent of the direction of the large-scale motion as the disorder increases more and more. Assuming a steady state (i.e., frozen turbulence) and isotropy (i.e., motion is independent from a direction) for uniform turbulent motion allows one to describe the TKE transfer through equilibrium spectra at wave numbers in the range of $k_O \ll k \ll k_\nu$ (regime II). In the ocean the so-called *inertial subrange of turbulence* extends from a millimeter (shelf seas) up to a maximum scale limited either by stratification or boundaries. In the inertial-subrange the slope of the equilibrium spectrum of velocity is found to be proportional to $k^{-5/3}$ (Table 3.1). The amplitude of the spectrum is set by ϵ.

With increasing wave numbers the velocity fluctuations disappear more and more and viscosity becomes important. The scales corresponding to this part of the spectrum are

known as the Kolmogorov micro-scales (small structures) given by

$$\eta_\nu = \left(\frac{\nu^3}{\epsilon}\right)^{\frac{1}{4}} \tag{3.12}$$

As dissipation extracts energy from the spectrum, Φ_u falls increasingly below the $k^{-5/3}$ form. This is decribed by an additional factor $F(k\eta_\nu)$ in the universal spectrum (Table 3.1).

III. The energy transfer continues until the eddies are so small that k approaches scales ($k \rightarrow k_\nu$) at which viscous forces cause the mean kinetic energy to be converted to heat in the so-called *viscous-diffusive subrange* (see Table 3.1).

Spectra of velocity shear from AUV-MSP measurements were used to estimate ϵ by a fit to the equilibrium spectrum of the inertial subrange of turbulence (II), the ‚Nasmyth universal spectrum'. For a reliable estimate of ϵ it is of interest to cover best the inertial subrange. At lower wave numbers internal waves govern the turbulent motion. The aspect ratio of horizontal vs. vertical wave numbers for internal waves is generally much smaller than 1. Thus internal waves can be better separated from turbulence using horizontal rather than vertical measurements. This may give the opportunity to look further into the turbulent regime probably even with temperature data from a regular CTD (*Klymak and Moum*, 2007a).

Wave number spectra of temperature (Φ_T)

Instead of studying velocity variations, turbulence spectra for scalar properties such as temperature in the ocean can be derived and thus applied to e.g., AUV-CTD data. This is based on the fact that turbulent motion generates small-scale fluctuations in scalar properties. Assuming isotropy, the spectrum of temperature fluctuations is given by

$$\overline{T'^2} = \int_0^\infty \Phi_T(k)dk. \tag{3.13}$$

Figure 3.2 illustrates the main regimes of the Kolmogorov energy cascade applied to a temperature spectrum. Based on the theoretical studies by Batchelor (*Grant et al.*, 1968) the temperature spectra in the inertial subrange can be separated into two parts (II(i) and II(ii), Table 3.1, Fig. 3.2).

II (i). At small wave numbers the spectrum is parallel to the velocity spectrum ($k^{-5/3}$). This part is named the *inertial-convective subrange* (i). The amplitude of the temperature spectrum depends on ϵ and the temperature gradient via χ_T (Fig. 3.2, Table 3.1), (*Grant et al.*, 1968).

II (ii). At larger wave numbers viscosity becomes important. In the so-called *inertial-diffusive subrange* (Fig. 3.2) the universal spectrum was found to have a slope of k^{-1}

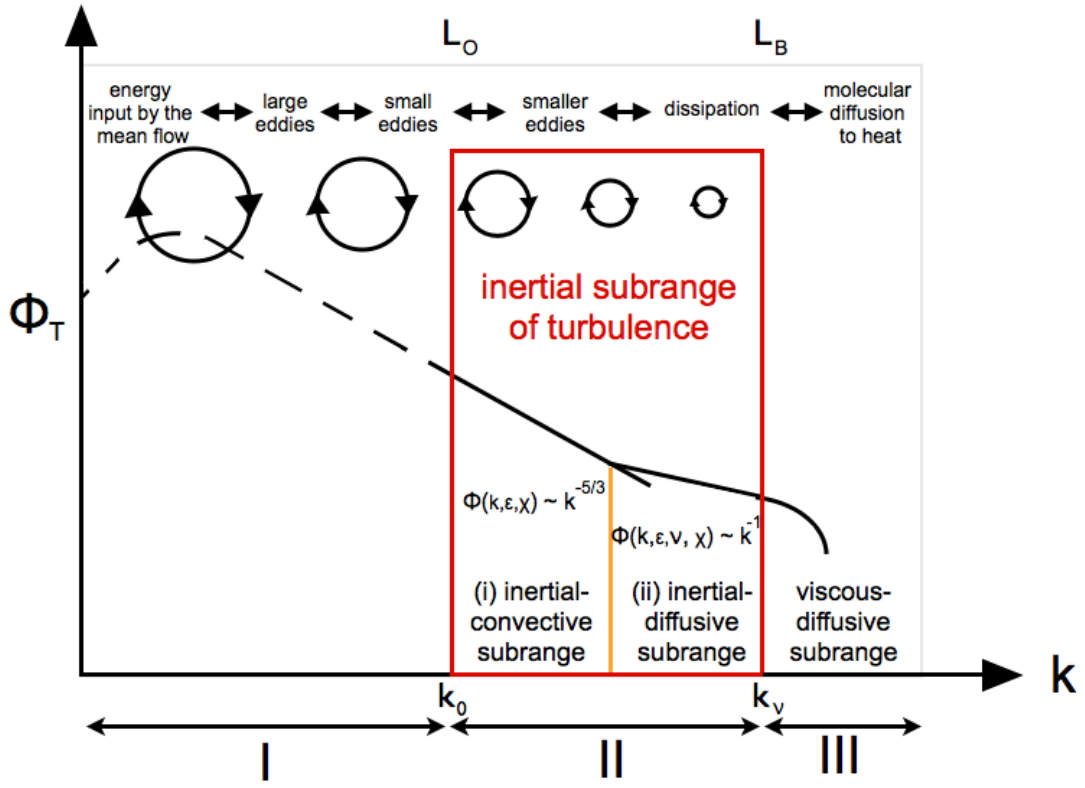

Figure 3.2: Sketch of the energy cascade via a temperature spectrum (Φ_T) based on the hypothesis of Kolmogorov and theoretical studies of Batchelor. In the top the length scales of motion (L_O, L_B) and governing physical processes are given. The curve gives the universal wave number spectrum of temperature found in the ocean. The inertial subrange of turbulence is highlighted by the red box. This is separated by the orange line in two regimes given with distinct spectral slopes of Φ_T. At larger wave numbers the viscous-diffusive subrange covers the regime where temperature is diffused to heat.

(Table 3.1). The Batchelor scale for temperature

$$L_B = \left(\frac{\nu D_T^2}{\epsilon}\right)^{1/4} \tag{3.14}$$

(where D_T describes the molecular diffusion) sets the upper limit of the inertial subrange.
III. For larger wave numbers (length scales are smaller than L_B), in the *viscous-diffusive subrange*, primarily D_T eliminates the temperature gradients.

This form of the energy cascade was confirmed by many spectra observed in the atmosphere and ocean (e.g. *Grant et al.* (1968)). At small scales temperature and velocity fluctuations are found to be dominated by turbulence.

Wave number spectra of isothermal displacement ($\Phi_{d\zeta/dx}$)
The disadvantage of temperature spectra is that due to the varying background stratification the derived turbulence levels cannot be compared to other experimental settings

directly. The background stratification can be eliminated by the use of the isotherm displacement instead of temperature to calculate horizontal wavenumber spectra (*Klymak and Moum*, 2007a). The use of *horizontal* (rather than vertical) wavenumber spectra of *isothermal slopes* is desirable because it gives the opportunity to see further into the inertial-convective subrange. This is of interest as at intermediate k the internal wave and turbulence spectral subranges overlap.

Horizontal wavenumber spectra of isotherm displacement can be derived as follows. The temperature signal can be converted to vertical displacement by

$$\zeta = z - Z_0(T) \tag{3.15}$$

where Z_0(T) is the inversion of the mean temperature profile T_0(z). The displacement is thus the depth offset of the isotherm from Z_0(T). The assumption is that the background displacement $Z_0(T)$ does not change over the course of the measurements.

Horizontal gradients of vertical isotherm displacement ζ_x yield the slope of the isotherms[1]. *Klymak and Moum* (2007b) found even at low wave numbers (at k shorter than those of the turbulent regime) in the internal wave range a slope spectrum can be relatively well modeled. This is the so-called *internal wave subrange* where $\Phi_{d\zeta/dx}$ is proportional to $k_x^{-1/2}$ (Table 3.1).

II(i). For the *inertial-convective subrange* the strength of turbulent dissipation ϵ and the temperature gradient (contained in χ_ζ, i.e. a scaled version of the dissipation of temperature variance) set the level of the displacement spectrum (Table 3.1). The form is proportional to $k^{1/3}$.

II(ii). At higher wave numbers in the *inertial-diffusive subrange* (Fig. 3.3) the viscosity of seawater becomes important and $\Phi_{d\zeta dx}$ is dependent on k (Table 3.1).

Instead of performing spectral analysis on isotherm slopes, more stable results are obtained by conversion of temperature spectra into isotherm slope spectra by

$$\Phi_{d\zeta/dx}(k_x) = (2\pi k)^2 \left\langle \frac{dT_0}{dz} \right\rangle^{-2} \Phi_T \qquad [cpm^{-1}] \tag{3.16}$$

where $\frac{dT_0}{dz}$ is the background vertical temperature gradient and k is the horizontal wavenumber in cpm (*Klymak and Moum*, 2007b). The equation describes two steps. First, the temperature spectrum is transformed in a temperature gradient spectrum by multiplying with $(2\pi k)^2$. Second, the result is multiplied with $\left\langle \frac{dT}{dz} \right\rangle^{-2}$ to obtain an isotherm slope spectrum in [cpm^{-1}]. The temperature gradient and slope spectra have identical k-dependence, but the slope spectra are shifted to higher wave numbers. Thus the slopes

[1]Neglecting effects of salinity, *Klymak and Moum* (2007b) equated the *isotherm* slope with *isopycnal* slope spectra. Here, the expression *isotherm* slope is kept for precision.

in the isotherm slope spectra are easier to distinguish. This can be seen in the sketch of the inertial wave and turbulent subranges of a slope spectrum based on the work of *Klymak and Moum* (2007b) (Figure 3.3).

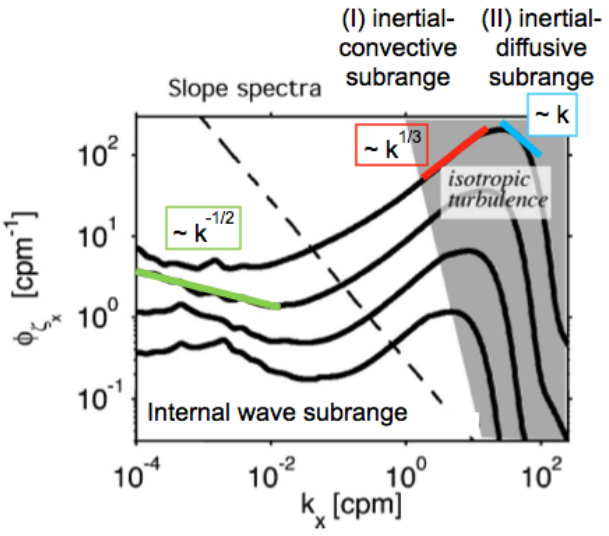

Figure 3.3: Sketch of the slope spectrum marking the subranges of internal waves at low and turbulence at high wave numbers. From *Klymak and Moum* (2007b).

Making use of the suggested high coverage of the inertial-convective subrange based on horizontal profiling, it will be studied if the CTD-based variances from the isotherm displacements can be related to dissipation rates from the high accurate MS measurements of velocity shear.

Chapter 4

The Performance of the AUV missions during June 2012

Commonly used oceanographic instruments provide either high resolution vertical hydrographic and velocity profiles from ship-lowered CTD/LADCPs or Eulerian time series from moored devices. The use of an AUV gives the potential to study high resolved *horizontal* profiles of parameters such as hydrographic data and the dissipation of TKE. With the AUV measurement system small horizontal scales can be resolved which can not be reached by commonly used measurement instruments. This gives, the opportunity to study small-scale turbulent motions even with a regular CTD (*Klymak and Moum*, 2007a). In the following chapter data from the AUV missions carried out in June 2012 (Table 2.1) is presented in order to show the general performance of the AUV. In the beginning the consistency between AUV-based CTD data and lowered CTD data is tested. Afterwards data from three AUV missions are given exemplarily to show different ways of mapping with an AUV, i.e. covering depth levels vs. mapping in a horizontal plane, section length along vs. across topography. The overall aim is to test which mapping mode performed best to capture small-scale variability in the interfacial layer of the DSO plume by horizontal profiling with the AUV.

4.1 Θ-S-characteristics of AUV-based and ship-lowered CTD data

Before the AUV-based hydrographic data is analyzed, the consistency of the data in comparison with lowered CTD data is studied. All AUV missions were carried out within nine days in the main working area (see map in Fig. 2.3, Table 2.1). Additionally during this period of time, 53 ship-lowered CTD profiles close to the AUV tracks were collected at two repeated stations. The Θ-S-characteristics from these profiles are compared to

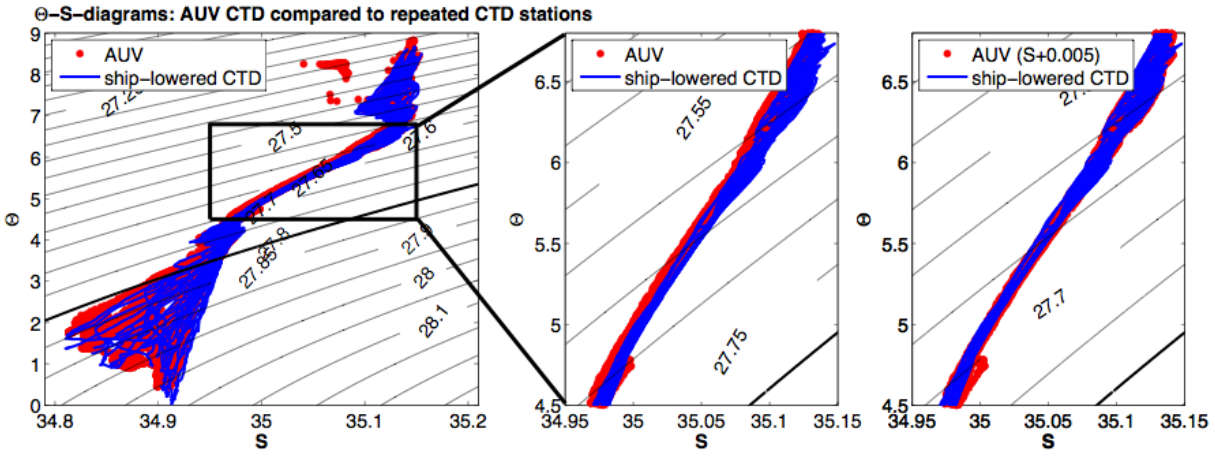

Figure 4.1: Θ-S-diagrams comparing hydrographic data collected during the AUV missions (red dots) with hydrographic data from 53 lowered CTD profiles (blue lines) carried out within the main working area close to the AUV tracks. The left panel shows the whole Θ-S-diagram. The middle panel is a zoom into the linear part of Θ-S-diagram (denoted by the box in the left panel). Note the salinity offset between both datasets. The right panel shows the same as the middle one, but with a salinity offset of 0.005 added to the AUV-CTD.

those relying on AUV-based measurements.

Figure 4.1 (left) shows the obtained Θ-S-diagram of both repeated lowered CTD stations close to the AUV missions (blue lines) and AUV-based CTD data from the deep tracks of all long missions (red points). A small offset to fresher values in the AUV-based CTD data is observed. This is best seen by an expanded view of the part of the Θ-S-diagram with an almost linear relationship at mid-depth (Fig. 4.1, middle). The conductivity sensor of the ship-lowered CTD was calibrated contemporarily using water samples from the Niskin bottles on board MSM21/1b and thus the data is highly accurate (r.m.s.[1] deviation: 0.0014). The conductivity sensor of the AUV-CTD was not calibrated before or after the missions. Thus the salinity data from the ship-lowered CTD measurements can be used to correct the salinity data obtained from the AUV-based CTD. The agreement in the Θ-S-curve of both data sets is visually improved by adding a constant of 0.005 to the AUV-based salinity values (Fig. 4.1, right). Thus a mean offset of -0.005 for the AUV-based CTD measurements is assumed. In the following all AUV-based salinity data include this offset-correction.

Because this study concentrates on dense DSO plume water in a bottom layer, the Θ-S-characteristics at deep levels are compared (Fig. 4.2). For densities larger than 27.75 $\frac{kg}{m^3}$ one class of lowered CTD profiles of the repeated stations merge at a line from about Θ = 4°C / S = 34.97 down to Θ = 0.5°C / S = 34.91 at 28 $\frac{kg}{m^3}$ (see Fig.

[1]root mean square

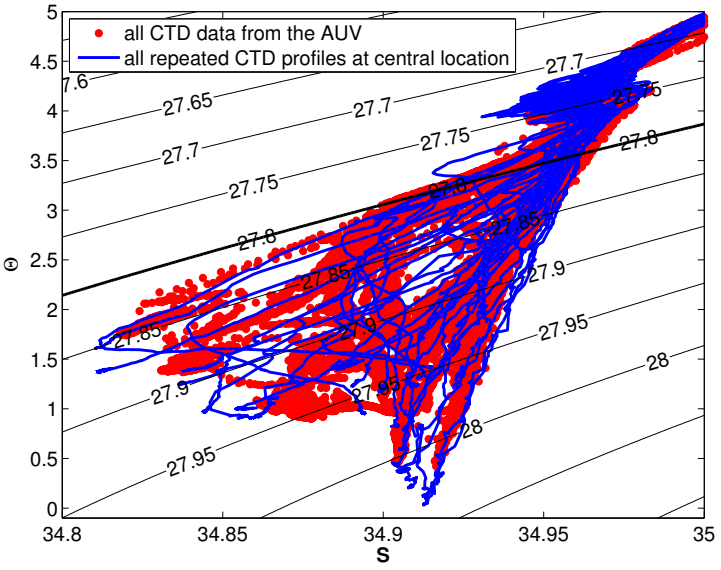

Figure 4.2: Dense part of the Θ-S-diagram shown in Fig. 4.1 (left). An offset of 0.005 has been added to AUV-based CTD data.

4.2). However several CTD profiles show warmer and fresher conditions at depth. The lowest salinity is found close to 34.81. This fresh water shows relatively warm potential temperatures of $\Theta = 1.4-1.6°C$. The spread of the Θ-S curves below the 27.8 $\frac{kg}{m^3}$ contour is equally captured by the AUV-based CTD. Due to the horizontal profiling mode the AUV is able to densely sample the water-mass variability in the depth range were the lowered CTD profiles show a strong spread in Θ-S space. The vertical hydrographic profiles may be regarded as snapshots of the deep hydrographic conditions limited by the distance of the CTD stations. The horizontal measurements of the AUV can help explain the internal scales associated with the changes in water mass characteristics in variable systems. As the AUV-based CTD data is consistent with the lowered CTD data, it can be used to study small-scale variability in the DSO plume, as follows.

4.2 AUV profiles at varying depth levels in the DSO plume

The aim of dives 2 and 6 was to collect horizontal profiles at different depth levels which cover the vertical DSO plume structure, i.e. the plume layer, the interfacial layer, and the ambient water. To achieve this, the AUV has been programmed to dive along the Greenland continental slope with the plume and to follow a chosen isobath at different depth levels above each other (map in Fig. 2.3). The data collected during AUV dive 6 are used exemplarily to analyze the usage of this mode of mapping the DSO plume.

The AUV was following approximately the 1460 m isobath during all tracks of dive

6 (map in Fig. 2.3). The first track was taken about 43 m above the seafloor. After completing a distance of 2 km, the AUV ascended up to 190 m above the seafloor. At this depth level the vehicle returned to the start position to avoid strong counter currents that would have slowed down the vehicle at larger depths. At the northwestern starting point the AUV descended again and started a second track at 67 m above the seafloor traveling in the same direction as the first track. Subsequently, all tracks close to the seafloor started in the NW and with the AUV heading in the along current direction for a distance of 3 km. In total the AUV carried out measurements at five depth levels roughly 50 m above each other (round A). The same pattern was repeated about five hours later (round B).

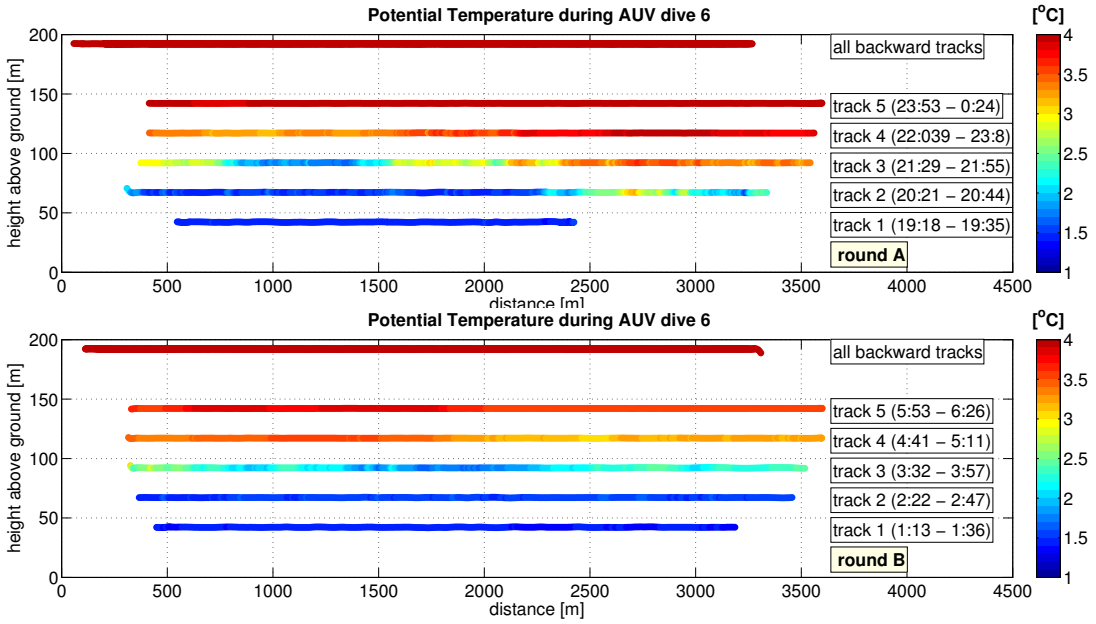

Figure 4.3: Potential temperature from AUV-based CTD measurements during dive 6 as a function of height above the ground and the distance from a fixed south-eastern location. The upper and lower panels show the results from round A and B, respectively, of the measurements taken about 5 hours apart from each other. The start and end times of each track are added in the boxes to the right of each track, respectively.

During both rounds the potential temperature shows mean values of 1.4 °C at the deepest track (track 1) associated with DSO plume water (Fig. 4.3). Water with temperatures warmer than 3.5 °C along the track 5 and the backward tracks (higher than 140 m above the seafloor) can be associated with ambient water. The three tracks in between captured the interfacial layer of the DSO plume indicated by the vertical temperature gradient. Horizontal temperature fluctuations in the range of 1.3 °C and 3.4 °C are observed along tracks 2 and 3 during round A (Fig. 4.3, upper panel). This is also indicated by a high standard deviation of (0.5 / 0.6) °C compared to $std(\Theta) \leq 0.1°C$ in the plume and ambient water (Table 4.1). During round B such strong gradients were not

track	height above ground [m]	Θ [°C]		S		$\sigma_\Theta[\frac{kg}{m^3}]$	
		A	B	A	B	A	B
1	43	1.4 ± 0.0	1.4 ± 0.0	34.90	34.84	27.93	27.89
2	67	1.8 ± 0.5	1.5 ± 0.0	34.90	34.84	27.91	27.88
3	91	2.8 ± 0.6	2.2 ± 0.3	34.94	34.87	27.85	27.86
4	115	3.6 ± 0.3	3.3 ± 0.1	34.96	34.95	27.79	27.81
5	140	3.9 ± 0.0	3.7 ± 0.1	34.97	34.96	27.76	27.79
back	190	4.0 ± 0.1	4.0 ± 0.0	34.97	34.97	27.76	27.76

Table 4.1: Mean values of potential temperature, salinity, and potential density along each track of dive 6. All values are given for both rounds A and B arranged by the track numbers and the corresponding height above ground. The mean values over each round are given for the backward tracks. Additionally, standard deviations are given for the potential temperature.

observed at any depth level. Here the standard deviation at each constant depth level was less than 0.1 °C except for track 3, where the standard deviation amounts to 0.3 °C. A comparison of round A and B (taken about 5 hours apart from each other) shows slightly cooler mean potential temperatures at each depth level 2 to 5 in round B (Table 4.1).

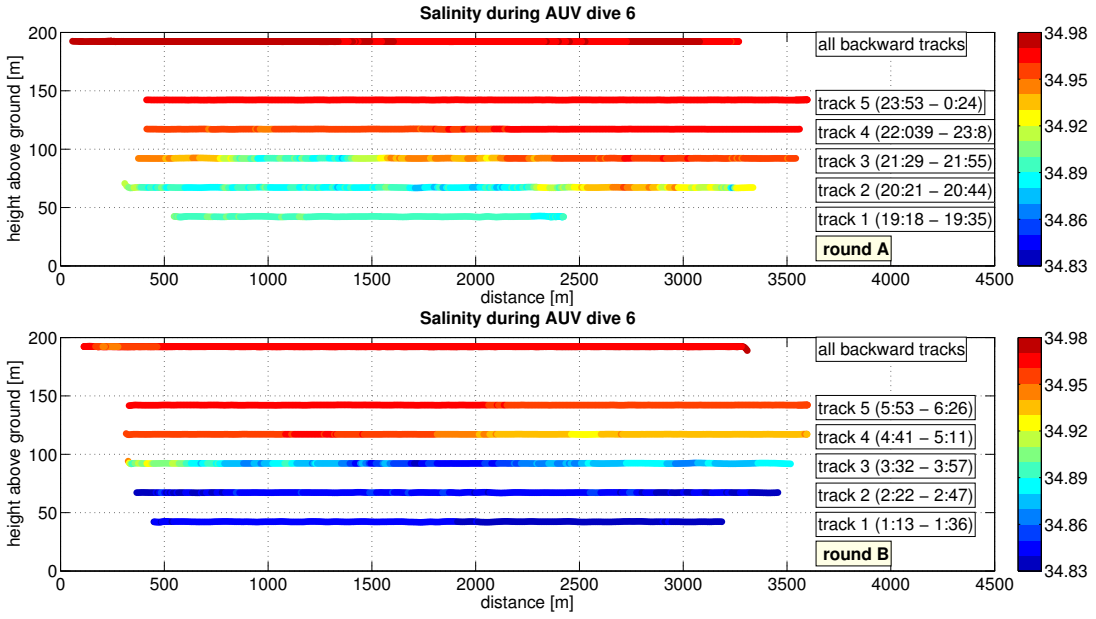

Figure 4.4: Salinity from the CTD attached to the AUV during dive 6. (See caption of Fig. 4.3 for explanation.)

Salinity shows similarly high values in the range of 34.95 - 34.97 along the upper tracks (4, 5 and backwards) (Table 4.1, Fig. 4.4). At deep levels below 100 m above the seafloor (1,2,3) the salinity ranges from 34.88 to 34.94 during round A. During round B fresher conditions were observed with salinities between 34.83 and 34.89. Thus the mean potential density decreases in the mixed bottom layer by 0.04 $\frac{kg}{m^3}$ while it remains about

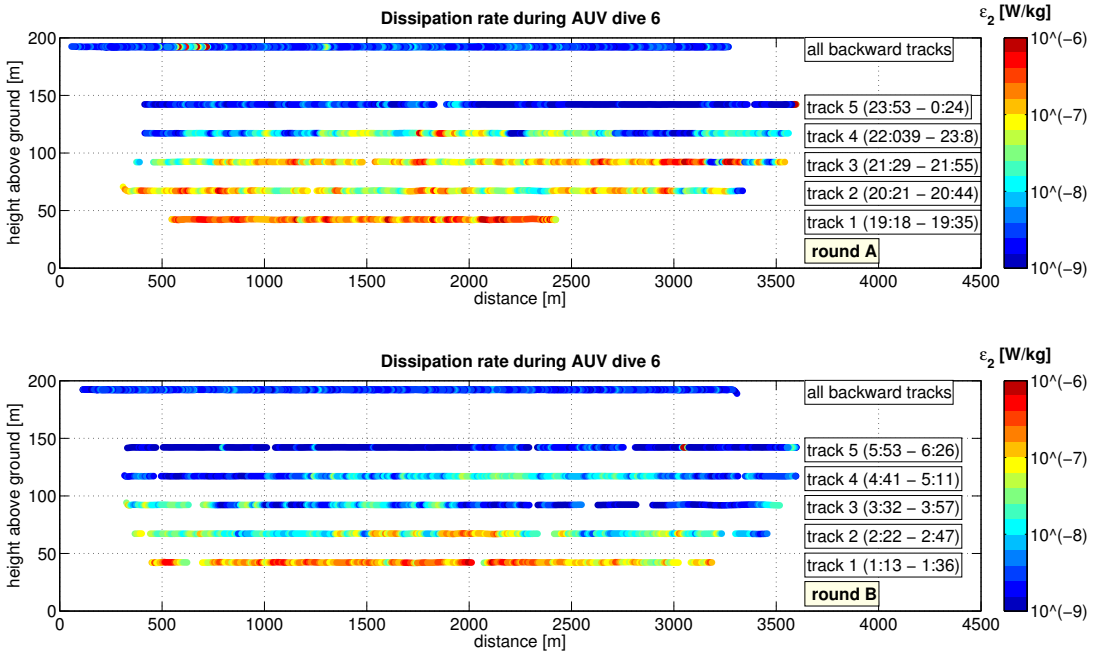

Figure 4.5: Dissipation of TKE from the MR attached to the AUV during dive 6. (See caption of Fig. 4.3 for explanation.)

the same ((27.85 - 27.86) $\frac{kg}{m^3}$) in the interfacial layer (track 3) (Table 4.1).

In addition to the hydrographic data, the AUV-based MS measurements provided data of the dissipation of TKE along the AUV tracks. Both sections show highest dissipation rates close to the seafloor (Fig. 4.5). At the deepest track (track 1) ϵ-values range mainly between O(10^{-7})$\frac{W}{kg}$ to O(10^{-6})$\frac{W}{kg}$ during both rounds. The profiles taken between 67 and 115 m (tracks 2 - 4) cover the whole range of ϵ from O(10^{-9})$\frac{W}{kg}$ to O(10^{-6})$\frac{W}{kg}$. The mean dissipation rates in the ambient water are one to two orders of magnitude lower than in the plume (Table 4.2). In comparison the mean dissipation rates during round A are in the interfacial layer one (track 2, 4) to two (track 3) orders of magnitude higher than during round B (Table 4.2).

track	height above ground [m]	ϵ [$\frac{W}{kg}$]		velocity [$\frac{m}{s}$]	
		A	B	A	B
1	43	O(10^{-7})	O(10^{-7})	0.59	0.50
2	67	O(10^{-7})	O(10^{-8})	0.62	0.52
3	91	O(10^{-7})	O(10^{-9})	0.45	0.47
4	115	O(10^{-8})	O(10^{-9})	0.22	0.22
5	140	O(10^{-8})	O(10^{-8})	0.11	0.07
back	190	O(10^{-8})	O(10^{-9})	-	-

Table 4.2: Mean values of the dissipation rate and current velocities along each track of dive 6. (same as in Table 4.1).

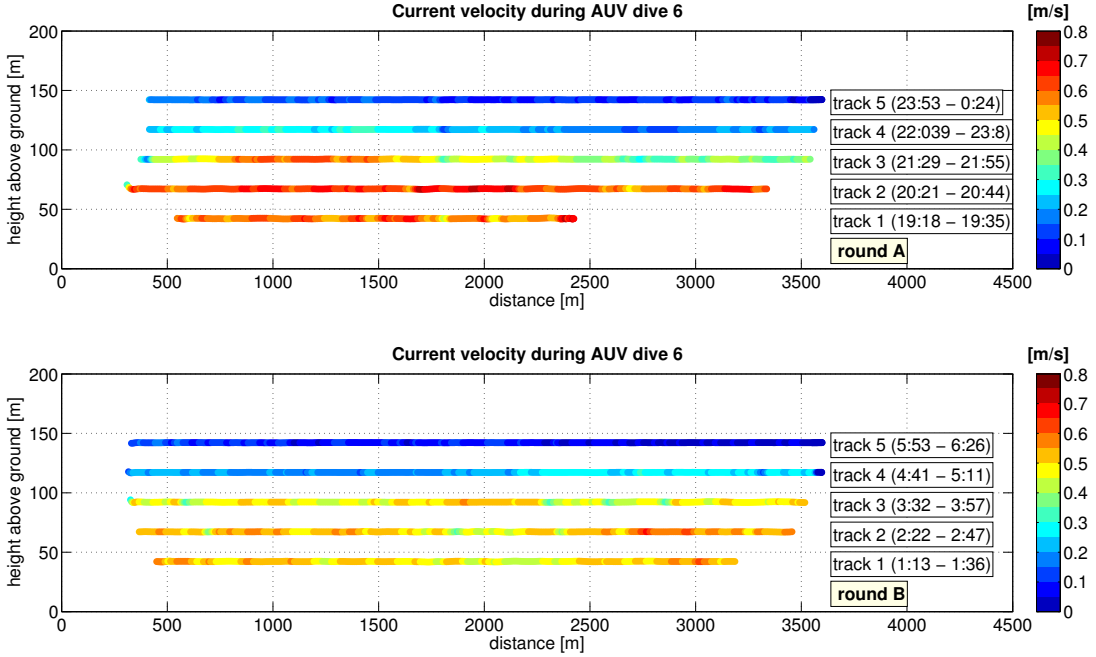

Figure 4.6: Current velocity in the direction of the AUV (downstream) during dive 6. (See caption of Fig. 4.3 for explanation.)

Additional information about the hydrographic and dissipation data can be achieved from the current velocity computed from the AUV (see section 2.2.3). The AUV-inferred current speeds can be assumed to represent the DSO plume velocities as the AUV dives along the topography. A mean plume velocity of 0.6 $\frac{m}{s}$ is observed during round A (Fig. 4.6, upper panel, tracks 1 and 2). The ambient water (track 5) is indicated by very low velocities with a mean velocity of 0.1 $\frac{m}{s}$. The velocity gradient is covered in between this range marking the interfacial layer of the plume. This compares well with the depth of the interfacial layer observed in the hydrographic characteristics. In comparison, the plume velocities 5 hours apart (round B) were on average 0.1 $\frac{m}{s}$ slower.

The data collected from the horizontal profiling AUV during dive 6 provides an insight into the DSO plume characteristics. By covering different depth levels the well-mixed plume layer, the interfacial layer, and the ambient water can be identified. The high resolution horizontal tracks yield information about small-scale variability in each layer, respectively. As the same pattern was covered a second time, temporal variations in the plume conditions were captured as well. Thus this programmed mode can be used in view of DSO plume analyses and entrainment processes.

4.3 AUV-based horizontal mapping

While dives 2 and 6 aimed to map the DSO plume at different depth levels in order to cover its vertical extent, the aim of dives 5 and 7 was to map the interfacial layer of the DSO plume in a horizontal plane. Within these missions the AUV was kept at a constant height above the seafloor along isobaths parallel to each other. This sampling mode was used to carry out horizontal mapping of properties and to repeat those patterns to study the temporal variability.

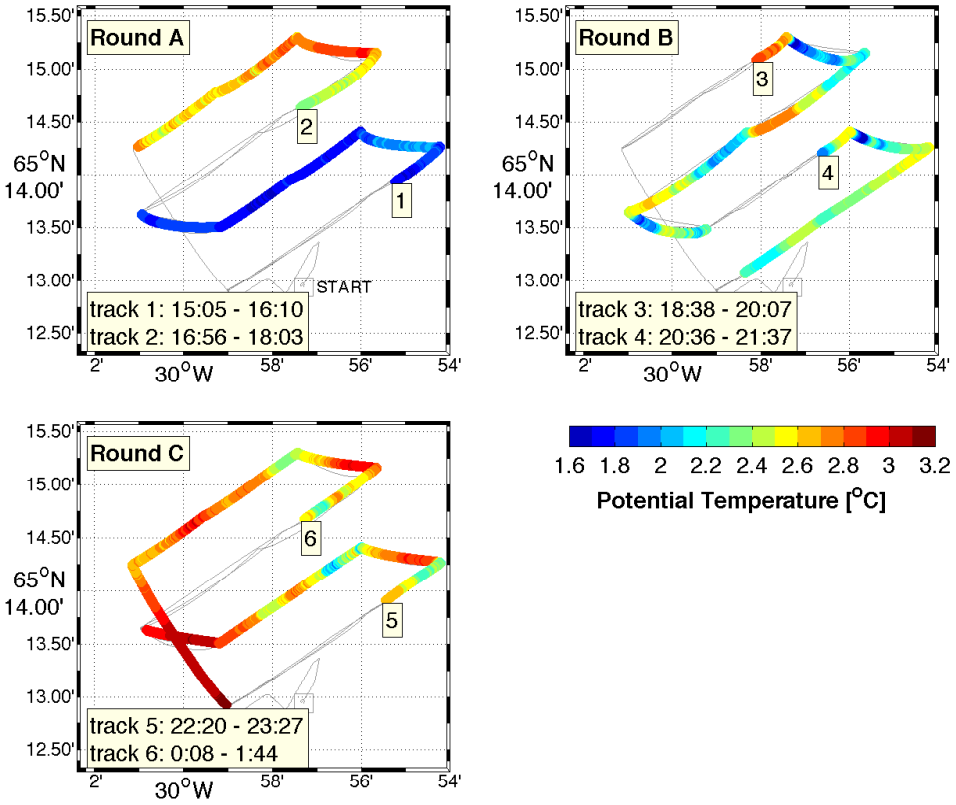

Figure 4.7: Potential Temperature collected at 100 m above the seafloor during dive 5. The same pattern was repeated three times. The upper left panel shows round A. Rounds B and C are depicted in the upper right and lower left panels, respectively. The grey tracks denote times when the AUV was diving 200 m above the seafloor. The starting point of each track is marked and counting upwards from one to six. All tracks lasted about one hour.

The AUV collected data along 4 parallel tracks following approximately the 1470 m, 1440 m, 1410 m, and 1380 m isobaths during dive 5 (map in Fig. 2.3). During tracks in which the AUV was heading NW (opposing the mean flow) it was programmed to dive 200 m above the seafloor. During all other times it stayed at around 100 m above the seafloor, i.e. likely in the interfacial layer between the plume and the ambient water (compare with dive 6). The AUV covered the same pattern three times (round A, B,

C). In rounds A and C the AUV started at the southeastern end of the pattern and in round B it started at the northern end. During all tracks the AUV collected very different temperature characteristics in comparison (Fig. 4.7). For instance, while the mean temperature was (1.8 ± 0.1) °C in track 1, it was (2.6 ± 0.2) °C further north along track 2 (Fig. 4.7, round A). Roughly the same tracks were covered about 7 hours later (Fig. 4.7, round C), whereby mean potential temperatures of (2.6 ± 0.3) °C (track 5) and (2.8 ± 0.2) °C (track 6) were observed. While the temperature within round 1 varied between the southern and northern track by 0.8 °C, it was almost similar in round C. Both tracks showed warmer temperatures compared to round A. The observed temperature anomalies during dive 5 are difficult to interpret due to the method of mapping. The mapping did not succeed neither in time (between the maps) nor in space (within a map between the tracks).

The way of mapping was improved during AUV dive 7. In order to capture variations in a horizontal plane the vehicle first followed five equal, about one-kilometer-long and downstream-oriented tracks. The tracks were parallel to each other with a distance of about 500 m in between. The AUV stayed at a constant depth of 90 m above the seafloor along these tracks. In total the pattern covers an area of 2 km x 1 km. The AUV was programmed to dive back upstream to the starting point of each track at 200 m above the seafloor. The higher depth level was chosen while heading NW was chosen to avoid strong countercurrents causing a time off of the AUV positioning system. In addition, the temporal variability in this area was observed by repeating the same pattern five times (round A to E).

During round A the potential temperature ranged between 3.3 °C and 3.5 °C at all 5 tracks (Fig. 4.8). The potential temperature was slightly higher ((3.7 - 4) °C) along all tracks during round B and C. These high temperatures indicate that the AUV did not catch the interfacial layer, but was rather sampling in the ambient water. In round D a gradient in the potential temperature from north to south is observed. At the southernmost location the water had temperatures of 4 °C, comparable to those during rounds B and C. Towards the north a slight cooling down to 3 °C is detected. In round E an even stronger gradient is observed from 3.6 °C in the south down to 2 °C in the north.

Changes in the salinity can be seen during the same time. In round A the salinity varies only slightly between 34.93 and 34.95. The tracks during rounds B and C show similar salinities of (34.96 ± 0.05). In round D the salinity ranges between 34.65 in the south and 34.94 in the north. Round E shows even fresher values between 34.95 in the south and 34.92 in the north.

Thus changing patterns can be observed and can be linked to DSO plume dynamics within a map as well as between the maps. Additional information for the physical interpretation of the observed changes is given e.g., by the along-stream current velocity

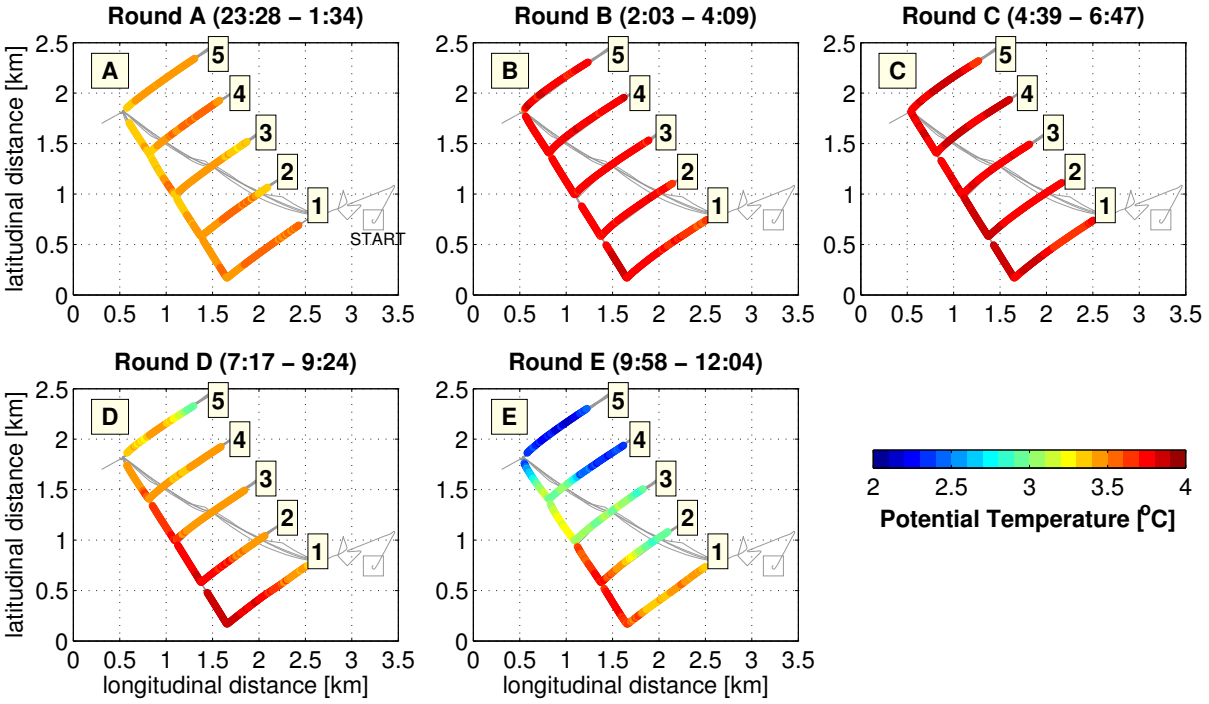

Figure 4.8: Potential temperature along AUV tracks during dive 7 observed 90 m above the seafloor. The pattern was repeated five times. Each panel, A to E, shows a map of the tracks 1 to 5 and the start and end times of each round are given in the titles. The axes are given in distances relative to a SW location at 30°W and 65.23°N.

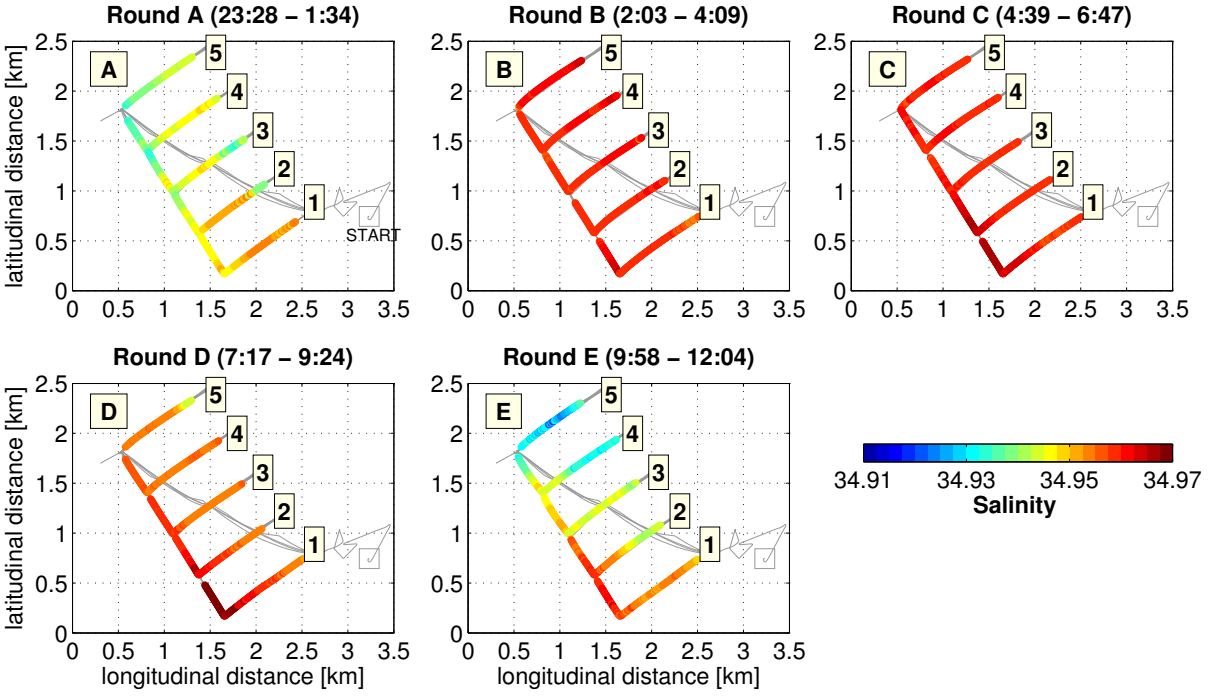

Figure 4.9: Salinity during AUV dive 7. (See caption of Fig. 4.8 for explanation.)

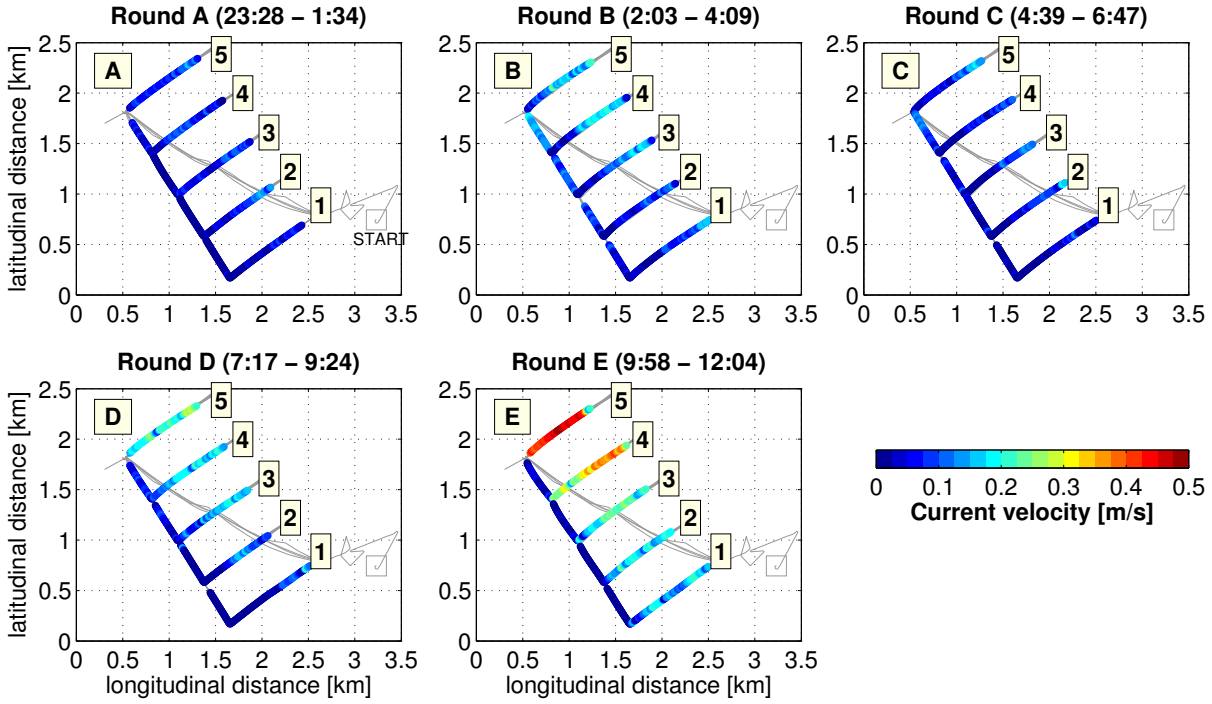

Figure 4.10: Current velocity calculated from the AUV during dive 7. (See caption of Fig. 4.8 for explanation.)

from the AUV (Fig. 4.10). During rounds A to C the AUV was likely not diving within the plume as velocities of less than 0.2 $\frac{m}{s}$ were observed. This supports the results implied by the hydrographic observations. In round D a change to higher velocities of 0.3 $\frac{m}{s}$ is observed at the northern-most track, i.e. track 5. The strongest velocities of 0.5 $\frac{m}{s}$ are found at track 5 in round E and can be linked to fresh and cold conditions (see above).

The hydrographic properties observed during AUV dive 7 indicate that a horizontal pattern can serve to analyze changes of properties in time. The spatial resolution is sufficient because changes are consistent between the tracks. In addition the changes observed between the rounds are consistent which indicates a sufficient time resolution. Spatial as well as temporal variability can be observed by using this method of mapping.

4.4 A long AUV profile in the interfacial layer between the DSO plume and ambient water

From dive 6 as well as from dive 2 and from vertical ship-lowered CTD profiles (not shown yet), the depth of the interfacial layer between the plume and the ambient water can be approximated in the mean working area. During dive 9 the AUV was diving along the 1460 m isobath heading NE at a constant depth level 91 m above the seafloor (map in Fig. 2.3). The AUV followed its programmed track diving upstream over 17 km about 5

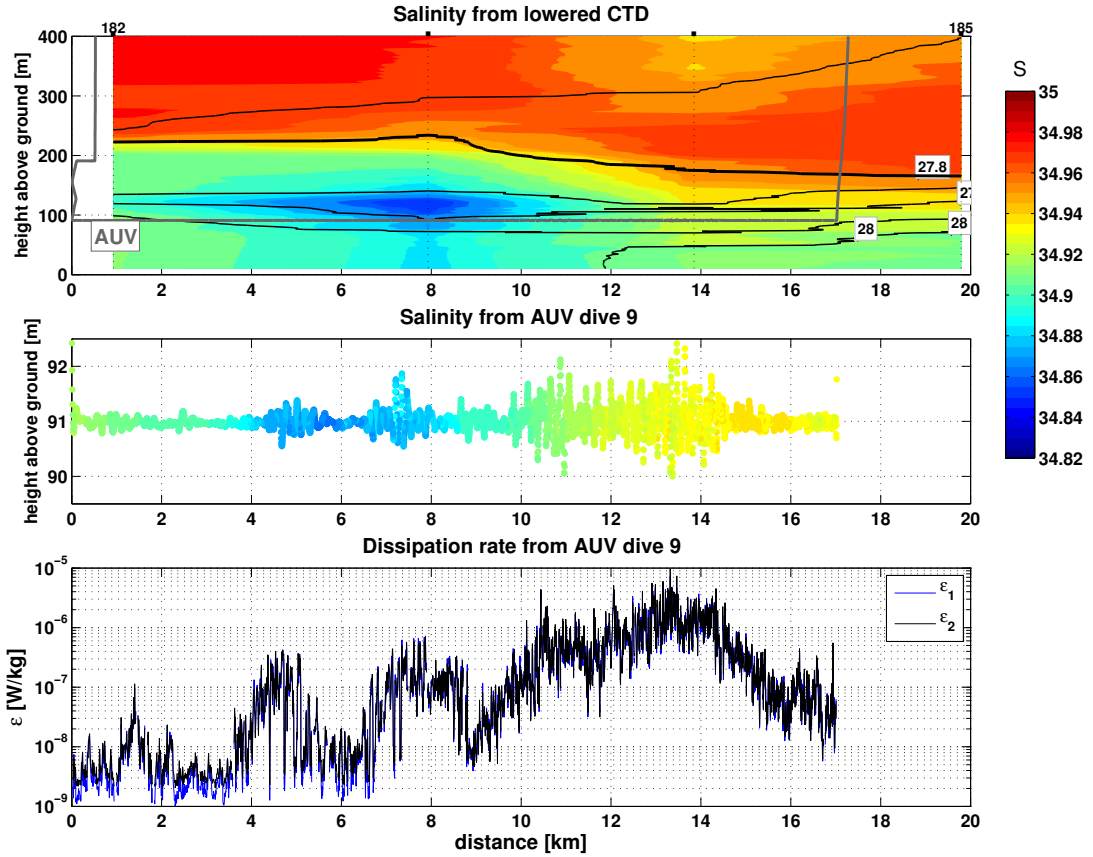

Figure 4.11: The top panel shows the salinity section interpolated from four ship lowered CTD stations (182 - 185) ranging from the seafloor up to 400 m. These CTD stations were carried out simultaneously to AUV dive 9. The grey line shows the AUV depth compared to the CTD section. The middle panel illustrates horizontally profiled salinity data collected by the AUV. The same color bar is used for both hydrographic data sets. The lowest panel shows the dissipation rates from the MSP during dive 9. In the upper two panels, all data is related in the vertical axes to the seafloor. In all panels the horizontal axes show the distance of the AUV to the southeastern-most point of the deep track.

hours to capture events of small-scale variability in the interfacial layer.

In order to provide a vertical context to the AUV-based salinity data along dive 9, data from the lowered CTD section along the AUV track can be used (Fig. 4.11, upper two panels). The CTD section obtained by linear interpolation between four lowered CTD profiles was collected during the AUV mission. It illustrates the main hydrographic properties along the AUV track. The shift in hydrographic characteristics captured in the plume and the interfacial layer by lowered CTD profiles can be analyzed with high horizontal resolution by the AUV-based measurements at one depth level. For example at CTD station 183 a low salinity anomaly is observed ranging from about 90 to 130 m above the ground (see Fig. 4.11, upper panel). The AUV captured parts of this anomaly within kilometer 4 to 8 from its starting point.

In general the AUV captures four different phases (Fig. 4.11, middle and lower panel). The first extends from the starting point to kilometer 4. Here constant salinities of 34.9 and low dissipation rates of $O(10^{-9})\frac{W}{kg}$ are observed. The second phase between kilometers 4 and 8, shows fresher water with S $\sim$ 34.86. It includes two parts from kilometers (4 - 5) and kilometers (7 - 8) with elevated ϵ-values of $O(10^{-7})\frac{W}{kg}$. Afterwards, between kilometers 8 and 14.5 (phase 3), the salinity increases from 34.87 to 34.94. Here, between kilometers 10 to 14, the highest dissipation rates of $O(10^{-7})\frac{W}{kg}$ to $O(10^{-6})\frac{W}{kg}$ are observed. In the last phase ϵ decreases down to values of the order $O(10^{-8})\frac{W}{kg}$ after kilometer 14.5 until the end of the dive. Here the salinity first stays constant at 34.94 and freshens slightly to 34.92 from kilometer 6 to 17.

In general the highest dissipation rates were observed during changes in salinity. The LADCP profiles as well as the current velocities from the AUV provide additional information about plume velocities. These will be discussed in more detail in chapter 6. It can already be seen from the salinity data and dissipation rates that the AUV covered hydrographic changes in the plume. This can be linked to small-scale turbulence implied by high dissipation rates. Although the data gained by a long horizontal profile were limited to one depth level, the vertical information can be provided by lowered CTD profiles. The advantage of diving at one depth level over a long time is that one is most likely able to capture turbulent events associated with entrainment of ambient water into the DSO plume.

4.5 Discussion

Consistency and limitation of the AUV-based measurements

The measurement system of a CTD and a MSP attached to an AUV yields new potentials of data sampling along horizontal profiles which can be used to study oceanographic topics. A general limitation of AUV-based horizontal measurements is the leakage of vertical information. Most often changes in the vertical profile are of interest because the ocean is vertically stratified. Such information can be e.g. provided by ship-lowered CTD profiles. Here the information in the horizontal profile is limited due the distance between the CTD stations. In variable systems, such as the DSO plume, the changes in the horizontal profile can be of interest. The AUV measurement system provides additional information to the vertical plume structure gained from lowered CTD profiles. This data can be used to study small-scale variability in and close above the plume in regard to entrainment by diapycnal mixing processes.

The AUV collected water mass characteristics and dissipation rates which can be used to study variability in the DSO plume during the AUV missions carried out at MSM21/1b.

In general the AUV-based hydrographic data are consistent with the lowered CTD data (Fig. 4.2) and capture the DSO plume characteristics ($\sigma_\Theta > 27.8\ \frac{kg}{m^3}$). The hydrographic data sampled along horizontal tracks at different depth levels during AUV dive 6 show that the AUV tracks covered the DSO plume and the overlying ambient water (Figs. 4.3, 4.4)

The observed dissipation rates range between a background noise of $O(10^{-9})\frac{W}{kg}$ and maximum values of $O(10^{-6})\frac{W}{kg}$ (Fig. 4.5). Such a noise level is sufficient for analyses in the turbulent regime. In general the data from the MSP indicate that dissipation rates in the DSOW plume are about one to three orders of magnitude larger than in the ambient water (Fig. 4.5). These dissipation rates are consistent with observations by the free-falling MSP deployed with some ship-lowered CTD profiles during the cruise MSM21/1b (see *Paka et al.* (2013)).

The different AUV measurement modes

The different shown measurement modes indicate that some programmed modes reveal more information in regard to DSO plume analysis than others. To analyze the the data it should be kept in mind that it is difficult to distinguish between whether properties change in time rather than in space. A stationary system is implicitly assumed for plotting maps from several AUV tracks.

The plume conditions as well as small-scale changes within different plume layers can be studied from AUV dive 6 (chapter 4.2). The additional information from the MSP and velocities may serve to explain hydrographic changes. Within dive 6 consistent hydrographic changes in time were observed (Table 4.1, round A and B). During round A the plume velocity was higher. In addition high dissipation rates were observed in the interfacial layer which can be linked to hydrographic variability (Table 4.2, track 3). In round B the mixed plume was fresher and its velocity was slightly lower (Table 4.1). In the interfacial layer the hydrographic properties showed low deviations from the mean and the dissipation rates showed values similar to the background values. This way of mapping the plume succeeded. Variability on time scales of 5 hours was captured by repeating the same pattern. Small-scale variability can be studied in the interfacial layer between the mixed plume and ambient water and can serve to analyze the diapycnal part of entrainment.

The horizontal mapping of the interfacial layer of the DSO plume in dive 5 failed (chapter 4.1). It turned out that it is better to repeat the AUV tracks at one depth level along-stream the plume. The backward tracks at higher levels should be excluded from the mapping pattern which is aimed to be studied. Dive 7 showed consistent changes in space (as it captured five tracks next to each other) and time (by repeating the same

spatial pattern five times). The disadvantage of this mode of mapping is that the vertical information is missing. During rounds A to C the horizontal mapping at 100 m above the seafloor most likely captured ambient water and not the interfacial layer. The hydrographic changes in round D and E to colder and fresher water can be linked to an increase in velocities, which are probably linked to an increase in the DSO plume height. Nevertheless, the hydrographic properties observed during round E of dive 7 can be interpreted in different ways (see Fig. 4.8 and 4.8, E). Either cold and fresh water is intruding the area at the northern part only, or it is intruding in the whole measurement domain, but was only captured during the last tracks. In addition it remains open if the water is intruding from below due to a thickening of the DSO plume or from the side with e.g. an eddy. The use of additional vertical information from lowered CTD stations is needed to interpret the observed changes.

The long profile of AUV dive 9 carried out 91 m above the seafloor provides the opportunity to capture turbulent events in the interfacial layer (chapter 4.1). Missing vertical information can be gained from lowered CTD profiles. Thus additional information supports that during dive 9, the AUV measured in the interfacial layer. The observed hydrographic changes along the AUV profile can be analyzed regarding small-scale variability. The high dissipation rates indicate that diapycnal mixing and thus an entrainment event was probably captured. Dive 9 provides useful information regarding variability in the interfacial layer of the plume which will be discussed in detail in the following two chapters.

4.6 Summary

The AUV-based hydrographic data is consistent with lowered CTD data. Three different modes of mapping the DSO plume with the horizontal profiling AUV were tested. Assuming steady-state dive 6 provides information about the vertical plume structure. Here, small-scale variability within each plume layer can be studied based on several horizontal tracks taken at different depth levels. During dives 5 and 7 several parallel-running tracks at constant depth levels were carried out to map the DSO plume in a horizontal plane. By repeating the same pattern variations in time and/or space can be observed. The missing vertical information leads to problems when performing analyses in a physical context. The third example represents a long AUV dive which was programmed to follow one contour line at constant depth. The data shown captured several events of variations in hydrographic properties on small horizontal scales. These events will be analyzed in detail in the following chapters. This mode, in combination with vertical information from lowered CTD stations, gives the best results to allow analysis of small-scale turbulence in

the interfacial layer of the DSO plume.

The dissipation rates of the MSP are in the same range of dissipation rates observed by the vertical profiling free-falling MSP. Varying dissipation rates in the interfacial layer as well as in the speed of the plume can be used in combination with the hydrographic variability to study entrainment by vertical mixing in the interfacial layer between the DSO plume and ambient water.

Chapter 5

Small-scale turbulence studied by AUV-based observations

The AUV missions aimed to study small-scale variability at the interface between the DSO plume and the ambient water. In this chapter AUV data with signatures of high fluctuations in hydrographic properties are analyzed and compared to the turbulent dissipation rates observed by the AUV-based MS measurements. The scales of variability are studied by spectral and wavelet analyses. Finally the energy from temperature data of the CTD is compared to the dissipation rates obtained by the MSP based on horizontal wave number spectra.

5.1 Hydrographic variability observed during the AUV missions

5.1.1 Hydrographic data of AUV dive 2

The AUV dive 2 was programmed to repeat one track along the same contour line at six different depth levels (map in Fig. 2.3). Similar to AUV dive 6, the vertical plume structure was covered by the horizontal AUV tracks (compare to chapter 4.2). Thus dive 2 provides hydrographic data and dissipation rates in the mixed plume, the interfacial layer, and the ambient water.

The deepest track captured the coldest ($\Theta \approx 0.5$ °C) and freshest (S = 34.9) water (Fig. 5.1). In general the upper three tracks (6, 7, backward tracks) sampled about 4.2 °C warm and salty water with salinities ranging between 34.96 and 34.98. The tracks between 1300 and 1360 m depth captured the gradient from warm, salty water at the top to cold, fresh water at the bottom. This can be seen by the linear Θ-S-relation as well (Fig. 5.1, lower right panel). Varying properties occur between 100 m and 200 m above

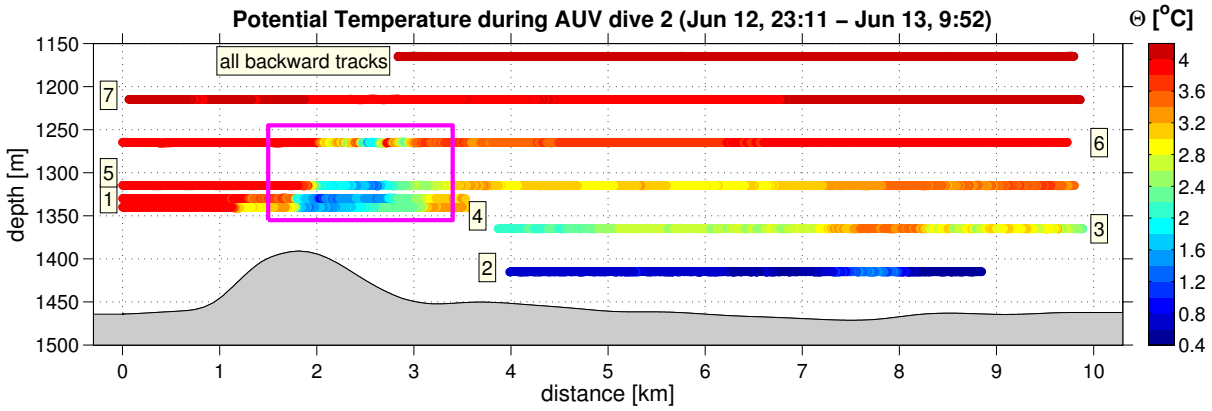

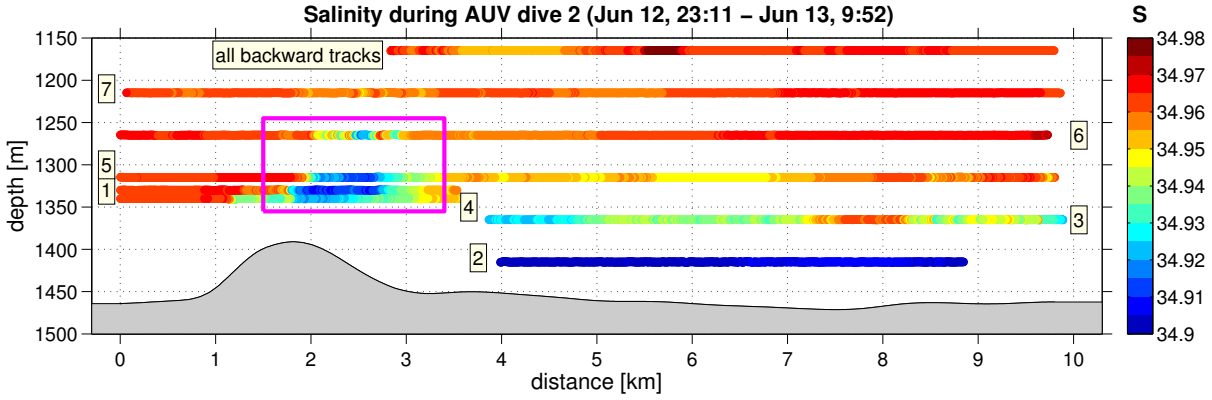

Track	start time (UTC)	end time (UTC)
1	23:11	23:44
2	23:50	1:10
3	1:13	2:18
4	2:21	2:57
5	2:58	4:46
6	4:49	6:36
7	6:39	8:24

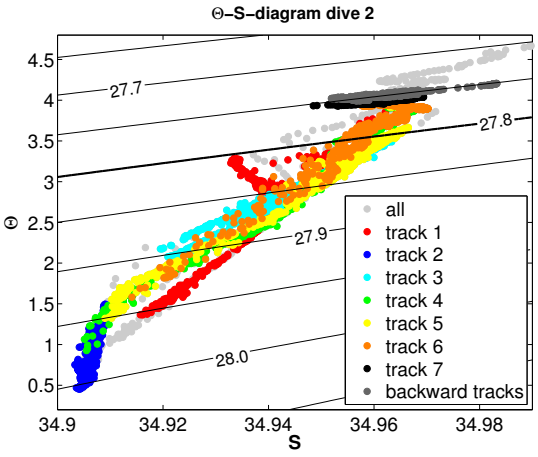

Figure 5.1: Potential temperature (top panel) and salinity (middle panel) observed during AUV dive 2 at constant depth levels above the seafloor. The starting point of each track is numbered. Grey shading marks the bottom topography. The table below shows the start and end time of each track, respectively. The lower right panel shows the Θ-S-diagram from all tracks.

the seafloor 1.5 km to 3.5 km away from the southwestern-most point (marked by the box in Fig. 5.1). Here an intrusion of fresh and cold water with Θ = (0.5 - 2) °C and S = (34.89 - 34.92) into the warm and salty surrounding water is found (see Fig. 5.1). Track 4 covered about the same depth and location as track 1 but was run about 3 hours later (Table in Fig. 5.1). Both tracks still captured the cold and fresh signal as well as

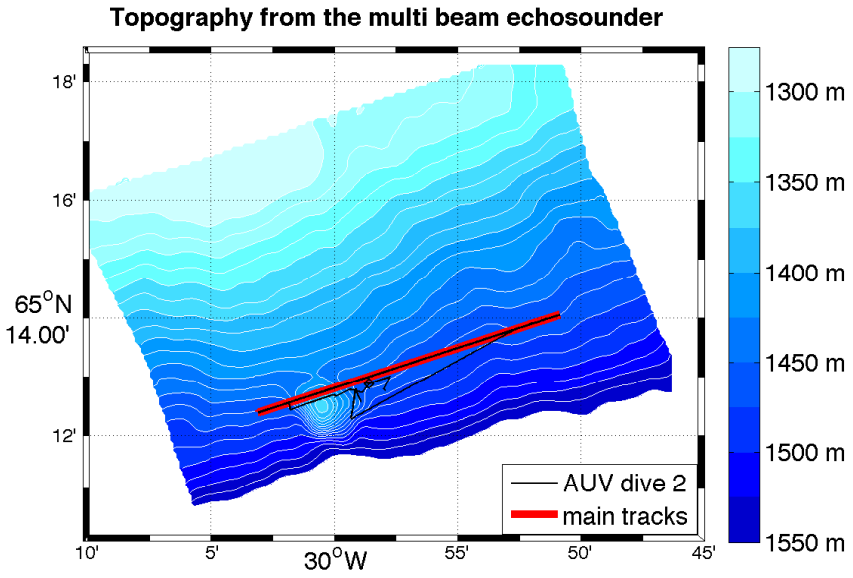

Figure 5.2: Topography from a multibeam echo sounder. White lines mark depth contours with dz = 12.5 m. The black line indicates the positions of AUV dive 2, the red line marks the track along the 1475 m isobath repeated at different depth levels during dive 2 (compare with Fig. 5.1).

track 5 and 6. This signal can be linked to the bottom topography. A high resolution map achieved from a multibeam echo sounder (Fig. 5.2) shows that the AUV is diving along the Greenland slope. At about 30°W and 65°12.5'N a topographic elevation with a height of 70 m was found. While the AUV followed the 1475 m isobath it passed the northwestern part of this topographic elevation. In regards to the DSO plume propagating from NW to SE, the plume encounters the elevation on its northwestern side and likely flows around the elevation. The local intrusion of cold and fresh water extends from the point where the bottom height increases to the highest point of the elevation (see Fig. 5.1, upper two panels). In contrast the water is homogeneous throughout all tracks behind the elevation.

5.1.2 Fluctuations in θ-S-characteristics during AUV dive 9

Hydrographic variability is also observed along the long horizontal profile of dive 9. As presented in section 4.4, dive 9 was carried out at a constant depth level of (91 $\pm$) 1 m above the seafloor. The AUV was approximately following the 1350 m contour line of the Greenland continental slope and covered a 17 km long horizontal profile above the seafloor which corresponds to 28.8 km through the water (see map in Fig. 2.3). The ship-lowered CTD Θ-S properties are in reasonable agreement with those from the AUV-based one (Fig. 5.3). All hydrographic data are contained in the DSOW water class ($> 27.8\ \frac{kg}{m^3}$) with densities between 27.87 and 27.97 $\frac{kg}{m^3}$. A wide range in Θ and S is observed rather

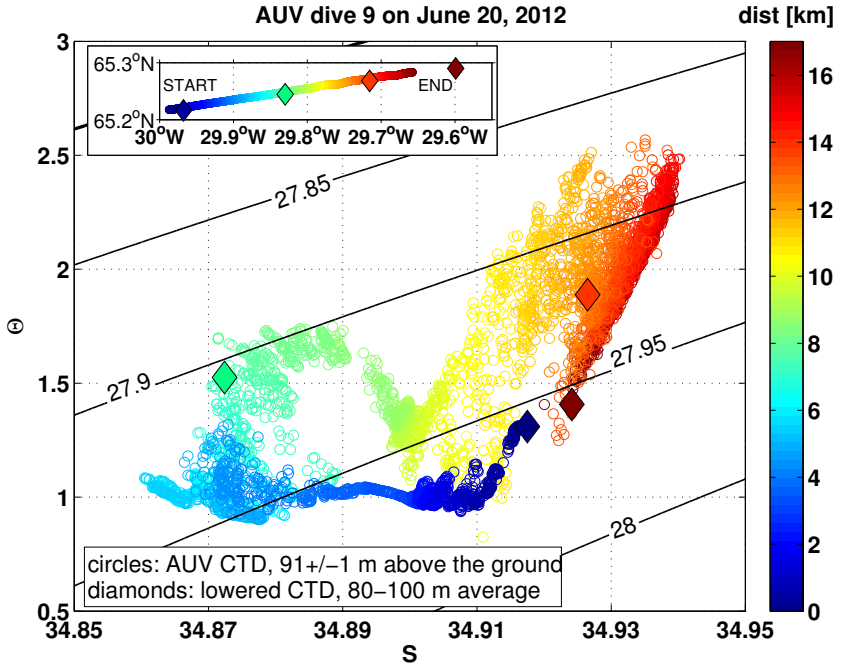

Figure 5.3: Θ-S-diagram collected during AUV dive 9. The small panel in the upper left corner illustrates the location of the AUV dive compared to the CTD stations. Colors indicate the distance of the AUV and CTD stations from the starting point of the deep AUV track in the southwest. The AUV dives along the slope heading northwest against the mean flow direction. The same color range is used in the θ-S-diagram in order to illustrate from which location the data originates. Here circles indicate data of the AUV-based CTD. Diamonds mark the average Θ-S-data taken over a depth range of 80 to 100 m from four ship-lowered CTD profiles in the depth range of the AUV.

than a linear relation relationship as in dive 2 (see Fig. 5.1). This indicates a transition between at least three different classes of water masses. In general the temperature and salinity driven density variations not equal. Within the first 2 km the AUV collects water with mean properties of Θ = 1 °C and S = 34.91 (see Fig. 5.3). Subsequently until about kilometer 8 the AUV passed through a regime of fresher and cold water with S = (34.86 - 34.88) and Θ = (0.9 - 1.6) °C. Between kilometers 8 and 12 another transition to saltier water with higher temperatures is observed. During this time the salinity increases by about 0.05. During the end of the AUV dive (> 13 km) the θ-S-characteristics mainly merge along a line extending from (Θ = 2.5 °C, S = 34.935) to (Θ = 1.5 °C, S = 34.92). This goes along with the potential density varying between 27.87 $\frac{kg}{m^3}$ and 27.95 $\frac{kg}{m^3}$ (Fig. 5.4). During the first eight kilometers a smooth transition to fresher waters is observed. The potential density decreases from 27.97 $\frac{kg}{m^3}$ down to 27.9 $\frac{kg}{m^3}$. In contrast between kilometers 10 and 14 the potential density varies between 27.85 $\frac{kg}{m^3}$ and 27.98 $\frac{kg}{m^3}$ (see Fig. 5.4). Such fluctuations are observed within horizontal scales of a few hundreds of meters. The variable heights above the seafloor of the AUV, ranging from

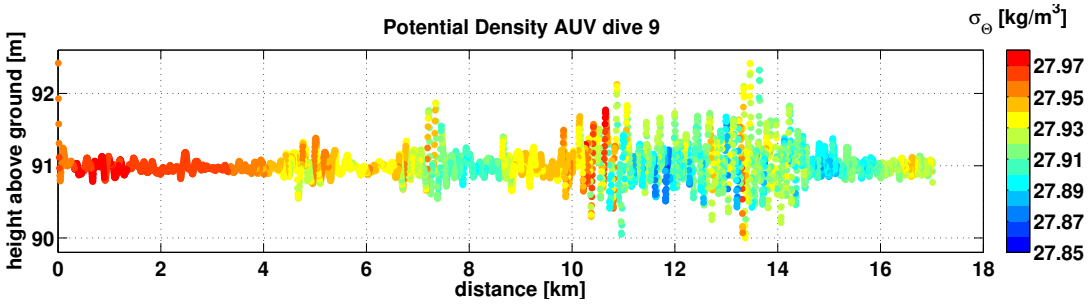

Figure 5.4: Potential density observed along the long horizontal track of AUV dive 9.

around 90 m to 92.5 m, indicate that the AUV experiences vertical water movements, possibly related to turbulence (see chapter 5.5).

Dive 9 shows that salinity and temperature can drive changes in density variations independent of each other. These variations as well as the horizontal displacements of the vehicle indicate that the AUV was diving through turbulent regimes.

5.2 Dissipation rates observed during the AUV missions

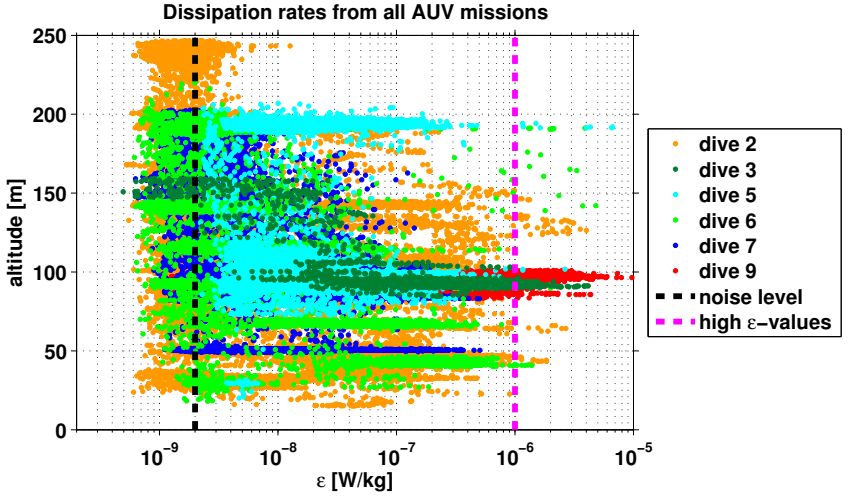

Figure 5.5: Dissipation rates from all successful AUV missions in the main working area (see map in Fig. 2.3) as a function of height above the seafloor. For simplicity the data from both shear probes are presented with exception for dive 5 and 6 (see section 2.2.3). The dashed black line marks the chosen noise level of $(2 \cdot 10^{-9})\frac{W}{kg}$. The dashed magenta line indicates very high dissipation rates of $(10^{-6})\frac{W}{kg}$.

The MSP was attached to the AUV in order to estimate the rate of dissipation of TKE. High dissipation rates can be associated with a high mixing efficiency. Thus entrainment

by diapycnal mixing can be studied by diving in the interfacial layer above the mixed DSO plume (see chapters 1 and 3).

In general the range of ϵ extends from about $(3 \cdot 10^{-10})\frac{W}{kg}$ up to $(10^{-5})\frac{W}{kg}$ in comparison of the dissipation rates from all AUV missions (Fig. 5.5). At the lower boundary a noise level of $2 \cdot 10^{-9}\frac{W}{kg}$ is chosen (Fig. 5.5, grey line). It is assumed that ϵ below this value cannot be resolved. Dissipation rates exceeding $10^{-6}\frac{W}{kg}$ are observed during AUV dives 3, 5 and 6, but most often during dives 2 and 9 (see Fig. 5.5), where hydrographic variability was observed to be high (see above). Thus, dissipation rates are studied in detail for dives 2 and 9 in the following.

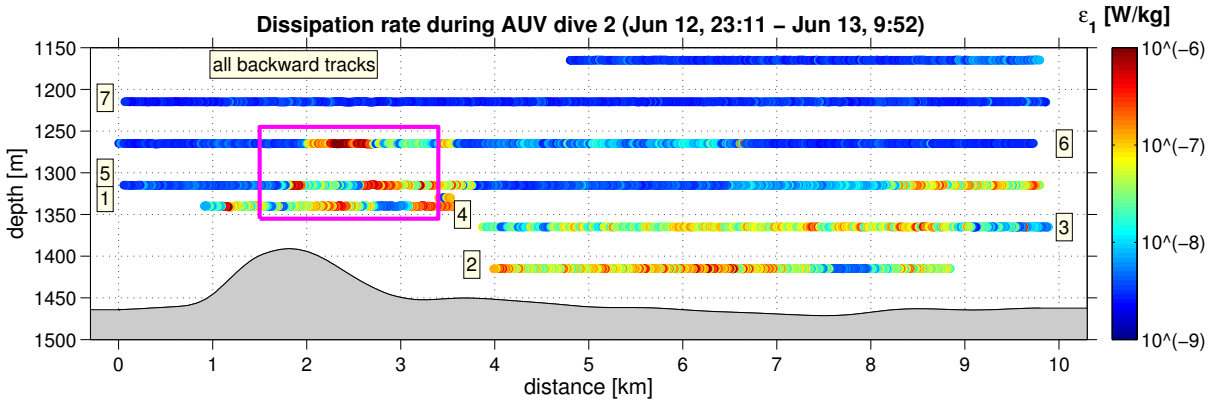

Figure 5.6: Dissipation rates observed along all tracks of AUV dive 2. (See caption of Fig. 5.1 for explanation.)

During dive 2 the highest mean values of $\epsilon_{mean} = (10^{-7})\frac{W}{kg}$ are observed for tracks 1 and 2 (see Fig. 5.6). Further away from the seafloor ϵ is one order of magnitude smaller ($\epsilon_{mean} = (5 \cdot 10^{-8})\frac{W}{kg}$ for tracks 3, 5, and 6). Above 1250 m (track 7 and backward tracks) the dissipation rates are in the range of background noise. The dissipation rates in the vicinity of the abyssal hill (see Fig. 5.6, pink box) vary from $O(10^{-9})\frac{W}{kg}$ to $O(10^{-6})\frac{W}{kg}$. Patches with high dissipation rates of $O(10^{-6})\frac{W}{kg}$ over a horizontal scale of 200 m are observed here. The elevated dissipation rates are observed in the same location where the cold and fresh water intruded into the ambient water (see Fig. 5.1, upper and middle panel, pink box). These observations can most likely be linked to the topographic elevation and are discussed with regard to vertical information from CTD stations in chapter 6.

During AUV dive 9 high dissipation rates of $O(10^{-6})\frac{W}{kg}$ are observed over an even broader horizontal range of about 4 km (Fig. 5.7). Between kilometers 10.5 and 14.5 dissipation rates reaches values of $O(10^{-6})\frac{W}{kg}$. In contrast, in the beginning of the track, from kilometer 0 to 4, ϵ values are about three orders of magnitude smaller and in the range of the background noise ($(2 \cdot 10^{-9})\frac{W}{kg}$). Dissipation rates of $O(10^{-6})\frac{W}{kg}$ are observed in combination with high density variations induced by temperature fluctuations (Figs. 5.3, 5.4). Additionally an increase in the current velocities is observed. These observations

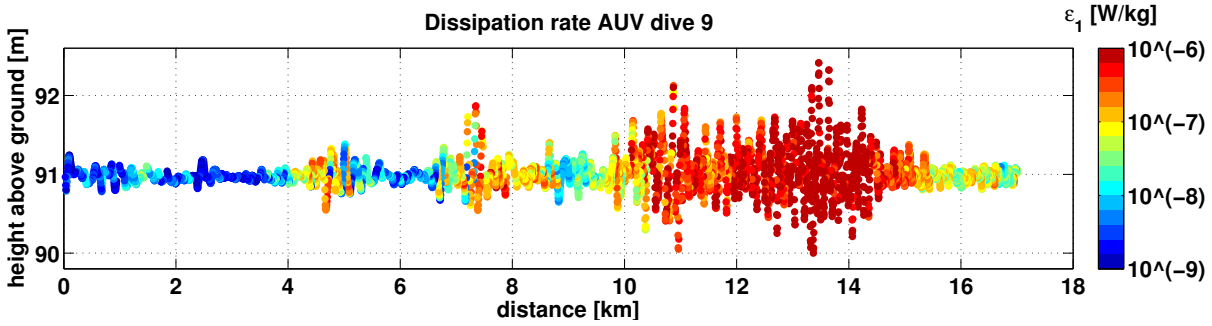

Figure 5.7: Dissipation rates observed along the track of AUV dive 9. (See caption of Fig. 5.4 for explanation.)

are studied with regard to the DSO plume dynamics in chapter 6.

5.3 Time and length scales of hydrographic variability

Based on the above described analyses, the horizontal tracks of AUV dives 2 and 9 were chosen to investigate the hydrographic variability on small-scales by spectral analysis.

5.3.1 Analyses of spectral subranges based on AUV-temperature data

In the following, the temperature time series of AUV dive 9 is used to evaluate scales of variability in comparison to the universal spectra found in the ocean (see chapter 3.2). The time series was transferred into wavelength by using the mean velocity of the AUV through the water (1.6 $\frac{m}{s}$) according to the Taylor hypothesis.

The spectral slope of the wave number spectrum of temperature is parallel to $k^{-5/3}$ in the range of 0.01 cpm to 0.3 cpm (Fig. 5.8). This is expected in the inertial-convective subrange (see chapter 3.2, Table 3.1). The wave number range corresponds to time periods of about 10 s to 6.7 min and length scales of 16 m to about 650 m. The slope of the spectrum increases at the highest wave numbers (see Fig. 5.8). In this range, the spectrum clearly does not correspond to the equilibrium spectrum for the inertial-diffusive subrange ($\Phi_T^{ID} \sim k^{-1}$). The drop off in energy at high wave numbers is likely caused by filter effects and/or limits of the measurement system as discussed below (section 5.5).

For comparison the temperature spectrum is transformed into an isothermal slope spectrum (see chapter 3, equation 3.16). The background temperature gradient is estimated from the ship-lowered CTD profiles carried out during AUV dive 9 in the depth range of the AUV track. Here a mean background temperature gradient of $\frac{d\Theta_0}{dz} = \frac{2.17}{100}\frac{°C}{m}$ is

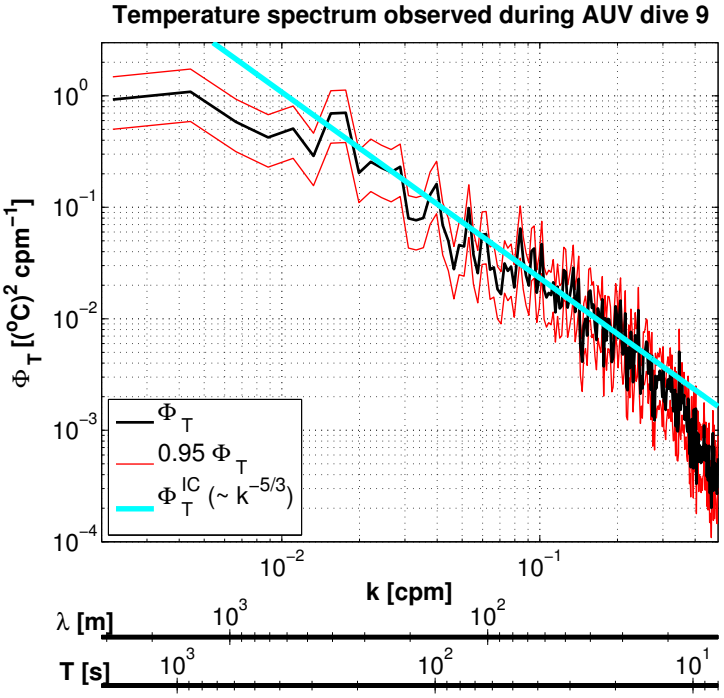

Figure 5.8: Temperature spectrum (Φ_T) of AUV dive 9 using 30 min long data segments with an overlap of 50% (black line). Red lines give the 95% confidence intervals. The light blue line has a slope of $k^{-5/3}$ (inertial-convective subrange).

applied to the temperature spectrum. The isotherm slope spectrum (Fig. 5.9, black line) is parallel to $k^{1/3}$ (Fig. 5.9, blue line) between 0.01 and 0.3 cpm, which is expected by the universal spectrum of the inertial-convective subrange. At highest wave numbers the slope of the spectrum is negative and thus clearly does not correspond to the equilibrium spectrum for the inertial-diffusive subrange ($\Phi^{ID}_{d\zeta/dx} \sim k^1$). This spectrum was calculated based on processed data filtered with a cutoff frequency of 8 s (see section 2.2.3). For comparison an isotherm slope spectrum calculated from unfiltered temperature data is given (Fig. 5.9, grey line). The energy from the unfiltered data (grey line) falls off slightly at wave numbers larger 0.23 cpm and rapidly at wave numbers larger than 2 cpm. The drop-off in the processed data (Fig. 5.9, black line) at k = 0.37 cpm is not seen in the unfiltered data. Thus the spectra of the processed time series are contained by the low-pass filter at k > 0.37 cpm (see section 2.2.3). Based on this, the upper limit of the wave number spectra is chosen at k = 0.37 cpm (Fig. 5.9, magenta line) for all further spectral analysis of the processed data. The limit at 0.37 cpm ($\lambda = 17m$) is either marked by the pink line or used as the upper range of the wave number axis in subsequent Figures.

In addition, the sensitivity of the isothermal slope spectrum to the background temperature gradient is tested. The ship-lowered CTD profiles show rather variable conditions at the depth level of the AUV during dive 9 (see below). Choosing a slightly smaller temperature background gradient of $\frac{d\Theta_0}{dz} = \frac{1.71°C}{100m}$[1], shifts the spectrum to energy levels matching the upper 95 % confidence interval (see Fig. 5.9, green and red line).

[1]The temperature gradient corresponds to the mean minus the standard deviation of temperature gradients computed from CTD profiles (details see below in section 5.4)

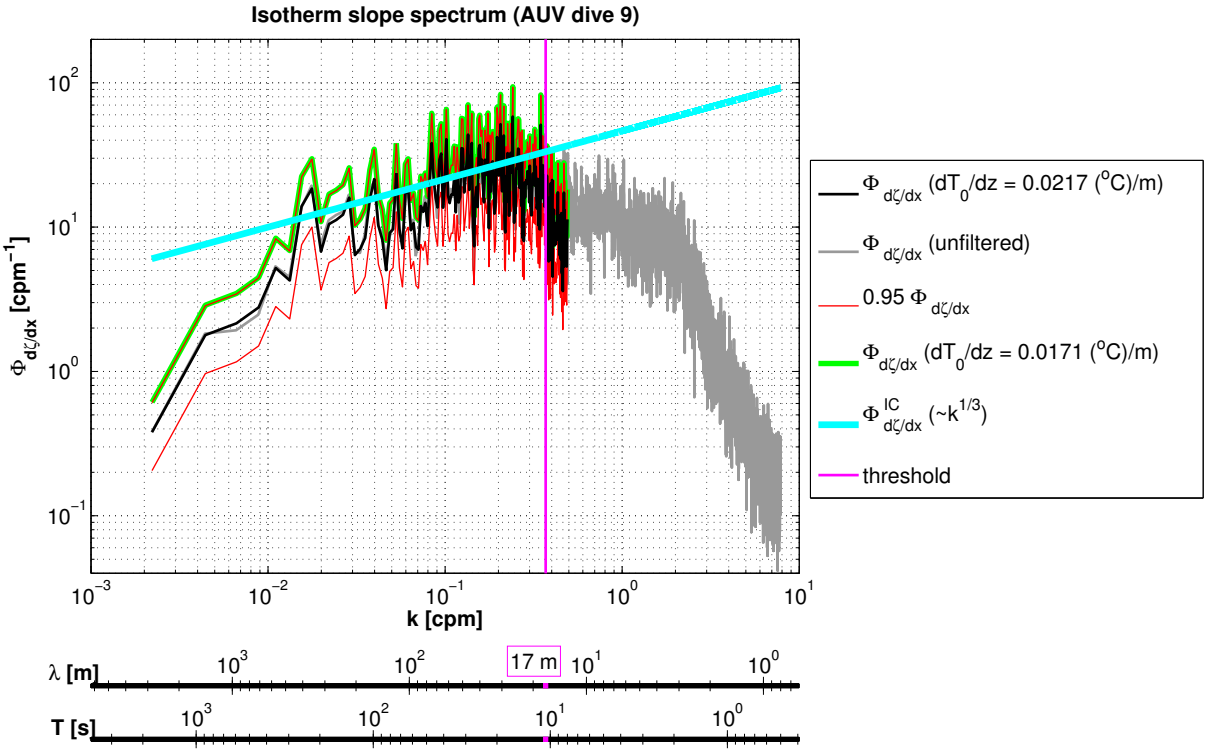

Figure 5.9: Isotherm slope spectrum ($\Phi_{d\zeta/dx}$) transformed from the temperature variance spectrum of AUV dive 9 with a background temperature gradient of $\frac{dT_0}{dz} = 0.0217 \frac{^\circ C}{m}$ (back line). The red lines are the 95 % confidence intervals. The grey spectrum is calculated in the same way from unfiltered temperature data. The green line shows the spectrum using a smaller background temperature gradient of 0.0171 $\frac{^\circ C}{m}$. The light blue line has a slope of $k^{1/3}$ (inertial-convective subrange). The magenta line marks the upper limit of the spectrum accounting for filter effects.

Although the AUV is programmed to dive at a constant depth level, small deviations in the pressure values were observed (see Fig. 5.4). The up- and downward motion of the vehicle may have caused temperature fluctuations not related to isothermal displacements. In order to study the contamination of the vertical motion of the AUV on the temperature and slope spectra, the gradient depth spectrum was calculated from the pressure data of the AUV. The depth spectrum describes the vertical AUV displacement. It was multiplied by $(2\pi k)^2$ to achieve a gradient spectrum which is comparable to the isothermal slope spectrum. Figure 5.10 shows the isothermal slope spectrum compared to the gradient spectrum of the vertical AUV motion computed from the deep track of AUV dive 9. The displacement spectrum is one order of magnitude larger than the spectrum of vertical motion of the AUV at wave numbers larger 0.03 cpm. The energy drops off rapidly for values of $O(10^{-6})\frac{W}{kg}$ at wave numbers larger than 0.6 cpm. As the gradient depth spectrum shows considerably lower energy over the entire wave number range it is concluded that the contamination of the temperature fluctuations by vertical movements of the AUV are

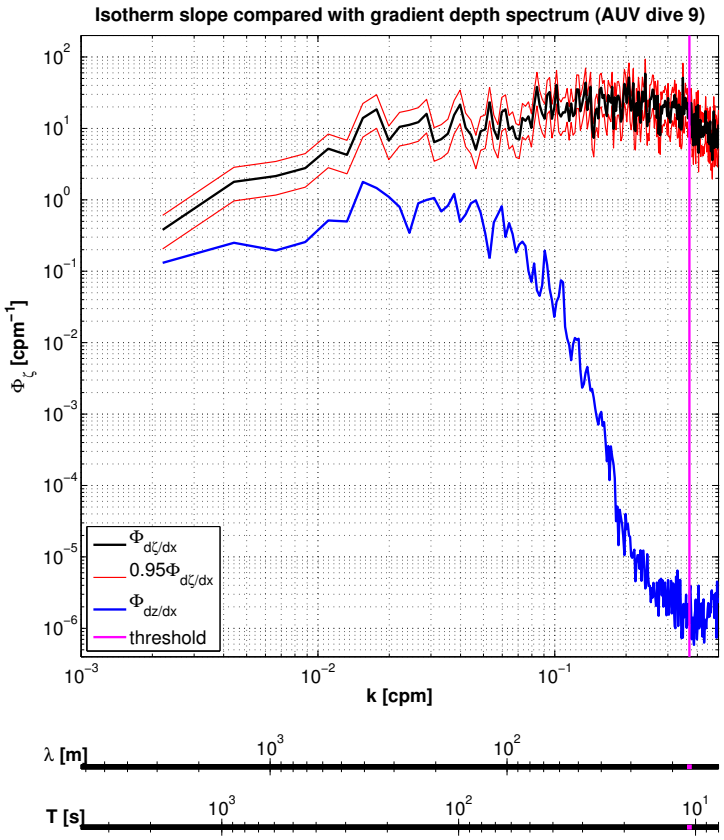

Figure 5.10: Isotherm slope spectrum ($\Phi_{d\zeta/dx}$) with 95% confidence intervals as in Fig. 5.9 (black and red lines). The isotherm slope spectrum is compared to the gradient depth spectrum ($\Phi_{dz/dx}$) from the pressure data of the AUV (blue line).

negligible in the turbulent subrange.

5.3.2 Wavelet transform for AUV-based T and S time series

The spectral analysis of the hydrographic data collected during AUV dive 9 has shown how energy is distributed on turbulent time and length scales. Wavelet analysis yields a closer insight not only by showing the distribution of the energy as a function of frequency, but also by showing the frequency (wave number) distribution of energy as a function of time (space). The largest temperature variances of the order of $10^{-3}\frac{(^\circ C)^2}{s}$ are observed during AUV dive 9 on June 20, between 12:30 and 14:00 (Fig. 5.11, for comparison: between kilometers 10 and 14.5). The magnitude is 3 orders of magnitude higher than the background variance found e.g., during the first hour of the AUV cast (see Fig. 5.11). The energy is dominantly found on time scales of 5 minutes down to the smallest scales of 8 s. This corresponds to length scales of around 500 m to 13 m. The energy is found to be two to three orders of magnitude smaller on timescales between 10 min to 1 hr. Between 11:00 and 12:15 variances of $O(10^{-4})\frac{(^\circ C)^2}{s}$ are found at time scales of (2 - 5) min and last

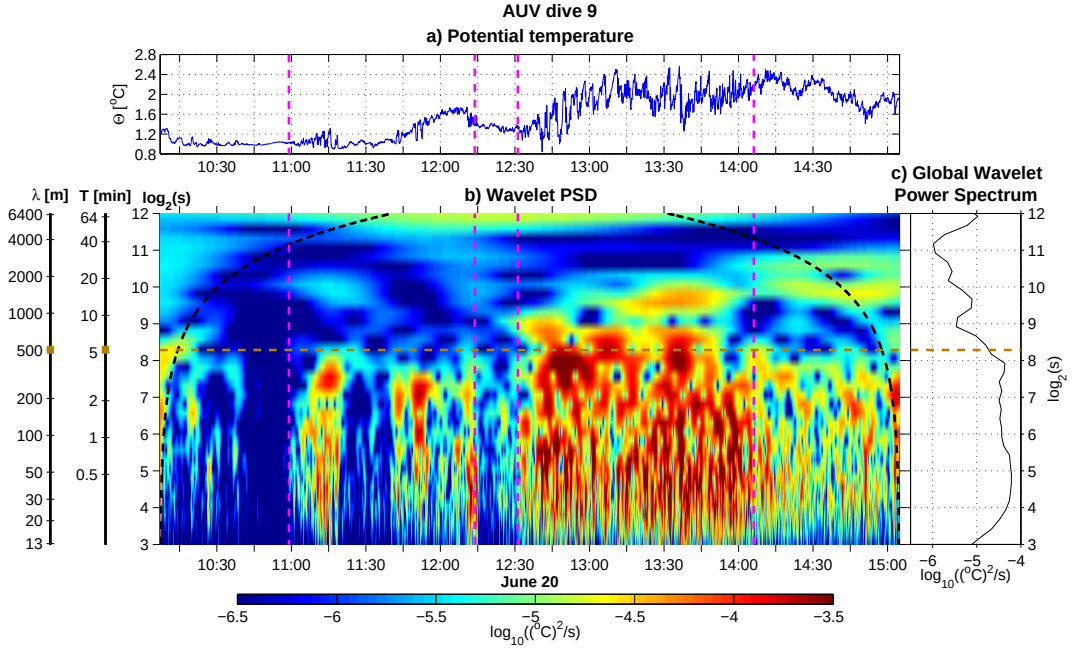

Figure 5.11: Wavelet transform of the time series of Θ collected during AUV dive 9 at constant depth (90 m above the ground). The upper panel (a) shows the time series of Θ used for the wavelet transform. Panel (b) gives the wavelet power spectral density. On the left, the two additional axes give the corresponding wavelength in meters and periods in minutes (based on the Taylor hypothesis). Panel (c) shows the corresponding global wavelet power spectrum, which gives the sum of the PSD over time. The magenta dashed lines in panels (a) and (b) mark two segments (11:00 - 12:15; 12:30 - 14:05). The brown dashed line in panels (b) and (c) indicates time periods of 5 min. The black line indicates the cone-of-influence (*Torrence and Compo*, 1998).

for about 10 minutes at 11:10 and 11:45. The global wavelet power spectrum (right panel Fig. 5.11) shows that most energy during the whole AUV track is observed on time scales of less than 5 min.

The wavelet PSD of salinity shows background values of $O(10^{-9})\frac{1}{s}$ (Fig. 5.12). Within the first time window, from 11:00 to 12:15 large variances of $O(10^{-6})\frac{1}{s}$ are observed between 11:40 and 12:00 at time scales of 2 to 4 min. During the second marked time window between 12:30 and 14:07 no dominant signals in variances were observed. The global wavelet power spectrum (right panel Fig. 5.11) shows a peak on time scales of about 2 min.

Both wavelet spectra show similarities in the first time window from 11:00 to 12:15, in comparison. Potential temperature as well as salinity drive density variations (compare to Fig. 5.3) on small scales here. In the second time window from 12:30 to 14:05 high

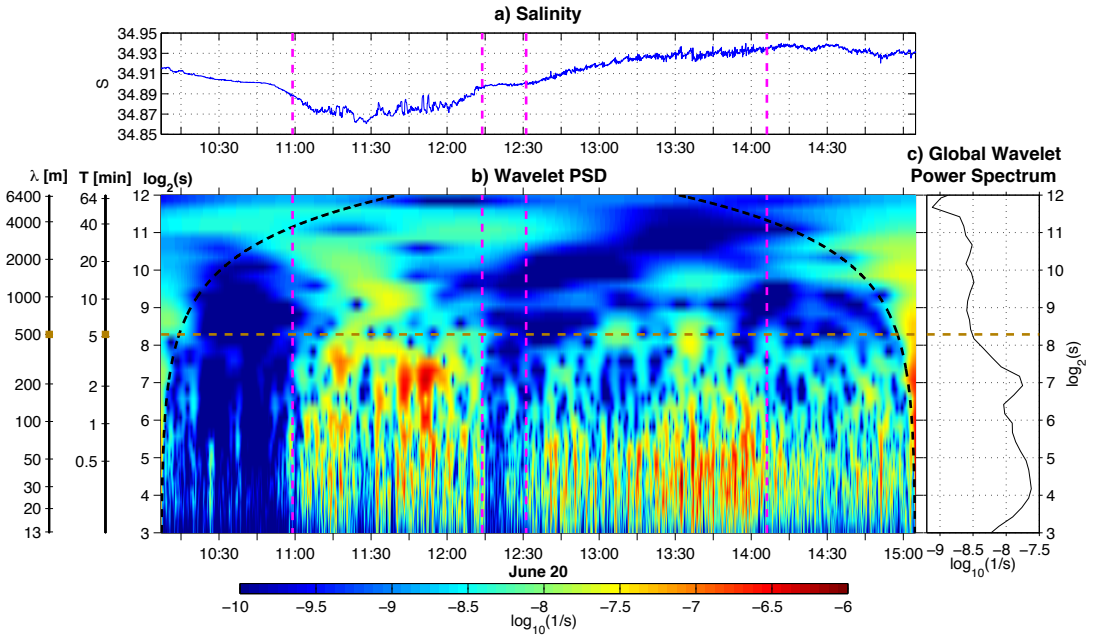

Figure 5.12: Salinity time series (a), wavelet PSD of salinity (b), and global wavelet PS of salinity (c) computed from AUV dive 9. (See caption of Fig. 5.11 for explanation.)

variances in the temperature but not in salinity are found. Thus temperature drives density variations on length scales of 13 m to 500 m.

5.4 Relationship between turbulent dissipation rates and the variances of isothermal displacements

Direct methods to estimate turbulent dissipation rates are based on either the use of shear probes or fast thermistors (see chapter 3). Recently *Klymak and Moum* (2007a) suggested that turbulent dissipation rates can be estimated from isopycnal slope spectra even from instruments that can resolve scales larger than a few meters. Thus the measurement system of the AUV provides the instrumentation to estimate turbulent dissipation rates from a temperature spectra of horizontal CTD measurements following *Klymak and Moum* (2007a).

Dissipation rates can be estimated by fitting the isotherm slope spectrum to the universal spectrum for the inertial-convective subrange (eqn. 3.16). However there are two major difficulties. Firstly, the measurements were carried out in the mixed bottom plume, the gradient interfacial layer, and the ambient water. Thus, in order to transform temperature to isotherm slope spectra, there is a need to estimate local temperature gradients for each of the chosen AUV tracks instead of simply one background temperature gradient. Secondly, the spectrum depends on χ_ζ and thus on the vertical temperature gradients

and buoyancy frequencies. Due to the highly variable background conditions it is not the aim of this study to estimate the turbulent dissipation rate directly by fitting the spectra. Nevertheless it is shown below that a direct dependence of the variances of isotherm displacement to the dissipation rates (estimated from the MSP) exists.

The following procedure is used to relate the spectra to dissipation. For the two datasets of AUV dives 2 and 9 several segments of the dives are chosen to compare conditions of low and high temperature fluctuations. In the following, only the results of AUV dive 9 are presented. The same steps were applied to AUV dive 2.

The temperature time series collected during dive 9 was divided into six segments (A - F, see top panel in Fig. 5.14). The segments were chosen to capture temperature fluctuations with different amplitudes around the respective segment-mean temperature level. As seen above (Fig. 5.9) the isotherm slope spectrum in the turbulent wavenumber range is sensitive to the choice of the background temperature gradient. Local temperature gradients have been estimated based on the vertical temperature profiles from the ship-lowered CTD data. The results from profiles 182 to 185 carried out during AUV dive 9 are shown in Fig. 5.13. At the depth level of the AUV (about 91 m above the seafloor) the vertical temperature gradients in the lowered CTD profiles vary within a broad range (see below in Fig. 6.11). More robust estimates are achieved by calculating temperature gradients in temperature classes rather than depth classes. Subsequently, these can be applied to the segment-mean temperatures inferred by the AUV in order to convert temperature fluctuations to displacements of isotherms. For each vertical temperature profile

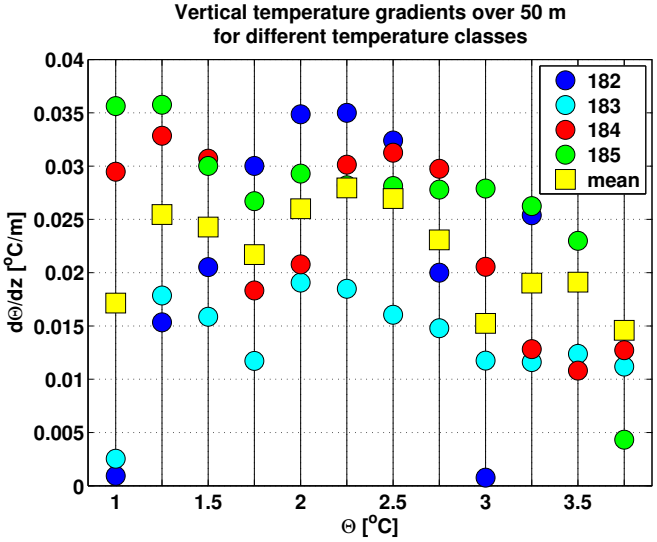

Figure 5.13: Vertical temperature gradients over 50 m sorted by different temperature levels from 1°C to 3.75 °C. Colored circles mark the values obtained from four different vertical CTD profiles (182 - 185). The yellow squares mark the mean of the gradients from all four profiles at each temperature level.

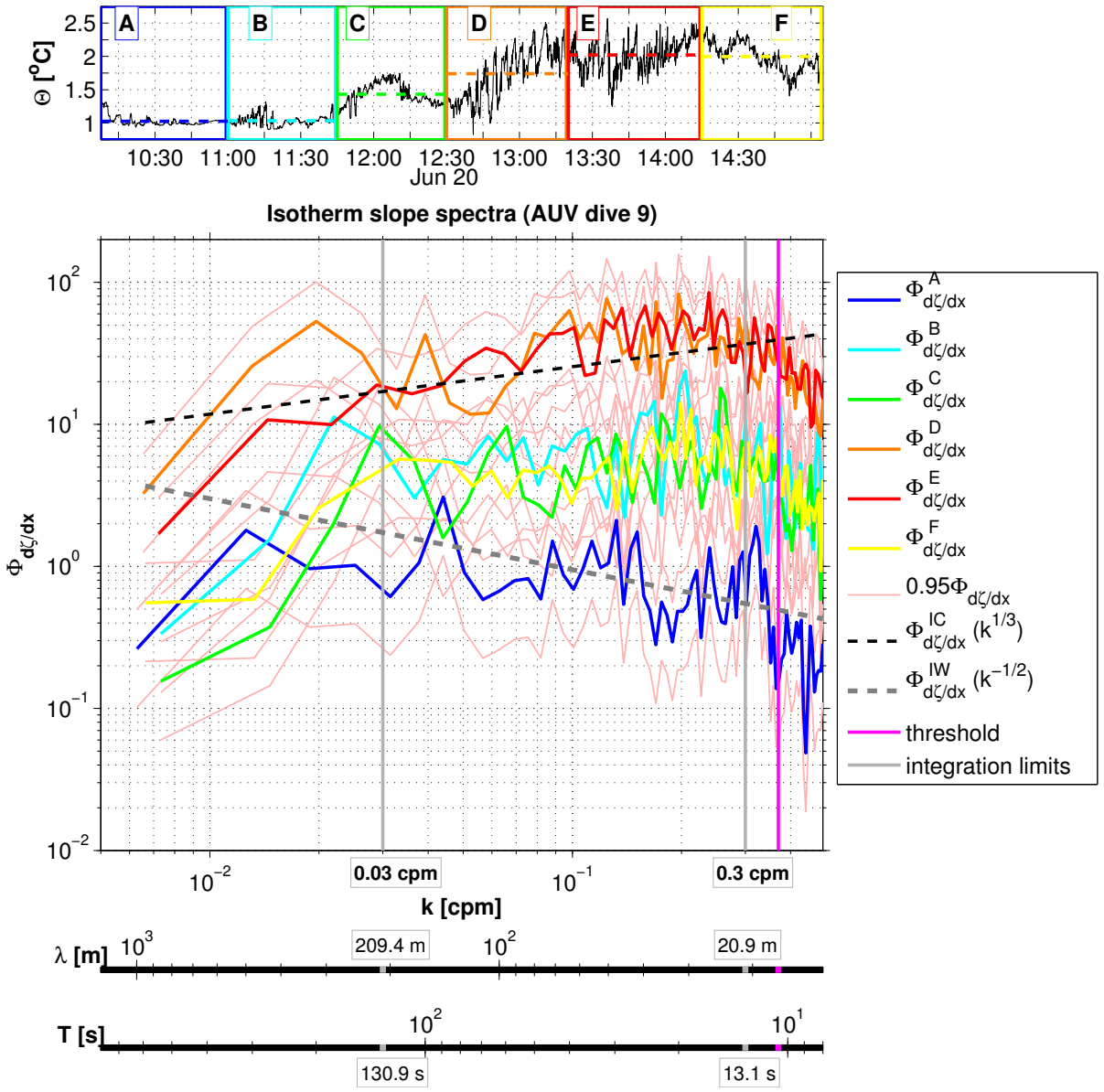

Figure 5.14: The top panel shows the temperature time series of AUV dive 9 and the chosen segments A to F. Marked in addition is the mean temperature within each segment to estimate the background temperature gradient (colored dashed lines). The lower panel shows the corresponding isotherm slope spectrum ($\Phi_{d\zeta/dx}$) of each transect and the corresponding 95 % confidence intervals (light red lines). The isotherm slope spectra were computed from temperature spectra (using 10 min long data segments and an overlap of 50 %). The black dashed line shows the expected slope ($k^{1/3}$) of the equilibrium spectrum in the inertial-convective subrange; the grey dashed black line shows the expected slope ($k^{-1/2}$) of the equilibrium spectrum in the internal wave subrange (see chapter 3, Table 3.1). The magenta line gives the threshold chosen from the comparison to unfiltered data (see Fig. 5.9). The grey lines indicate the chosen lower (0.03 cpm) and upper (0.3 cpm) limit for the inertial-convective subrange.

the temperature levels from 1 °C to 3.75 °C with dT = 0.25 °C are chosen with the upper and lower level so that near-zero-gradients in the bottom mixed layer are excluded. A linear least-square-fit was applied to all temperatures in the range of ± 25 m from the depth of a chosen temperature level by $T_{fit} = a + bz$ with $(T(z) - T_{fit})^2 = min.$ The slope b represents the mean vertical temperature gradient at certain temperature levels of a vertical CTD profile.

The slopes vary among different CTD profiles for the temperature levels near 1 °C and 3 °C (Fig. 5.13). All other values differ by a factor of two. The resulting mean over all temperature classes is 0.0217 ± 0.0046 $\frac{°C}{m}$. The mean slopes of the temperature classes were applied to the mean temperatures of each transect of the AUV track (compare marked temperature levels in top panel of Fig. 5.14).

The temperature spectrum was calculated for each of the segment using 10 min long data segments. These were transformed into isotherm slope spectra (Eqn. 3.16) with the local mean temperature gradients. All spectra show similar slopes which are largely consistent with those of the inertial-convective subrange of turbulence ($k^{1/3}$) (Fig. 5.14 (lower panel), black dashed line). For instance, much higher energy is observed in part E compared to part A at the same wave numbers. The integral of the spectra over the wave number range 0.03 cpm < k < 0.3 cpm (corresponding to wave length of 210 > λ > 21 m) gives a measure of the energy of motion on turbulent scales from the isotherm displacement. The upper and lower integration limits are chosen to be in the range of the best fit to the slope of the universal spectrum and to exclude influences of the vertical motion of the vehicle (compare to Fig. 5.10, grey lines).

Those results are compared to the mean dissipation rates observed by the AUV-based MSP based on shear probes in each segment. The data is more or less represented by a straight line in the log-log space (Fig. 5.15, black dashed line). Thus there is a direct relation between the integrated isotherm slope spectra (i.e., the variances of isotherm displacement) and the mean turbulent dissipation rates calculated from the MSP (Fig. 5.15).

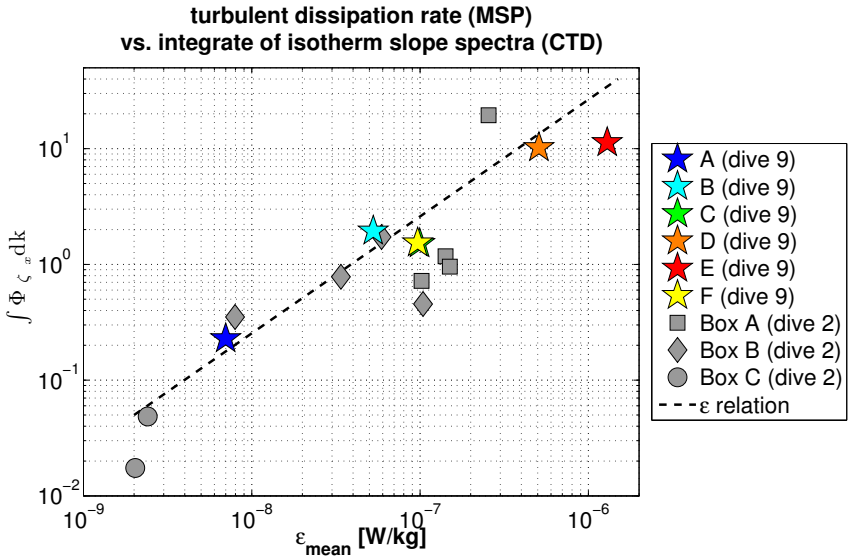

Figure 5.15: Variances of isotherms displacements computed from the AUV-CTD compared to turbulent dissipation rates from the AUV-MSP. Both datasets are obtained by horizontal profiling with the AUV. Subsamples were chosen from AUV dives 2 and 9 along tracks at constant depths with approximately constant temperature values. Wave number isotherm slope spectra were calculated from temperature spectra using local temperature gradients estimated from ship-lowered CTD profiles. Each spectrum is integrated between 0.03 cpm and 0.3 cpm in order to cover the inertial-convective subrange of turbulent motion. The mean dissipation rates are calculated over the same segments based on data of the MSP. Colored stars show results of the transects from AUV dive 9 (compare to Fig. 5.14). Grey markers denote results from AUV dive 2 (compare to Fig. 5.1). Herein the grey cycles are achieved from segments in the ambient water, the grey squares from segments of tracks 1, 4, 5, and 6 where high temperature fluctuations were detected, and the grey diamonds from segments of tracks 2, 3, 5, and 6 where low temperature fluctuations were detected (see Fig. 5.1).

In addition, the vertical motion of the AUV is related to turbulence as seen, for instance, in Fig. 5.7. It is possible to relate the integrated energy of depth fluctuations to turbulent dissipation rates for the specific instrumentation of the AUV. The same segments of AUV dive 9 are used as before (A-F, see Fig. 5.14, top panel) to compute gradient depth spectra from the vertical displacement of the AUV (see section 5.3.1, Fig. 5.10). A relation between the integrated gradient spectrum of depth from the AUV pressure sensor and the mean dissipation rates is found (Fig. 5.16). At dissipation rates below $(3 \cdot 10^{-7}) \frac{W}{kg}$ the integrated gradient spectra show very low values of $\leq (3 \cdot 10^{-4})$ cpm^{-1} (black dashed line). For larger ϵ, the values from the vertical depth variations of the vehicle increase and a straight line in log-log space is observed (black solid line). Thus above a threshold of $(3 \cdot 10^{-7}) \frac{W}{kg}$ the variances of depth gradients are related to the turbulent dissipation rates.

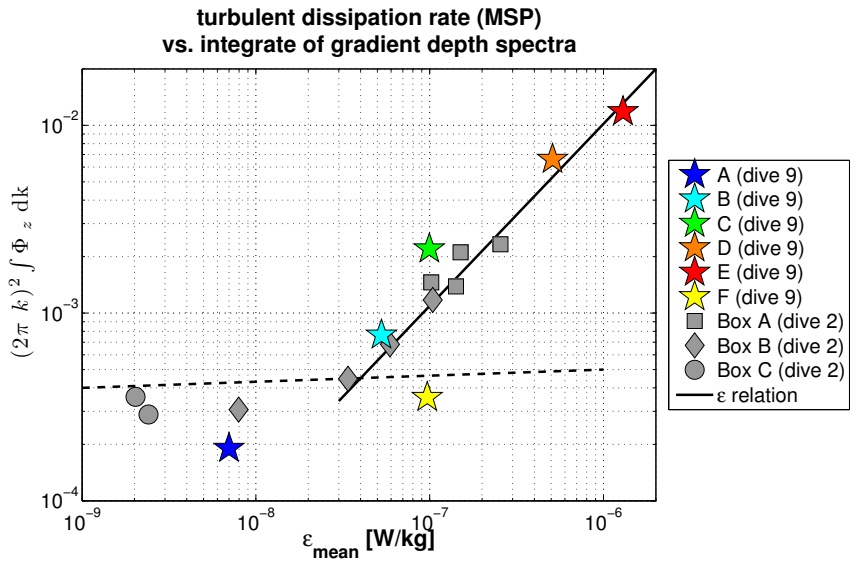

Figure 5.16: Integrated gradient depth spectra from the AUV-pressure compared to the mean dissipation rates of the AUV-MSP. (See caption of Fig. 5.15 for explanation.)

5.5 Discussion

Turbulence sampled in the DSO plume along horizontal AUV tracks

The horizontal AUV profiles of dive 2 cover the mixed bottom layer of the DSO plume as well as the interfacial layer and ambient water (Fig. 5.1). Additionally a cold and fresh intrusion is observed along four tracks extending over a depth range of 1260 m to 1340 m in the vicinity of a topographic elevation (see Fig. 5.1, magenta box). This feature is present throughout the dive with the tracks having been taken up to 5 hours apart from each other. Spectral analysis shows higher variances at these segments (box A) compared to segments at the same depth but further apart from the elevation (box B) (see Fig. 5.15). The dissipation rates are two orders of magnitude higher in the same location than at same depth levels at larger distance from the topographic elevation (Fig. 5.6). High dissipation rates of $\mathrm{O}(10^{-6})\frac{W}{kg}$ are found extending horizontally over 600 m especially at the upper-most track. Both high dissipation rates and the variations in hydrographic characteristics imply that pronounced vertical mixing occurred in the vicinity of the 70 m topographic elevation (see map in Fig. 5.2).

The highest dissipation rates, in comparison of all AUV missions, are observed during dive 9 (Fig. 5.17). Here dissipation rates of $\mathrm{O}(10^{-6})\frac{W}{kg}$ over 4 km distance (Fig. 5.7) and high fluctuations in potential density (Fig. 5.4) are seen. The density changes are governed by varying contributions in Θ and S as seen in the Θ-S diagram (Fig. 5.3). At first (0 to 4 km) the salinity decreases from 34.91 to 34.87 while Θ remains constant. Then (4 to 8 km) Θ varies from 1 °C to 1.7 °C while S is constant. In the middle of the

track (8 to 12 km) both Θ and S vary. In the end (12 to 17 km) S varies only slightly (34.93 ± 0.01) and high temperature fluctuations between 1.4 ° and 2.5 °C are observed.

During the pronounced changes in salinity the MSP measured an increase in ϵ over two orders of magnitude (Fig. 4.11). Wavelet analysis of the salinity time series indicates high energy during the observed low salinities during the first half of the track (Fig. 5.12). The salinity variances can be associated with variability on length scales of 100 to 400 m. At the same time and the same length scales high energy in the wavelet PSD of the temperature is found (Fig. 5.11). The high variances and increasing dissipation rates may indicate vertical mixing.

Wavelet analysis of the temperature time series shows even higher energy during the second half of the long track on length scales of 700 m down to the lowest scales of 13 m (Fig. 5.11). The global wavelet PDS shows that most energy is found on scales below 500 m. The larger scales are in the range of internal waves[2]. During the same time dissipation rates of $O(10^{-6})\frac{W}{kg}$ are found (Fig. 5.7). The temperature wave number spectrum of the whole time series of dive 9 indicates small-scale variability on dominantly turbulent scales in the inertial-convective subrange between 21 m and 210m (Figs. 5.8, 5.9). The contamination of the spectra by vertical movements of the AUV is negligible (Fig. 5.10).

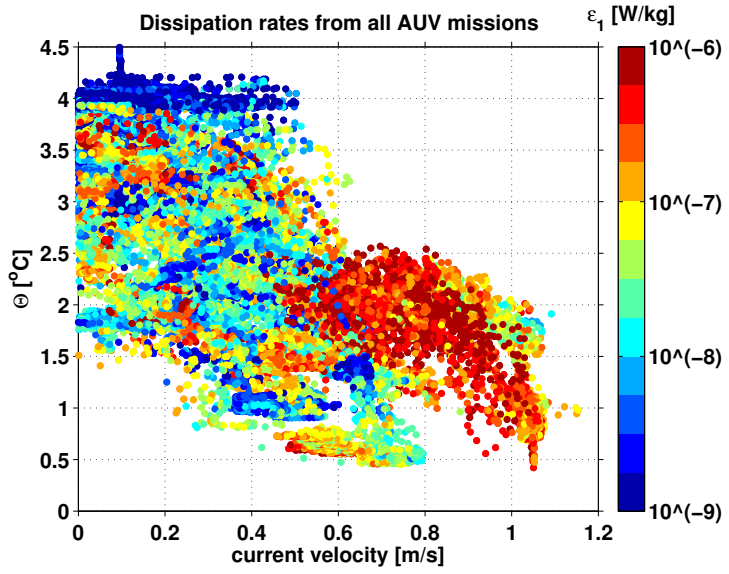

Figure 5.17: Dissipation rates from all successful AUV missions in the main working area (see map in Fig. 2.3) as a function of potential temperature and current velocity.

In general most of the highest dissipation rates of $O(10^{-6})\frac{W}{kg}$ are observed during high current velocities (0.6 - 1.1 $\frac{m}{s}$) and potential temperatures in the range of 0.5 °C to 2.5 °C (Fig. 5.17). In order to understand the enhanced small-scale variability observed during dives 2 and 9 the physical surroundings will be discussed in the following chapter 6.

[2]Lowered CTD profiles show N $\leq$ 0.006 s^{-1} which corresponds to $\lambda \geq$ 320 m.

Spectral subranges

Spectral analysis applied to the variances of temperature as well as to isotherm displacement shows that spectral slopes are parallel to slopes of universal spectra expected in the inertial-convective subrange (Figs. 5.8, 5.9). The comparison of various isotherm slope spectra from segments of AUV dive 9 indicates that, especially for regimes with large variances, the spectral slopes are parallel to $k^{1/3}$, correspondingly to the inertial-convective subrange (Fig. 5.14, segments D and E). For less turbulent segments the spectral slope declines from low to high wave numbers and is rather parallel to $k^{-1/2}$ which corresponds to the internal wave subrange (Fig. 5.14, segment A).

A spectral slope corresponding to the inertial-diffusive subrange cannot be observed at small length scales in any of the analysis (i.e. k^1 for isothermal slope spectra in Fig. 5.14). This might be caused by an insufficient temporal resolution and/or due to the inertia of the system. The flow through the CTD measurement system is limited as it is attached rather close to the AUV hull (see Fig. 2.4, photo B). A CTD mounted at a further distance from the hull could enhance the flow rate through the pumped system. The fast thermistors of the MircoRider provide a high temporal resolution (512 Hz) and are attached to the AUV with sufficient distance from the hull. Thus spectral analyses could be applied to the thermistor data in the same way as it was applied to the temperature data from the CTD for comparison.

Estimates of ϵ by isotherm slope and temperature spectra

As discussed above the spectral slopes of both the temperature and the isotherm slope spectrum are parallel to the equilibrium spectrum of the inertial-convective subrange. The amplitude of the temperature spectrum is dependent on ϵ and the dissipation of temperature variance χ_T (see Table 3.1). Respectively, the amplitude of the isotherm slope spectrum depends on ϵ and χ_ζ. Here χ_ζ is given by χ_T scaled with the background temperature gradient. Thus to estimate ϵ from the spectra one needs to know the dissipation of temperature variance. This can be estimated based on the Osborn method following *Klymak and Moum* (2007a) by

$$\chi_T = 2\frac{\Gamma\epsilon}{N^2}\left(\frac{\partial T}{\partial z}\right)^2. \tag{5.1}$$

A mean background vertical temperature gradient and mean background buoyancy frequency need to be assumed to approximate χ_T in order to apply this to a regular CTD system (*Klymak and Moum*, 2007a). This introduces uncertainties as the background stratification varies in the interfacial layer of the DSO plume. These uncertainties are avoided in the analysis by considering only the integrated spectra in comparison with

dissipation rates derived from the MSP. This comparison is reliable as the estimate of ϵ by shear probes of the MSP is computed at a wave number range that does not overlap with the wave number range of the temperature/isotherm displacement spectrum.

The errors of using a mean background stratification can be reduced by evaluating local temperature gradients from the ship-lowered CTD profiles during the AUV tracks. By splitting the dive into several segments local background conditions were used to transform temperature to isotherm slope spectra. The local temperature gradients calculated for temperature classes yield $\frac{dT_0}{dz} = 0.0217 \pm 0.0046 \frac{^\circ C}{m}$ (compared with Fig. 5.13).

Due to the sensibility of the background stratification one may test whether isotherm slope spectra provide more reliable information compared to horizontal wave number spectra of temperature. Comparison of the integrated wave number spectra of temperature

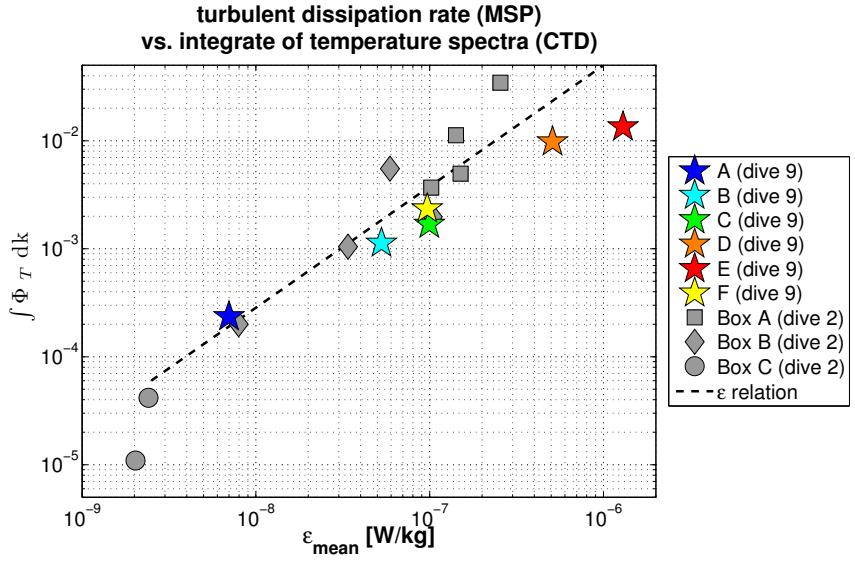

Figure 5.18: Integrated spectra of temperature from the AUV-CTD compared to mean dissipation rates from the MSP. (See caption of Fig. 5.15 for explanation.)

computed over the same segments as the isotherm slope spectra yields a similar relation to mean ϵ values computed from the MSP (Fig. 5.18). On the other hand the the slope spectrum shifts the spectrum to higher wave numbers and thus it is easier to distinguish between the spectral slopes of internal wave subrange ($k^{-1/2}$) and inertial-convective subrange ($k^{1/3}$).

Uncertainties in the analyses can be introduced by the choice of the integral width over the inertial-convective subrange. Still the chosen range is reasonable and for comparable settings a similar range (0.04 cpm $\leq$ k $\leq$ 0.4 cpm) was used by *Klymak and Moum* (2007a).

Other sources of errors are: At first the effect of the vertical movement of the AUV especially during high current speeds. Still this effect is found to be small. Secondly the transformation from frequency to wavelength domain based on the assumption of a

finite speed of 1.6 $\frac{m}{s}$ of the AUV through the water (Taylor hypothesis). Thirdly the assumption of isotropy which may be not true on large wave numbers (e.g., [pp. 183-184] *Thorpe* (2005) and references therein). And lastly errors induced within the applied methods of spectral analysis (e.g., *Emery and Thomsen* (2001, pp. 432-440)).

The pressure data of the AUV can provide estimates of turbulent dissipation rates additional, although a relatively high noise level at about $(3 \cdot 10^{-8})\frac{W}{kg}$ is found (Fig. 5.16). The vehicle is programmed to respond to vertical changes keeping the AUV on a horizontal track. As this response is specific to the navigation scheme used by this platform this analysis is restricted to the AUV.

5.6 Summary

Horizontal profiling with an AUV yields a closer insight into horizontal scales of turbulent motion. Two major turbulent events are detected in/above the DSO plume. The first is found within dive 2 in the vicinity of a topographic elevation. The second event occurred during the long profile of dive 9. Here wavelet analysis indicates elevated temperature fluctuations on time scales of 8 s to 5 min and wavelength of 13 m to 500 m. High energy on these scales is found especially where the turbulent dissipation rates are high, on the $O(10^{-6})\frac{W}{kg}$. Horizontal wave number spectra are found to be in reasonable agreement with universal spectra of the inertial-convective subrange of turbulent motion on wavelength between 21 m to 210 m. By sub-sampling the dataset it is possible to show a relation between the variance of isotherm displacement (computed from AUV temperature data) and mean dissipation rates from the MSP. In addition variances of depth (based on AUV pressure data) agree well with mean dissipation rates from the MSP. A direct estimate of ϵ from the temperature/isotherm slope spectra by comparison with universal spectra of the turbulent subrange is challenging. This is due to the dependence on the variable background conditions in the DSO plume.

Chapter 6

Spatio-temporal structure of the DSO plume during the AUV missions

The DSO plume changes its hydrographic characteristics on its path from the DS sill downstream along the Greenland continental slope. Meso-scale eddies traveling with the DSO plume dominate the variability and change the characteristics of the DSO plume. Within this chapter the DSO plume conditions in the mean working area during the AUV missions are described based on moored measurements and ship-lowered CTD/LADCP data. Firstly, observations from the different measurement platforms are analyzed in order to describe varying DSO plume conditions with respect to meso-scale variability. Afterwards these observations are used to study the plume conditions during the AUV missions focussing in more detail on the observations during dives 2 and 9. Finally, the effects of meso-scale eddies on mixing is analyzed with respect to the observed small-scale variability during AUV dive 9.

6.1 Spatial structure of the DSO plume in the working area

The DSO plume gets thicker, broader, and less dense as it entrains water during its downstream propagation(see Fig. 1.6). Similar changes are observed by comparing the three long CTD sections (DS, 30°W, 31.4°W) obtained during the cruise MSM21/1b (see map in Fig. 2.1). Here the focus is set on the structure of the plume in the mean working area about 180 km downstream of the DS sill. Fig. 6.1 shows the potential temperature (left) and along-stream velocity (right) sections across the DS sill and across the Greenland

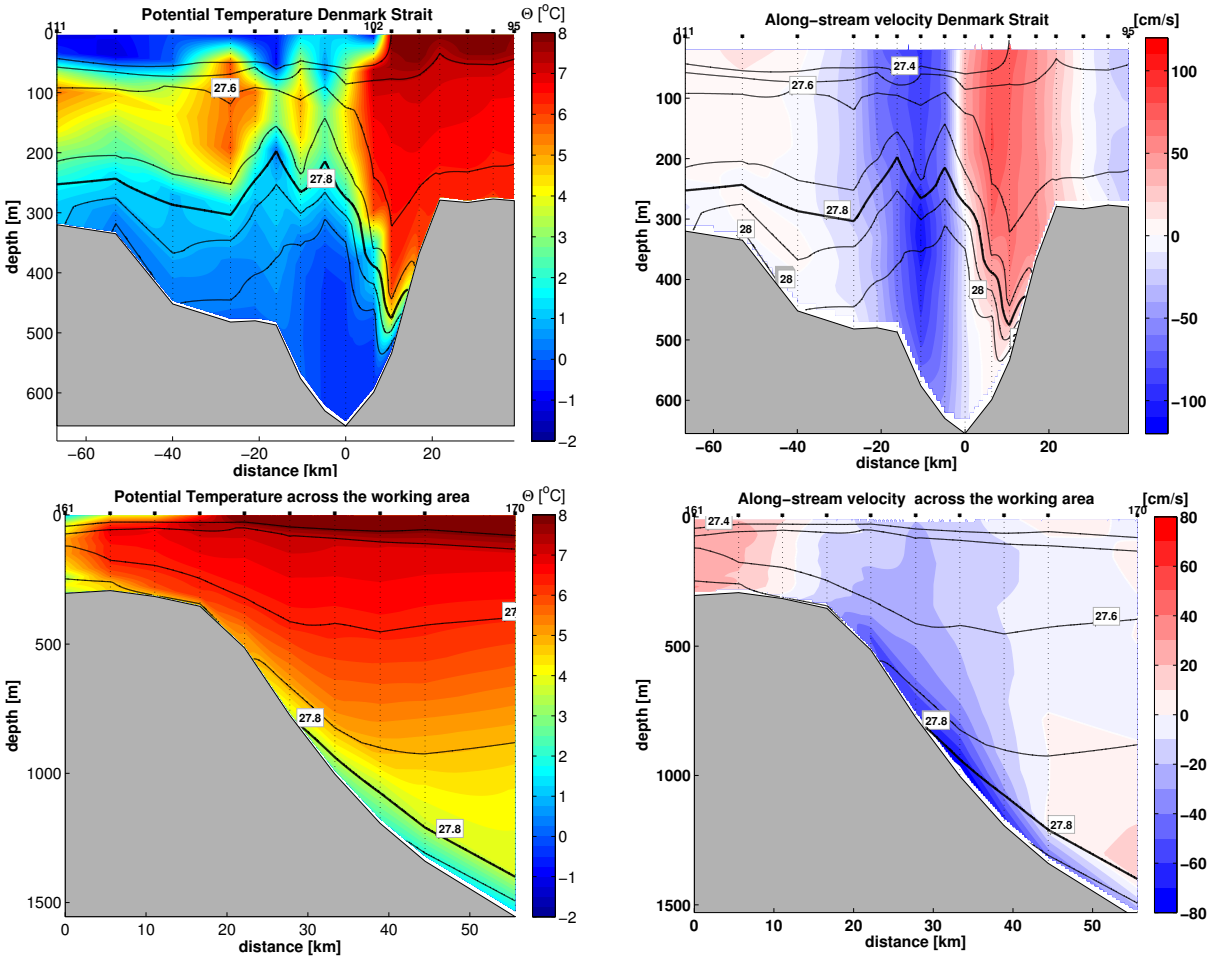

Figure 6.1: Potential temperature (left) and along-stream velocity (right) sections from CTD/LADCP profiles across the Denmark Strait sill (upper panel) and across the continental Greenland slope (grey shading) in the mean working area 180 km downstream from the sill (lower panel) during MSM21/1b. Potential density contours are superimposed on all sections. Note the different limits of the color ranges for the along-stream velocity sections.

continental slope reaching into the working area.

The DS sections show that cold ($\Theta = 0.4°$) water is observed in the deepest 200 m of the DS with densities of 28 $\frac{kg}{m^3}$. This dense water is transported southward through the DS and feeds the DSO plume. Towards the east (Fig. 6.1, kilometers 0 to 10) a sharp front separates the southward flow from northward-flowing warm water on the Iceland continental shelf. This water can be associated with the Icelandic branch of the Irminger Current.

In the working area the DSO plume is indicated by along-stream velocities larger than 0.5 $\frac{m}{s}$ and dense water ($\sigma_\Theta \geq 27.8$ $\frac{kg}{m^3}$) at the bottom below 800 m. The plume is cold ($\sim$ 2 °C), fresh ($S \leq 34.9$), and oxygen rich ($O_2 \geq 300$ $\frac{\mu mol}{kg}$) compared to the ambient water and has a slight downslope velocity component (not shown). Water with densities

above 27.9 $\frac{kg}{m^3}$ is only seen at the deepest CTD station ($\sim$ 1550 m). The DSO plume extends most probably even further downslope as observed e.g., by *Rudels et al.* (2002) (section PsVI).

6.2 Temporal variability of the DSO plume in the working area

6.2.1 Meso-scale variability observed by current profilers

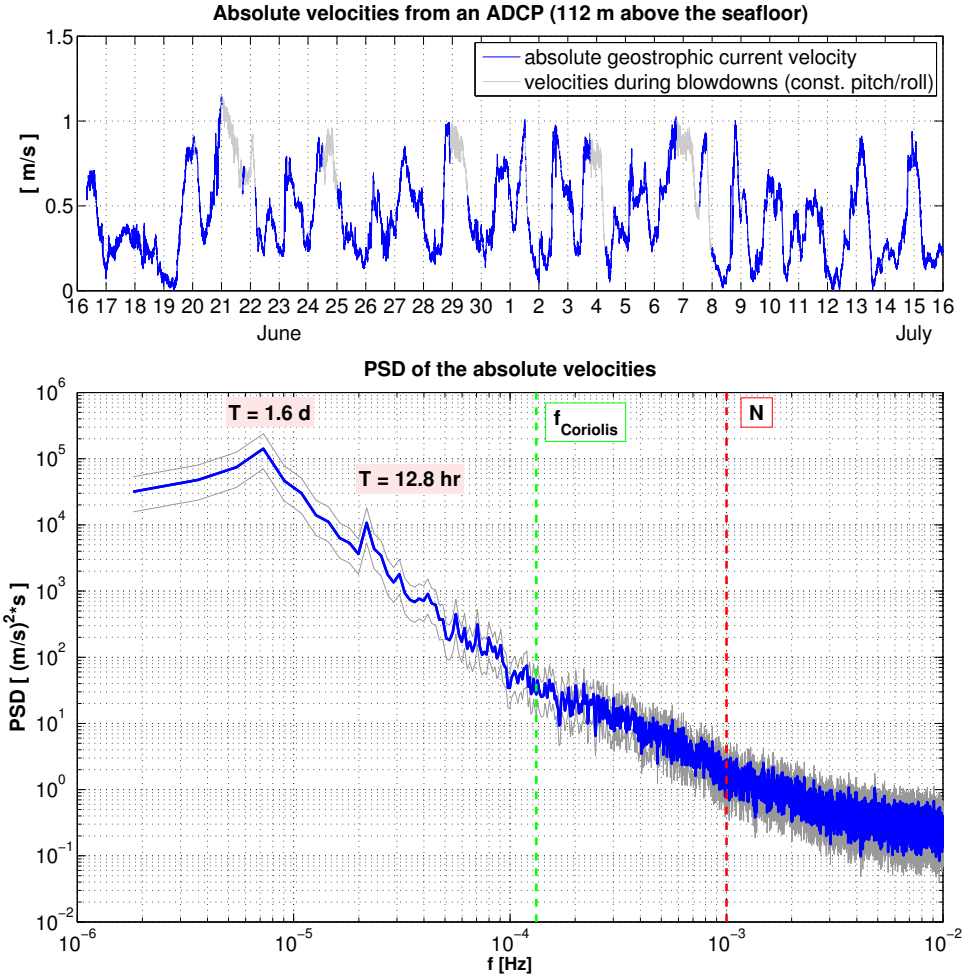

Figure 6.2: Time series (upper panel) and PSD (lower panel) of the absolute velocity from an ADCP 112 m above the seabed at the DS19 mooring site. In the upper panel, current speeds observed during times when the ADCP exceeded its tilt range (see section 2.4.2) are marked in grey. In the lower panel the frequency spectrum (blue) and the corresponding 95 % confidence intervals (grey) are given. The mean buoyancy frequency (red dashed line), the inertial frequency (green dashed line), and the periods [day] of the peaks found at low frequencies are marked. (The PSD is calculated using eight data segments with a length of 6.4 day each.)

The time series of current speeds observed by the ADCP at the central mooring DS19 frequently shows peaks between 0.8 $\frac{m}{s}$ and 1.2 $\frac{m}{s}$ (see Fig. 6.2, upper panel). In oder to examine the period of these velocity peaks spectral analysis is applied to the velocity time series. The first peak which deviates from the spectrum corresponds to a time period of 1.6 d, the second to a time period of approximately 12 hrs 50 min. A time series analysis using the current data of the Aquadopps yields similar results (not shown). The period of 1.6 d can be associated with the passage of meso-scale eddies. No signal is detected in the range of the inertial period. The signal at 12.8 hrs is caused by semi-diurnal tides.

6.2.2 Temporal changes in hydrographic properties associated with meso-scale eddies

The passage of meso-scale eddies recorded by the moored current meters can be linked to changes in hydrographic characteristics of the DSO plume. A large dataset of temperature and salinity data was collected by different platforms in the working area in order to observe the plume characteristics and variability. An interpolated potential temperature field was computed from MCs and T-recorders of the central mooring DS 19 (see map in Fig.2.3), covering the range between 27 m and 194 m above the seafloor (dependent of the depth of the sensors). The salinity field, computed from the MCs, is filtered with a cutoff of 10 min and interpolated between 27 m and 144 m above the seafloor (dependent on the depth of the sensors). Fig. 6.3 shows the potential temperature (upper panel) and salinity (lower panel) field obtained during the first 5.5 days after the deployment of the mooring. Generally a strong gradient in the hydrographic characteristics separates warm and salty ambient water at the top ($\Theta \geq 4°C$, S $\geq$ 34.94) from cold and fresher plume water ($\Theta \leq 1°C$, S $\leq$ 34.88) deeper down. The vertical gradients in Θ and S vary within the shown time window. For instance, the temperature gradient is twice as strong on June 21 ($\frac{d\Theta}{dp} = \frac{7.5°C}{100dbar}$) compared to that on June 17 ($\frac{d\Theta}{dp} = \frac{3.75°C}{100dbar}$). The most dominant signal is the shift in temperature on June 19. During the first part of the time series the pressure levels of the MCs (black lines) are smooth and the warm, salty water extends down to 1320 dbar (16.06., 20:00 - 18.06., 4:00) and to 1380 dbar (19.06., 2:00 - 12:00). In contrast, pressure levels deepen and show high variability on small time scales on June 19 and June 21 which can be associated with the passage of eddies. The upper-most MC is pushed down almost 70 dbar within a day. The potential temperature appears to be very low ($\Theta \leq 1°C$) over the whole depth range of the moored devices. This cold bolus implies the core of an eddy. The salinity is around 34.9 which is between the two water masses observed during the first days.

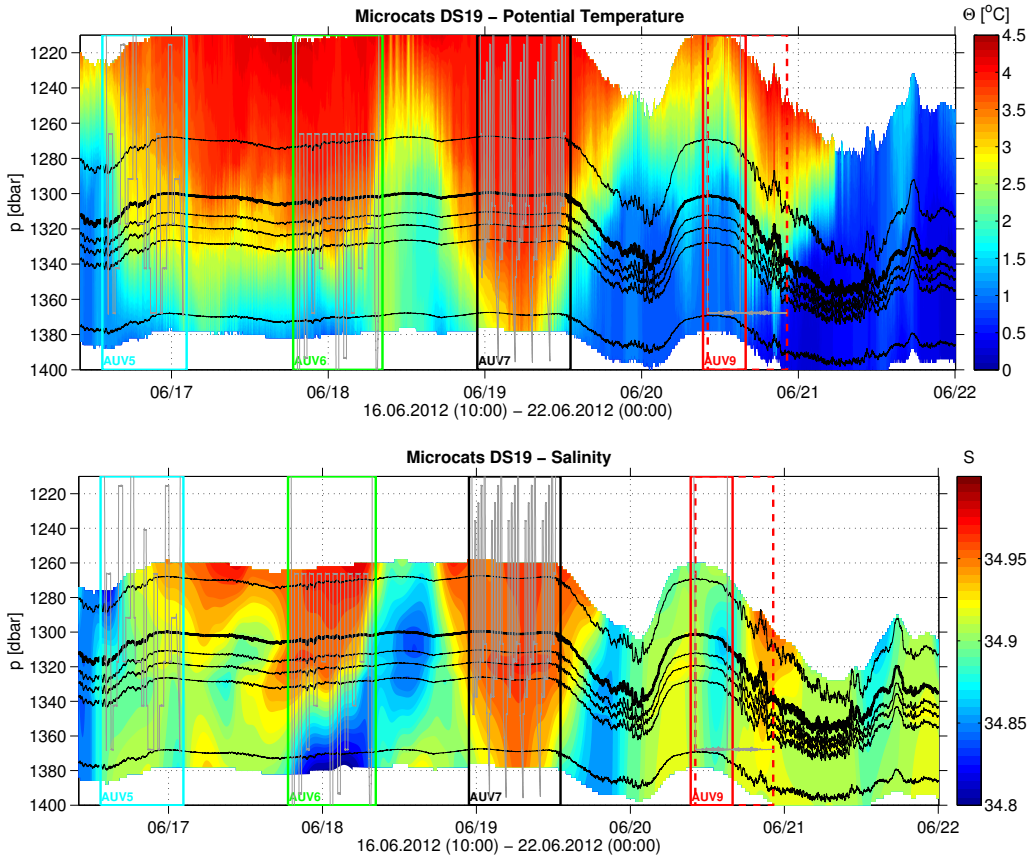

Figure 6.3: Time series of potential temperature (upper) and salinity (lower) profiles computed from the MCs and T-recorders of the DS19 mooring. Black lines mark the pressure levels of the MC sensors. In addition, the times when AUV dives were carried out close to the central mooring site are marked. Grey lines represent the pressure levels of the AUV dives. The temperature field is unfiltered while the salinity field is filtered with a cutoff of 10 min to reduce noise.

Additional results can be obtained from the CTD yo-yo data. The time series of the four yo-yos are one to three hours long and cover a larger and higher resolved vertical range compared to the moored hydrographic data. At yo-yo stations 172 and 173 the hydrographic characteristics are almost similar showing a very thin plume layer (Fig. 6.4). The well mixed bottom plume layer is less than 30 m thick (using the 27.9 $\frac{kg}{m^3}$ contour as an upper limit). The plume is relatively warm ($\Theta \simeq 2°C$) and saline ($S \simeq 34.91$) during these times. About 6.5 hours later, during profile 177, a much thicker plume is observed ($\geq 100m$). The water within the well mixed bottom plume layer is colder ($\Theta \leq 1.5°C$), fresher ($S \leq 34.88$), and more rich in oxygen (not shown) compared to the earlier profiles. These observations likely can be linked to an incoming eddy.

Additionally changes in salinity are observed in the ambient water. The water is slightly fresher during yo-yo 177 than during stations 172 and 173.

The observed changes in hydrographic observations by the MCs as well as during the

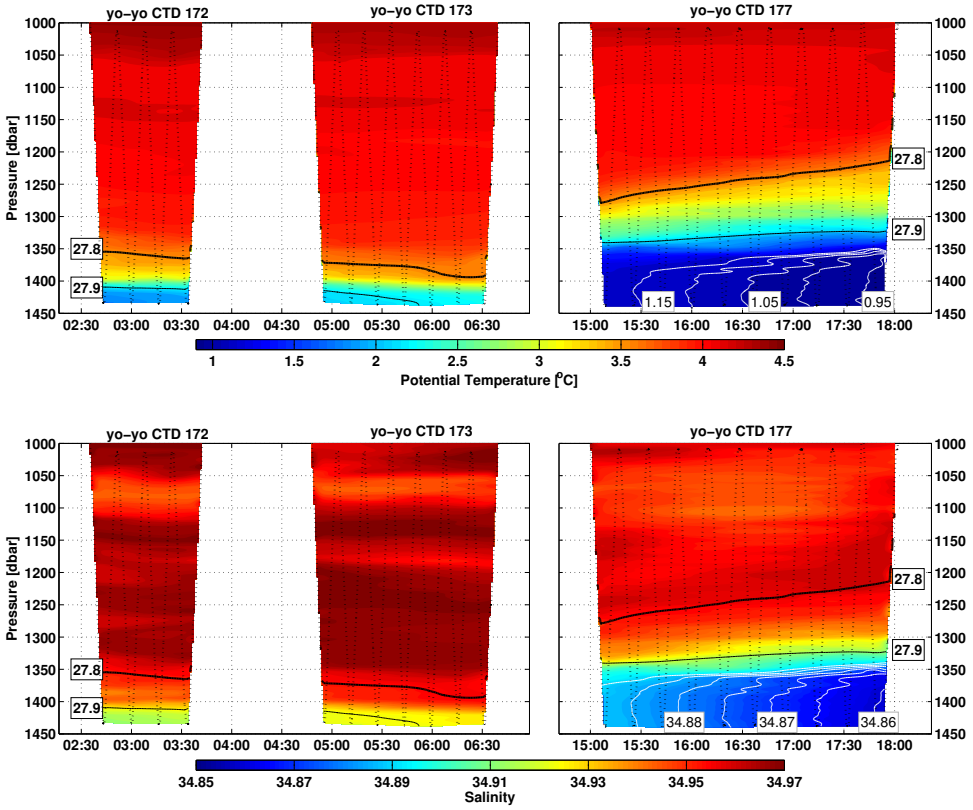

Figure 6.4: Potential temperature (upper panel) and salinity (lower panel) sections from the three CTD yo-yo profiles carried out between 1000 dbar and 10 m above the seafloor at the same central site in the mean working area on June 19 (see map in Fig. 2.3). Dotted black lines show the origin of the data while the shown fields are interpolated onto a constant grid and filtered (see section 2.3.1). The thick black line marks the 27.8 $\frac{kg}{m^3}$ contour, the thin black line the 27.9 $\frac{kg}{m^3}$ contour. White lines in yo-yo profile 177 mark chosen isolines of Θ (upper panel)/S (lower panel) in the DSO plume.

yo-yos indicate that the DSO plume is a mixing product of different waters. It changes in time due to the passage of eddies. Cold fresh boluses of waters are associated with the passage of eddies. Thus the data is discussed with respect to the passage of meso-scale eddies through the working area and linked to the observations from the AUV missions below.

Another way to analyze the hydrographic variability of the DSO plume is to compare all CTD profiles carried out in the main working area at repeated spots (map in Fig. 2.3). These can serve best to compare with data from the AUV missions because they were carried out closest to the AUV dives. Fig. 6.5 shows data from all these CTD profiles in depths ranging from the seafloor to 400 m above it. The profiles collected within these nine days reflect the strong hydrographic variability at depth. Within the mixed boundary

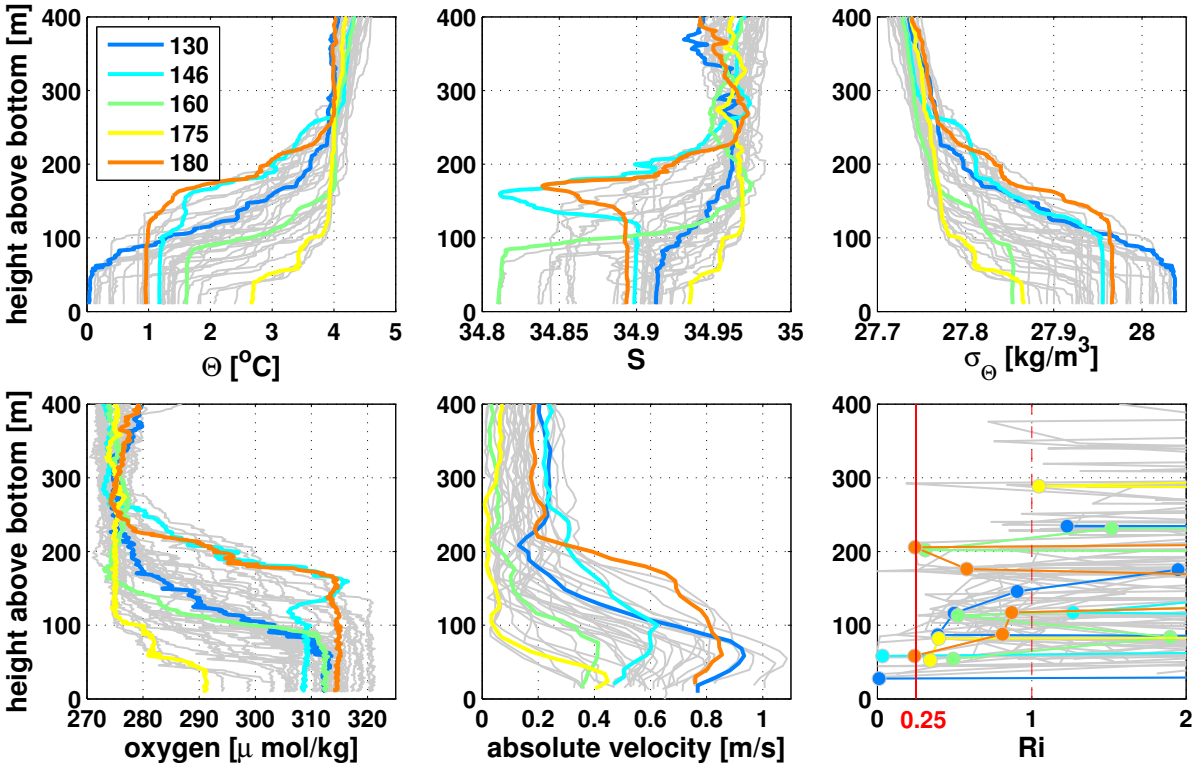

Figure 6.5: CTD profiles from all repeated CTD stations in the central working area. Given are from left to right potential temperature Θ, salinity, and potential density in the upper panels and oxygen, absolute velocity, and Richardson numbers in the lower panels. The different colors indicate five exemplarily chosen stations (stations 130, 146, 160, 175, and 180).

layer the potential temperature varies by more than 2 °C and the salinity by about 0.1. Consequently differences in potential density of up to 0.2 $\frac{kg}{m^3}$ are observed. Maximum changes of about 30 $\frac{\mu mol}{kg}$ in the oxygen content of the plume are observed. A large range of maximum core velocities, spreading from about 0.4 $\frac{m}{s}$ to 1.1 $\frac{m}{s}$, is seen by examining the absolute velocity profiles.

Five CTD profiles exemplary for different states of the DSO plume are highlighted in Fig. 6.5. The yellow profile was observed during low core velocities at CTD station 175. The bottom layer of the plume is about 50 m thick and compared to most other profiles warm (2.8 °C), saline (34.93), and low in oxygen (291 ml/l). A second homogeneous layer of about the same thickness as the bottom layer is observed above the core. During stations 130 (dark blue) and 160 (light green) the core of the plume has a thickness of about 60 to 80 m. The oxygen levels are similar (312 $\frac{\mu mol}{kg}$), while the plume water at station 160 is lighter (27.85 $\frac{kg}{m^3}$) due to very fresh (34.81) and relatively warm (1.6 °C) conditions. In contrast station 130 reflects the densest ($\sim$ 28.04 $\frac{kg}{m^3}$) and coldest ($\sim$ 0 °C) plume conditions observed during the cruise. The plume is saline (34.92) and shows large absolute core velocities of up to 0.95 $\frac{m}{s}$. Stations 146 (cyan) and 180 (orange) reflect an

even thicker plume layer of about 150 m core thickness. The plume characteristics range around the mean for all profiles ($\Theta \approx 1$ °C, S ≈ 34.9, $\sigma_\Theta \approx 27.96$ $\frac{kg}{m^{-3}}$, dissolved oxygen $\approx$ 310 $\frac{\mu mol}{kg}$). In both profiles the plume is covered by a low salinity lid about 180 m above the seafloor. At station 146 the water has a minimum in salinity of 34.81 and a maximum in oxygen content of 316 $\frac{\mu mol}{kg}$ at this depth. The potential temperature is relatively cold (1.5°C) and the absolute velocity is 0.45 $\frac{m}{s}$. At station 180 the salinity lid has a slightly smaller gradient with S = 34.84 but similar temperature and oxygen values. The absolute current speed is large (0.7 $\frac{m}{s}$).

In general it seems that a fast plume transports cold water. Large current speeds and a low salinity lid is observed during thick plume conditions. A thin plume shows varying characteristics. The maximum plume velocities are commonly observed in or on top of the mixed boundary layer.

L_O [m]		N [Hz]				
		0.001	0.002	0.003	0.004	0.005
ϵ	10^{-6}	31.6	11.2	6	4	2.8
	10^{-7}	10	3.5	1.9	1.3	0.9

Table 6.1: Ozmidov scales [m] computed from typical values of N (i.e., the root of stratification based on lowered CTD profiles) and ϵ (i.e., dissipation rates based on the AUV-MSP) in the DSO plume.

Richardson (Ri) numbers were calculated based on stratification N^2 and velocity shear S_v (Eqn. 3.3). In order to exclude the turbulent motion, it is desirable to evaluate Ri numbers at spatial scales larger than typical Ozmidov scales (Eqn. 3.11). Ozmidov scales were computed based on the stratification and dissipation rates measured in the DSO plume (see Table 6.1). By this a 30-m-scale was chosen and applied to N^2 and S_v as a 30-m-running-mean to compute Ri numbers. Critical Ri values are most often observed close above the seafloor (Fig. 6.5). At station 180 (orange) critical Ri values related to a very strong velocity gradient are observed at around 200 m above the seafloor.

The information gained from the CTD/LADCP profiles will be linked to the AUV dives in the following section.

6.3 DSO plume conditions during the AUV missions

All AUV missions were carried out close to the central moorings and the repeated CTD stations (see map in Fig. 2.3). Thus, the velocity and hydrographic data from the mooring DS19 and ship-lowered CTD/LADCP profiles can serve to characterize the DSO plume conditions during each AUV mission. In the following the data from the AUV missions

will be analyzed in the context of certain plume layers and varying characteristics of the plume due to meso-scale variability.

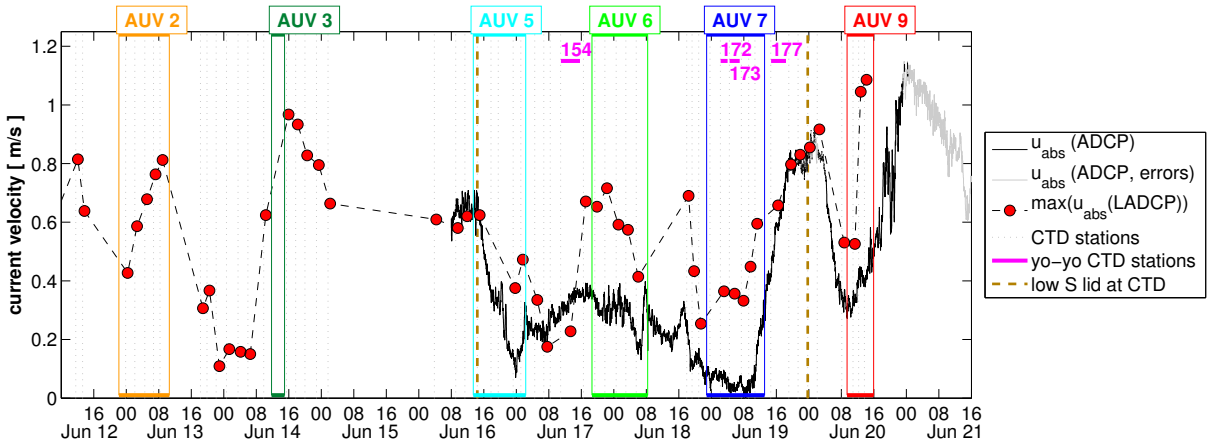

Figure 6.6: Absolute velocity maxima of each LADCP profile (red dots) and current speeds observed from the moored ADCP (DS19) (black/grey line). The times during which AUV missions and CTD yo-yos (magenta) were carried out are marked by colors (see legend for details). The brown dashed lined mark CTD stations 146 and 180 where strong low salinity lids were observed (see Fig. 6.5).

The current speeds observed from the moored ADCP and the largest speeds observed at each LADCP station associated to plume velocities (see Fig. 6.5) are used to study the meso-scale variability during the AUV missions (Fig. 6.6). A decrease in current speed is observed during AUV dives 5 and 6. During the four other AUV missions an increase in the absolute current velocity can be seen. The highest speeds of about 1.1 $\frac{m}{s}$ occur during AUV dive 9 in the LADCP profiles. Similar high speeds are collected in the moored ADCP data about 7 hours later.

In addition to the plume velocity, it is of interest to distinguish in which part of the DSO plume the AUV missions were carried out. It can be seen from the CTD profiles in Fig. 6.5 that the plume height of the mixed boundary layer varies between 50 m and 150 m. The AUV tracks were carried out in the range between 45 m and 200 m above the seafloor, covering different parts of the plume. Fig. 6.7 illustrates in which part of the plume the AUV dives were carried out based on the plume layer definitions given in chapter 2.3.2. As mentioned in the chapters before, the horizontal tracks at different depth levels during dive 2 and dive 6 captured all parts of the plume - the mixed bottom layer, the interfacial layer, and the ambient water. During all other dives the purpose was to capture the interfacial layer. AUV dives 5 and 9 collected data just above the bottom layer interface in the interfacial layer. During dive 7 the AUV collected data within the upper part of the interfacial layer. Here, in the beginning and the end of the dive, the upper interface of the interfacial layer is above the AUV which measured changes in Θ-S characteristics. However the AUV likely sampled ambient water in between (compare with

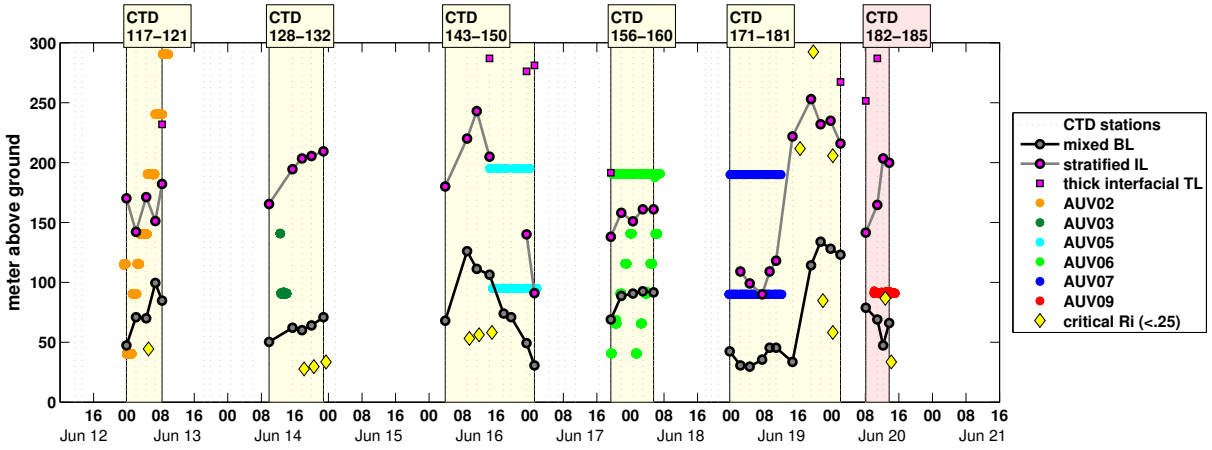

Figure 6.7: Mixed bottom layer (BL, black line with grey dots), interfacial layer (IL, grey line with magenta dots) and transition layer (TL, magenta squares) for all repeated CTD stations (light yellow shading) and CTD stations 182-185 (light red shading) from the short section in the mean working area (map in Fig. 2.3). In color the long AUV dives carried out simultaneously to some of the CTD stations are marked at their altitude levels. Yellow squares indicate critical *Ri* numbers computed from lowered CTD/LADCP profiles.

section 4.2). The tracks carried out 200 m above the seafloor during dives 6 and 7 were located in the ambient water, while the tracks during dive 5 were likely carried out within a second homogeneous layer (TL). Critical *Ri* numbers outside the mixed bottom layer are only observed during dive 9. Additionally the hydrographic data from the moored MCs given in Fig 6.3 indicate that the bottom layer thickness strongly increases from June 20 until June 22.

Of main interest is to study entrainment by vertical mixing the interfacial layer between the well-mixed overflow plume and the ambient water. This is captured best during dives 2, 5, and 9. Due to the chosen mapping mode the analysis of dive 5 appears to be problematic (see chapter 4.3), the aim in the following section is to link the meso-scale variability to observed variability in dives 2 and 9.

6.3.1 Plume conditions during AUV dive 2

The CTD profiles carried out during AUV dive 2 show that the plume velocity increased from 0.4 $\frac{m}{s}$ to 0.8 $\frac{m}{s}$ and that the plume thickens from about 50 m to 100 m (referred to as the mixed bottom layer) (Fig. 6.8). This indicates the passage of an eddy. In addition the plume gets colder (from 0.9 °C to 0.4°C) while the salinity stays constant over the time at 34.91. These observed changes give additional information to the AUV observations during dive 2 (presented in chapter 5.1.1), which is discussed in section 6.4.

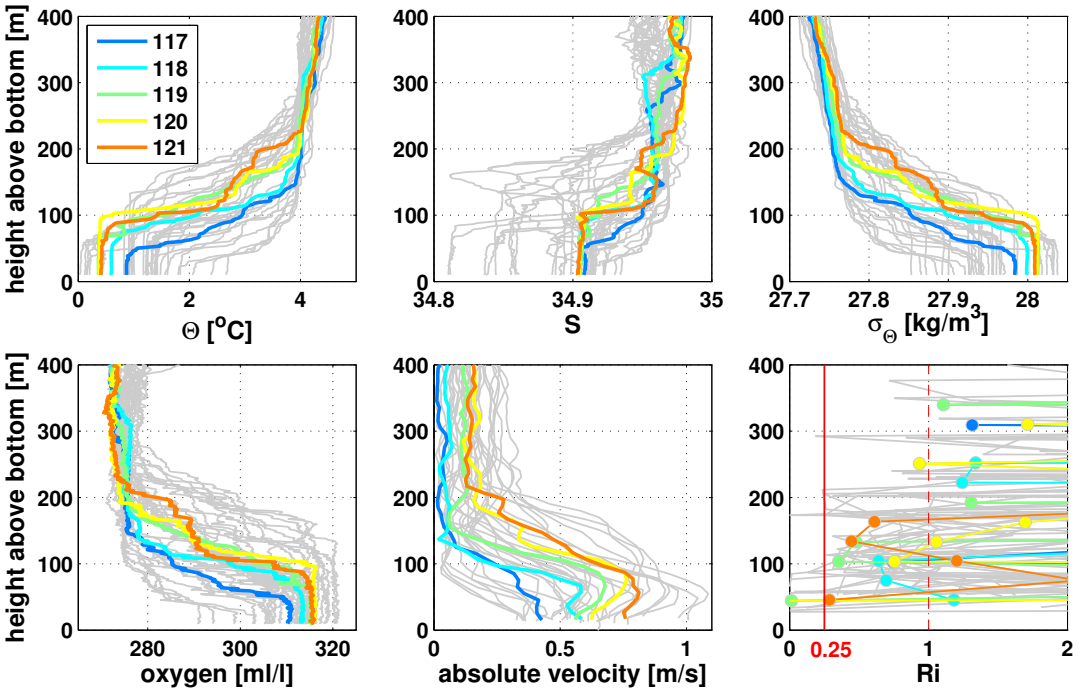

Figure 6.8: Plume properties at CTD stations (117 - 121) carried out after each other during AUV dive 2. (See caption of Fig. 6.5 for explanation.)

6.3.2 Plume conditions during AUV dive 9

During AUV dive 9 a large increase in plume velocities from 0.55 $\frac{m}{s}$ up to 1.1 $\frac{m}{s}$ is observed in the LADCP profiles (Fig. 6.6). The absolute velocity is dominated by the along-stream velocities (Fig. 6.9). In profiles 182 and 185 a positive cross-stream velocity of about 0.4 $\frac{m}{s}$ is additionally observed which indicates a downslope movement of the plume. In profile 182 both along- and cross-stream components are of the same magnitude (0.4 $\frac{m}{s}$). Above 140 m the along-stream velocity shows negative values which is against the mean plume direction. This indicates the structure of an internal wave. Profile 183 shows a similar, but less pronounced signature. Positive velocity gradients with maxima at 100 m above the plume are found in all profiles. The largest largest velocity gradients of 1 $\frac{cm}{s}$/m are found at stations 184 and 185.

The increase in plume velocities found in the LADCP data can be compared to the velocity calculated from the AUV itself (Fig. 6.10). This is based on the assumption that the AUV is heading exactly against the mean current direction and therefore its speed above the ground decreases at the same rate at which the plume speed increases. Both the AUV-inferred current velocity and the LADCP current velocity (90 ± 10 m averaged) show an increase in current velocity from about 0.4 $\frac{m}{s}$ at 10:00 to 0.85 $\frac{m}{s}$ at 14:00. The AUV-inferred velocities reach even higher values of 1.05 $\frac{m}{s}$ at 15:00. An increase in current speed is also observed in the data from the moored RCM located

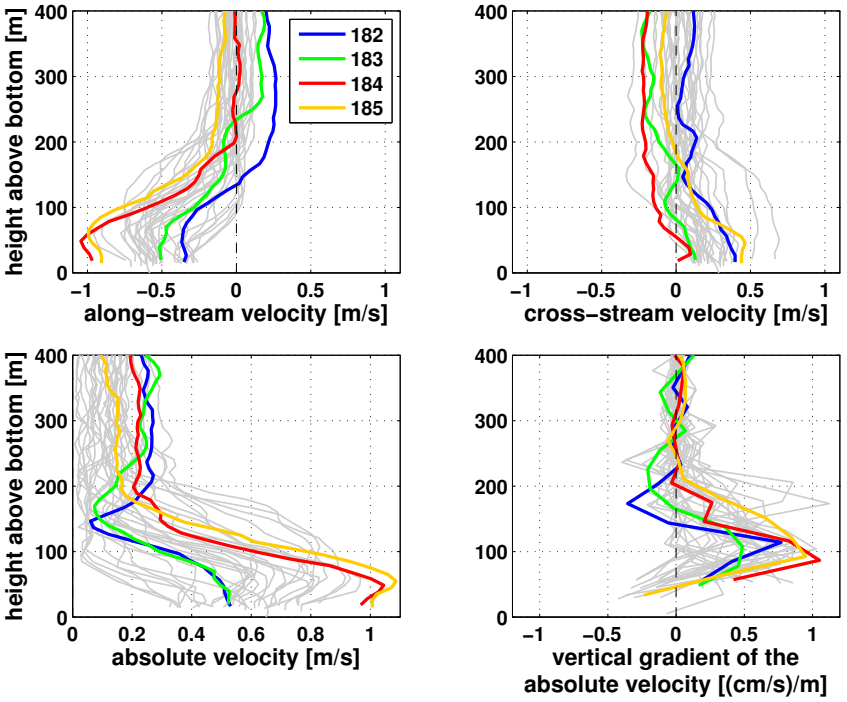

Figure 6.9: LADCP vertical velocity profiles of stations 182 - 185 (blue, green, red, and yellow lines respectively) from 400 m above down to the seafloor. The along-stream (top left), the cross-stream (top right), the absolute (bottom left), and the gradient of the absolute velocities (bottom right) are given. Grey lines show all repeated LADCP profiles in the central working area.

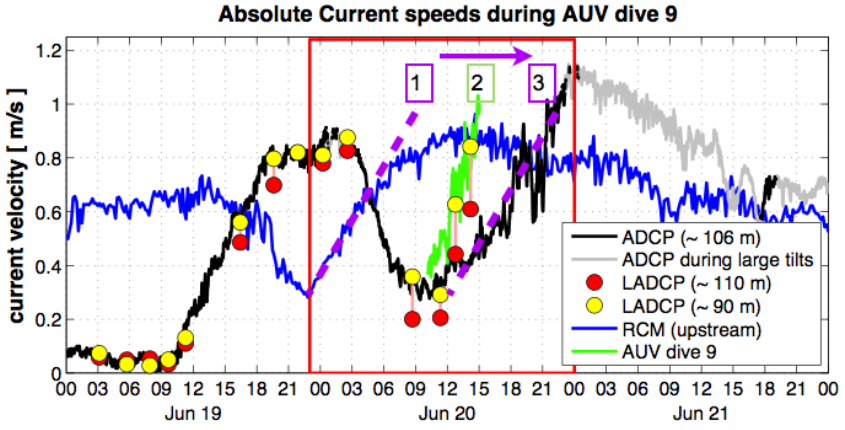

Figure 6.10: Current speeds from the RCM 16.7 km upstream (blue line), the ADCP (DS19) in the centre of the mean working area (black line), LADCP profiles from repeated stations in the mean working area and along the track of AUV dive 9 averaged between 90 m (yellow) and 110 m (red) above the ground, and from AUV-inferred velocity during dive 9 (green line). The purple dashed lines indicate the increase in current speed and how this signal propagates downstream from the RCM (DS13) to the AUV/LADCP track down to the ADCP at the central mooring site (DS19) (compare to map in Fig. 2.3).

16.7 km further upstream (see map in Fig. 2.3) from 0:00 to about 9:00 on June 20. A similar increase as seen at DS13 is observed at the central mooring DS19 from 11:00 to 23:00 on June 20 with about the same slope (Fig. 6.10, indicated by the dashed purple lines). The best current correlation of the time series collected by the ADCP at DS19 compared to the RCM at DS13 is found by shifting the RCM 10.5 hrs forward in time. This gives a travel time of $v = \frac{16.7 \cdot 1000m}{10.5 \cdot 60^2 s} \approx 0.44 \frac{m}{s}$. Thus if a signal propagates downstream with a mean travel time of 0.44 $\frac{m}{s}$ it can be assumed that a similar increase in current speed will be observed at the central mooring about 10.5 hours later as seen in Fig. 6.10. The AUV was diving from the central mooring upstream toward to the RCM site within this time. Thus, the AUV captured the same signal as observed by the moored devices but with a stronger slope because it was moving against the propagation direction of the signal, inducing effects of the Doppler shift.

The AUV most likely captured by chance parts of an eddy diving through the interfacial layer of the DSO plume. This is supported by changes to a very cold and thick plume layer in the MC data as well (see Fig. 6.3).

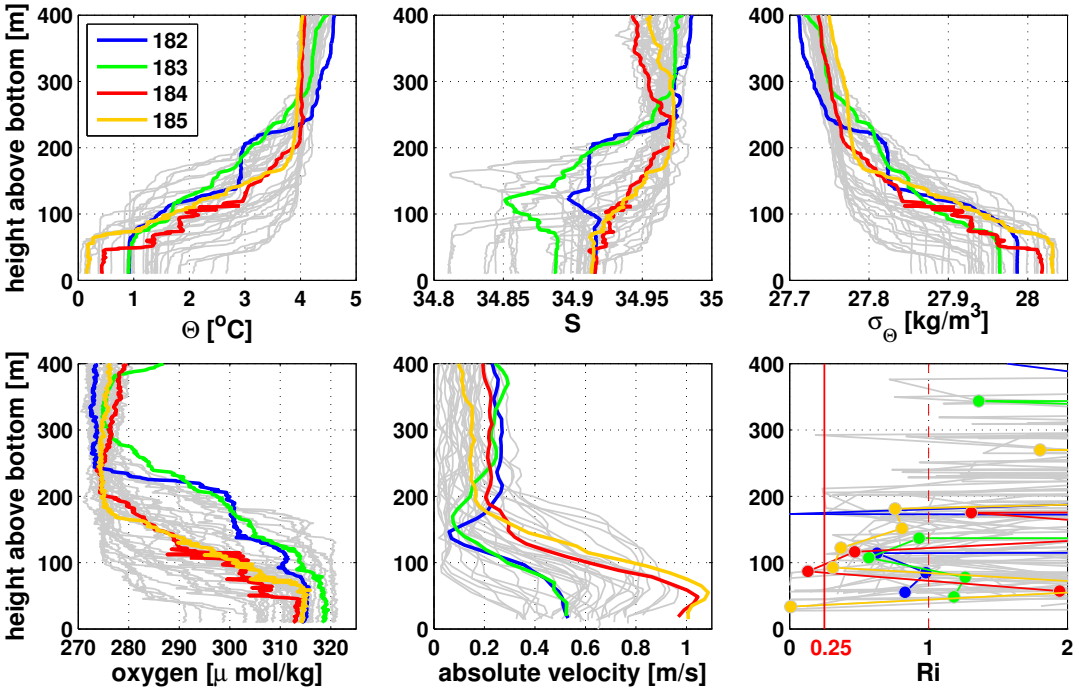

Figure 6.11: Hydrographic and velocity profiles from the four CTD stations carried out parallel to AUV dive 9. (See caption of Fig. 6.5 for explanation.)

The CTD profiles 182 to 185 collected during dive 9 resolve these changes in the vertical. Profiles 182 and 183 show similar characteristics but differ from profiles 184 and 185. Thus two classes of varying plume characteristics can be observed. The well-mixed plume shows similar characteristics within all four profiles: it is very cold 1 °C (182) to 0.1 °C (185), has salinities of 34.92 (despite slightly fresher values in profile 183 of 34.89)

and is very dense ranging from 27.97 $\frac{kg}{m^3}$ (183) to 28.3 $\frac{kg}{m^3}$ (182). The plume is oxygen rich in all profiles (314 $\frac{\mu mol}{kg}$ - 319 $\frac{\mu mol}{kg}$). Although the hydrographic characteristics in the mixed bottom layer of the plume are about the same, the plume velocities differ largely as shown before (Fig. 6.9). Profiles 182 and 183 show velocities of 0.5 $\frac{m}{s}$ while the current speeds of the plume in profiles 184 and 185 reach 1.1 $\frac{m}{s}$. Additionally the interfacial layer above the mixed BL of the plume varies between both classes. During profiles 182 and 183 a low salinity lid at about 120 m above the seafloor is observed. This was also captured by the AUV observations (see section 4.4, Fig. 4.11). A 100 m thick homogeneous transition layer extending from above the lid to about 240 m above the seafloor is observed. It includes a layer with uniform properties of 3 °C, S = 34.91, and 301 $\frac{\mu mol}{kg}$ (182) and an increase in absolute velocity up to 0.25 $\frac{m}{s}$ extending from 140 m up to 200 m above the seafloor. This layer is covered by a second gradient layer in which the velocity stays constant. About the same characteristics are noticed in profile 183 but less pronounced. Here the salinity shows an even more distinctive minimum of 34.85 above the mixed bottom layer. A much stronger gradient of hydrographic properties in the interfacial layer and no second homogeneous transition layer is observed in profiles 184 and 185. Conspicuous are high fluctuations of potential temperature and oxygen as well as critical Ri numbers in the interfacial layer both implying vertical motion. These observations will be discussed below with respect to meso- and small-scale variability.

6.3.3 AUV observations near the edge of an energetic eddy

The hydrographic variability and velocity signals from the mooring as well as from the AUV-based data indicate that the AUV was sampling data while passing through parts of an eddy during dive 9. With respect to the high dissipation rates and turbulence observed during dive 9 (discussed in chapter 5), it is of interest to study this event in more detail.

The AUV captured parts of a meso-scale eddy indicated by the minimum velocity of 0.4 $\frac{m}{s}$ in the beginning (10:00) and maximum velocity of 1.1 $\frac{m}{s}$ in the end (15:00) of its dive which is comparable to the observed velocities in the mooring DS19 (Fig. 6.12, first panel). The observations from the moored ADCP indicate that the plume velocities turn towards the shelf during the increase of velocities (Fig. 6.12, second panel). In contrast, earlier from 0:00 to 10:00 the velocities decrease from 0.9 $\frac{m}{s}$ to 0.4 $\frac{m}{s}$ and show a downslope component. This could imply that a cyclonic eddy passed the central mooring with its western side (illustrated in Fig. 6.13). Considering the AUV, dive 9 could have started inside an eddy, corresponding to relatively low velocities, and subsequently the AUV was diving out of the eddy. Another option could be that the moored ADCP sampled the western-most flanks of two cyclonic eddies following each other or the downslope side of an anticyclonic eddy, within the given time window. Nevertheless, the strong increase in

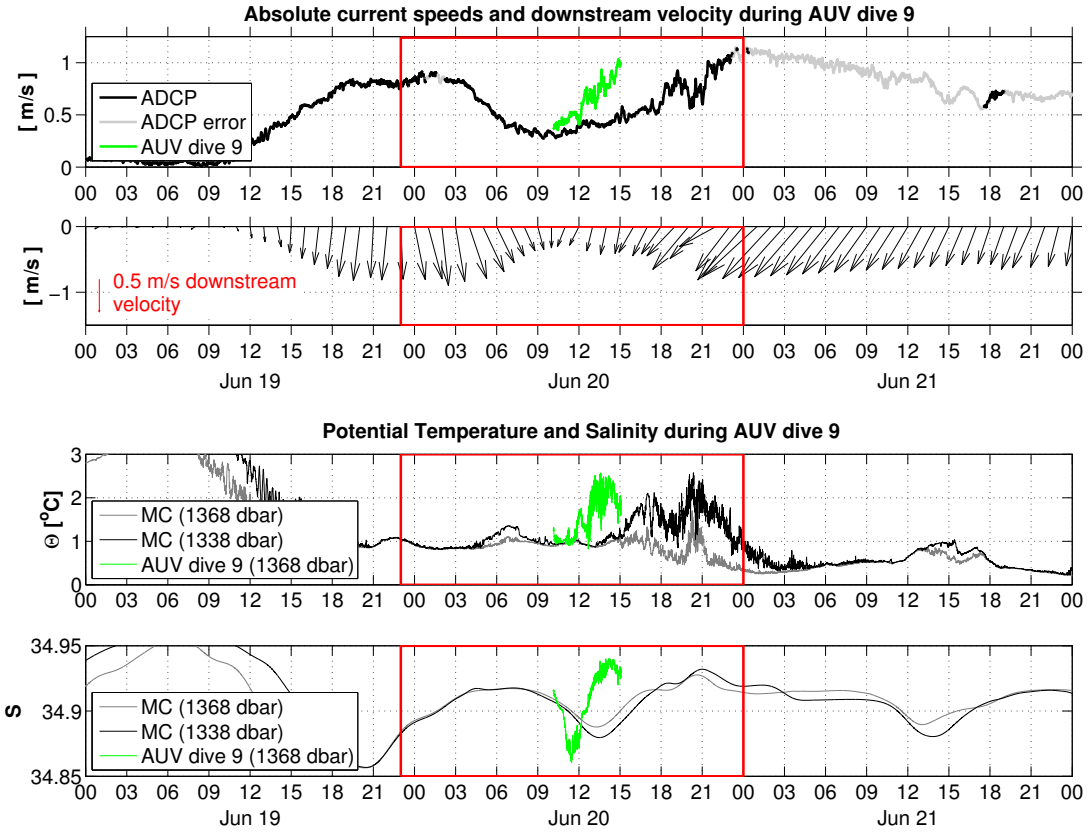

Figure 6.12: Moored data of the central mooring DS 19 over three days (19.-21.06 2012) in comparison to data collected by AUV dive 9 at one depth level (91 m above the seafloor). The upper two panels show velocity data. The first gives absolute current speeds from the moored ADCP (112 m above the seafloor) (black) in comparison to the AUV-inferred velocity (green). The second shows the direction of the current from the ADCP. Here a vertical downward pointing arrow is related to the downstream velocity component. Thus arrows pointing to the left indicate an upslope component while arrows pointing to the right indicate downslope velocity components. The lower two panels show the potential temperature (upper) and salinity (lower) from the MC at two depth levels (black 1338 dbar, grey 1368 dbar) in comparison to the data collected during AUV dive 9 (green).

current speed during AUV dive 9 implies that the AUV was measuring near the edge of an energetic eddy. During the transition from low to high plume velocities the potential temperature collected by the AUV increases from 1 °C to temperatures fluctuating around (2 ± 0.5) °C (Fig. 6.12, third panel). Similar changes were observed in the MC but 30 dbar above the AUV. The salinity varies from 34.92 (10:00) to a minimum of 34.87 (11:30) and later to a maximum of (34.94 - 34.95) in the end of the dive (Fig. 6.12, fourth panel). Such changes are also observed in the downstream moored MCs. The mooring data show that after the transition to strong current speeds the velocity keeps high values of about 1 $\frac{m}{s}$ which slightly decline (0:00-12:00) (Fig. 6.12, first panel). Here cold temperatures (Θ = 0.5 °C) are observed which can be associated with the core an

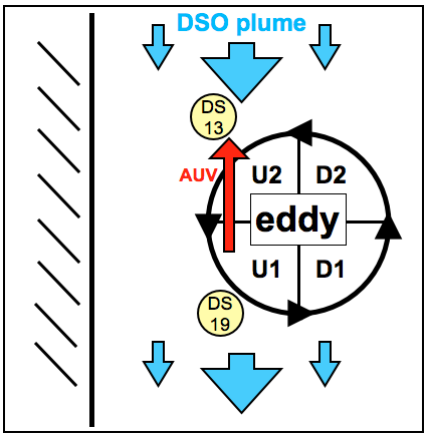

Figure 6.13: Sketch of an cyclonic eddy traveling with the DSO plume (blue arrows) downstream from the DS sill along the Greenland continental slope (left side). The eddy is divided into four parts. The two parts towards the shore (upslope) are named U1 and U2, towards the open ocean (downslope) D1 and D2. The red arrow indicates the AUV diving through the eddy. Thus the numbers of the eddy parts indicate which side of the eddy is collected first by the AUV. In addition the mooring sites DS13 and DS19 are marked at their approximate position.

eddy. A decrease in temperature is also indicated at the end of the AUV dive. Based on these consistent observations, the data collected during dive 9 can be interpreted in regard to observations near the edge of an energetic eddy.

6.4 Discussion

Entrainment and meso-scale eddies

The differing plume characteristics can be linked to the frequent passage of meso-scale eddies traveling with the plume. The moored current meter observations in June 2012 indicate that meso-scale eddies passed the working area with a period of 1.6 days. This is slightly more frequent than the earlier observations of periods of 2 to 5 days close to the sill (*Bruce*, 1995). All five current meters at the central mooring showed a similar period here, which makes the value appear robust. The cyclonic eddies transport source water enriched with ambient water into the working area (*Jungclaus et al.*, 2001). The moored MCs as well as the yo-yo profile 177 captured the characteristics during the passage of an eddy associating cold boluses with cyclonic eddies. This is supported by an increase in current speed observed in the LADCP profiles at plume depth as well as by an increase in current speeds observed by the moored ADCP.

Although the moored MCs did not cover the whole plume the passage of one or two eddies within the 5.5 day long time series can be detected (Fig. 6.3). The full time series showed many realizations of eddies (not shown). This is assumed based on the decrease

in all pressure values indicating a deepening of the moored instruments and the change to very cold dense plume conditions. In the evening on June 19 the introduced water mass was about 1°C and fresh (34.86). The variability on the pressure data on small scales might indicate high frequency velocity fluctuations. The yoyo CTD 177 measured hydrographic properties during the same time, capturing the water column from the bottom up to 1000 dbar (Fig. 6.4). The plume extends up to 250 m above the seafloor with a 100 m thick mixed plume layer while before (at profiles 172 and 173) the plume was very thin, salty, and warm. At profile 177 the properties get fresher and colder with time in the bottom layer while above the conditions stayed constant.

The MC data show a second transition into very cold (about 0°C), dense water about one day later on June 20 (Fig. 6.3). The pressure sensors indicate large current speeds and turbulence again. AUV dive 9 was carried out in the beginning of this transition and most likely passed through some part of an eddy. This assumption is supported by increasing current speeds calculated from the vehicle as well as from LADCP data. In addition the moored velocity data upstream and at the central mooring indicate that an eddy traveled with the DSO plume through the working area (see Fig. 6.10). The AUV was located in the interfacial layer close above the mixed bottom layer (Fig. 6.7). It captured a region of high entrainment caused by vertical mixing over two hours (see chapter 5). The temperature fluctuations ranged between (1.5-2.5) °C. The rather warm and saline (34.93) water collected during high dissipation rates may indicate entrainment of ambient water in the interfacial layer. At the same time the hydrographic properties observed in CTD profile 184 showed high fluctuations in the interfacial layer (Fig. 6.11). Large vertical velocity shear and low Ri numbers in the interfacial layer indicate vertical instability here as well (see Fig. 6.11). Thus the instabilities are generated at the interface between the interfacial and the bottom layer rather than by bottom-generated turbulence. The boundary layer characteristics changed only slightly while the interfacial layer characteristics vary a lot between the profiles 182/183, collected in the first part, and 184/185 collected in the second part of the AUV dive. It is assumed that the upper part of the plume is merging with ambient water. Here both vertical and lateral fluxes seem to play a role. During the AUV mission the moored velocities show an increase and turn towards the continental shelf. This implies horizontal advection of ambient water towards the shelf. There could be an interaction of eddy-driven lateral advection of ambient water and entrainment by vertical mixing on the side of eddies. These results implicate that the use of a multi-platform approach successfully provides a deeper insight into meso- and small-scale variability in the DSO plume which likely can be linked to each other.

If the results are robust there might be comparable to former studies which suggested that eddies can double the vertical entrainment in the FBC overflow plume *Seim et al.* (2010).

Entrainment vs. mixing of source water masses

In general, transport values indicate that entrainment by diapycnal mixing needs to play a role in the formation of deep water because the source water masses alone do not contribute enough to feed the observed overturning (see chapter 1).

More general implications of entrainment can be achieved from analyses of watermass-based Θ-S changes associated with diapycnal mixing. When comparing the water mass properties in the working area to those properties found at the DS sill, it is found that the plume is warmer, saltier, and less dense. The changes in hydrographic characteristics of the descending plume are commonly thought to be caused by mixing of the different source waters and/or entrainment of the ambient water by diapycnal mixing (e.g. *Rudels et al.* (1999)).

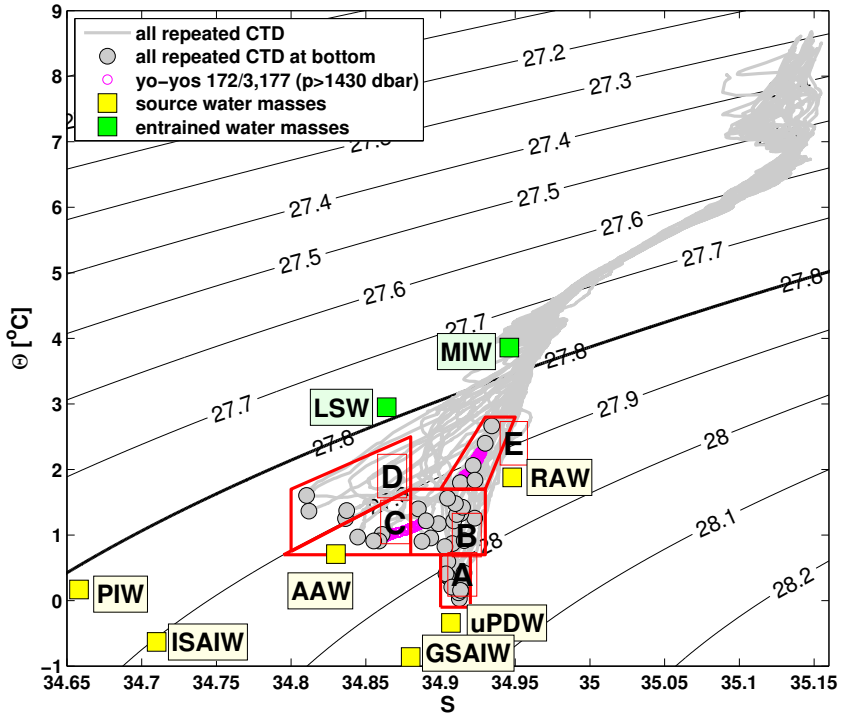

Figure 6.14: Θ-S-diagram of all CTD profiles at the three repeated stations in the central working area (map Fig. 2.3). For simplicity the bottom value of each profile is supposed to be representative for the plume characteristics at each station. The deepest values of the CTD profiles are marked by grey dots. The deepest values (below 1430 dbar) of the yo-yo CTD profiles are marked by pink circles. The same stations as in Fig. 6.5 are highlighted with colors. The Θ-S characteristics collected during dive 9 are marked in light red. Source water masses based on *Rudels et al.* (1999) are marked in yellow. The MIW, which is most likely an entrained water mass, is labeled in green. The DSOW characteristics about 500 km downstream are labeled in red. All water mass properties are based on *Tanhua et al.* (2005).

Five different types (A - E) of plume characteristic are identified, based on Θ-S-

watermass type	Θ [°C]	S	(σ_Θ) [kg/m^{-3}]	most likely origin
A	-0.05 - 0.6	34.9 - 34.92	≥ 28	dense Arctic Ocean water
B	0.8 - 1.6	34.88 - 34.93	27.92 - 27.98	supplied by EGC warm Atlantic layer
C	0.8 - 1.6	34.84 - 34.87	27.92 - 27.95	supplied by EGC, less dense thermocline layer
D	1 - 2.5	34.8 - 34.88	27.84 - 27.9	gradually homogenized PIW
E	1.8 - 2.8	34.91 - 34.93	27.85 - 27.92	source waters mixed with MIW

Table 6.2: Water mass classes observed in the DSO plume from several ship-lowered CTD profiles. Gives are the ranges of the hydrographic properties of each watermass type named alphabetically from A to E.

diagram of all repeated CTD stations and yo-yo CTDs in the mean working area (Fig. 6.14, Table 6.2) Several water masses are marked in Fig. 6.14 in order to identify if the observed water characteristics can be formed by the different source waters. The DSO plume water at the sill is most likely formed of two mixing products of RAW/AAW and uPDW/AIW which should gradually homogenize by diapycnal mixing in the descending DSO plume (*Rudels et al.*, 2002). A high fraction of PIW is found at the sill as well creating a low salinity lid capping the plume (*Tanhua et al.* (2005), *Rudels et al.* (1999)). By comparing the source water masses defined by *Rudels et al.* (2002) (marked in Fig 6.14 by yellow squares) with the CTD data, all characteristics within the watermass types A, B, and C could be explained simply by internal mixing of the initial source water masses. Nevertheless, it depends on the relative contributions of the source waters whether the observed water characteristics can be formed. MIW or water with a similar density class could also be entrained and mix with the source water masses to form the observed water mass characteristics (see chapter 1).

Cold, fresh ($S_{min} = 34.81$), and oxygen rich intrusions capping the mixed bottom layer of the DSO plume are observed in 15 of 37 CTD profiles and identified as the low salinity lid. Observations in 1999 showed a much fresher lid of almost 34.7 in about the same location (*Rudels et al.*, 1999). The more saline characteristics in June 2012 could indicate that the source waters at the sill were more saline. This is possible because this least dense part of the plume is quickly responding to changes in the conditions in the Nordic Seas (*Tanhua et al.*, 2005). The occurrence of a lid moving on top of the descending plume indicates that little entrainment of ambient water by vertical mixing took place along the plume path (*Rudels et al.*, 1999). More than half of the CTD profiles at repeated stations in the central part of the mean working area showed no salinity lid which could indicate that diapycnal mixing occurs locally. Some profiles even show that water with similar

fresh characteristics is occasionally found at the bottom (e.g., profile 160 compared to the lid in profile 146, Fig.6.5). This fresh and warm plume water (type D) could be a mixture of modified PIW and water from the interfacial layer of the plume.

The type E characteristics found in some CTD profiles show the warmest and saltiest conditions of the plume. During these profiles the plume was very thin as seen e.g. in profile 175 (Fig. 6.5) and at the yo-yo stations 172/173 (Fig. 6.4). When the plume is thin bottom-generated turbulence can create large enough entrainment to change properties of the overflow plume (*Paka et al.*, 2013).

It should be noted that the given water mass analysis is based on characteristics of source water masses which are still under discussion. In addition, characteristics of the source waters at the sill probably vary in time due to a temporal change in the strength and position of the EGC and the Irminger Current as a dominant source of the DSO overflow (*Rudels et al.*, 2002). The overall role of entrainment and the characteristics of possible entrained water remain open.

The role of waters from the shelf

With respect to the water mass analysis waters from the shelf could play a role to be entrained in the DSO plume as well. The CTD section across the Greenland continental slope at 30°W (map in Fig. 2.1) in June 2012 showed relatively warm (1.5 °C) and salty (34.92) plume conditions (Fig. 6.1). The 27.8 $\frac{kg}{m^3}$ isopycnal indicates that the plume extends from 800 m down the slope reaching highest densities of 27.94 $\frac{kg}{m^3}$ at the deepest station. In contrast a section collected about 3 months later in August 2012 reaching across the shelf and down the Greenland continental slope (see map in Fig. 6.15) showed considerably different characteristics. The section starts much further up on the shelf crossing the Greenland slope down to 1900 m. The seafloor is covered by water denser than 27.8 $\frac{kg}{m^3}$ on the shelf and almost over the whole slope (Fig. 6.15). Before, similar sections were observed only further downstream 250 km from the sill and linked to spilling events from the shelf (*Brearley et al.*, 2012). At the location of the working area it was not assumed that water from the shelf contributes to the DSO plume. A theoretical study of particle trajectories suggested recently that very dense water from the shelf area of the DS section circulates on the Dohrn Bank array and spills off the shelf break at (29 - 30)° E (*Koszalka et al.*, 2013). Thus, if water in the density class of the DSO plume spills off the shelf, it would likely mix with ambient modified Atlantic water which is observed close to the seafloor in the upper part of the Greenland slope. This mixing product could either be subsequently entrained in the plume or carried with the plume, thus contributing to the overturning.

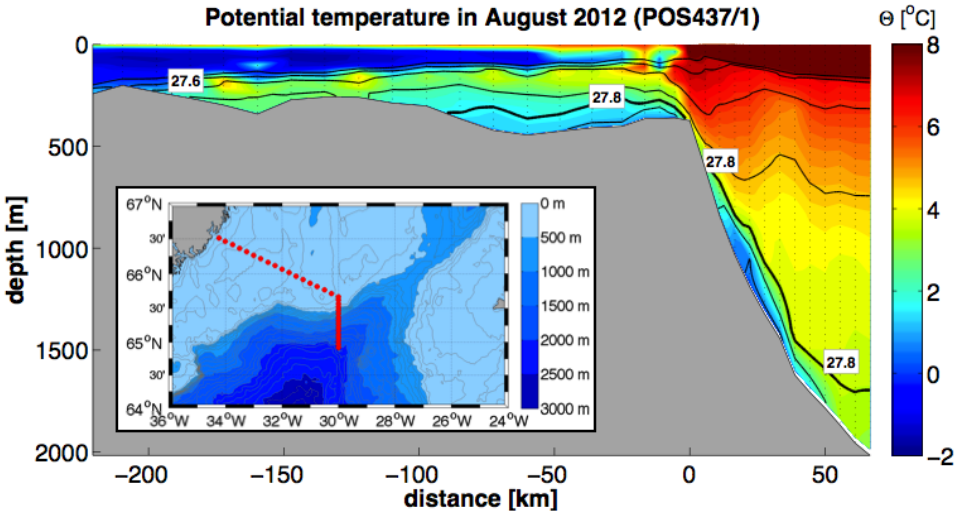

Figure 6.15: Potential temperture section from lowered CTD profiles carried out in August 2012 within the Poseidon cruise POS437/1. Black lines mark the potential density contours. Grey shading marks the Greenland continental shelf and slope. A map showing the location of the CTD section is given in the lower left part of the panel.

Mixing by KH instabilities

In some profiles two sharp gradients and a well-mixed layer are found between the plume and the ambient layer referred to as transition layer (TL) e.g., at station 182 (see Figs. 2.9 (right), and 6.11). This could indicate that an initial sharp interfacial layer has become unstable and created an intermediate layer by KH-instability. The homogeneous transition layer could detach from the plume and mix into the surrounding water column making it colder and less saline.

Enhanced mixing by bottom topography

During dive 2 the AUV collected data in the direct vicinity of an abyssal hill. The hydrographic data shows cold and fresh plume water intruded into the warm, salty ambient water here. This intrusion can most likely be linked to turbulent mixing indicated by dissipation rates of the order $10^{-6}\frac{W}{kg}$ (Fig. 5.6). Lowered CTD/LADCP data indicate an increase in current speed as well as an increase in plume thickness and a cooling of the mixed plume bottom layer during the same time. This can be associated with the passage of a meso-scale eddy (Fig. 6.6) which implies a rise of the plume interface. The observed feature seems to be localized and does not move in space because it is observed in several profiles above each other at varying times. Nevertheless the observed changes in plume characteristics might have caused some of the observed changes. Thus it is challenging to explain the observed feature as a result of vertical resolution problems.

6.5 Summary

The DSO plume characteristics were studied in the working area centered about 180 km downstream of the DS sill across the Greenland slope by many different observational systems. All reveal that the plume is highly variable and a mean state may not be representative for most cases. The moored velocity time series revealed pronounced eddy-driven anomalies exceeding 90 $\frac{cm}{s}$ with periods of 1.6 days.

Both major turbulent events analyzed in chapter 5 can be linked to increasing plume velocities. Together the moored data and data from AUV dive 9 imply that the AUV passed through parts of an eddy. A strong increase in velocity from 0.4 $\frac{m}{s}$ to 1.1 $\frac{m}{s}$ is observed. At the same time the velocity components turn towards the shelf. The hydrographic data show an increase in potential temperature from 1°C to (2 $\pm$ 0.5) °C. Turbulence is indicated by high dissipation rates of O(10^{-6})$\frac{W}{kg}$ and temperature fluctuations observed from the AUV as well as by high fluctuations in the pressure data of the MCs. Additionally strong vertical shear of horizontal velocities and critical Ri numbers in ship-lowered CTD data indicate turbulent vertical mixing. The observations imply that there might be an interaction of horizontal advection of water driven by meso-scale eddies and turbulent vertical mixing, leading to entrainment of ambient water into the DSO plume.

Chapter 7

Conclusion and Outlook

Based on the deployment of a horizontal profiling AUV it was possible to map time and space variability in the DSO plume 180 km downstream from the DS sill. The CTD and MS observations from the AUV provided consistent data with that of ship-lowered CTD/LADCP profiles, moored devices, and a free-falling vertical MSP. The AUV collected profiles in the mixed plume bottom layer, the interfacial layer, and the ambient water above the DSO plume. In order to observe vertical fluxes into the DSO plume it was of interest to sample a long horizontal profile in the interfacial layer. The AUV captured, by chance, an event with high dissipation rates of $\mathrm{O}(10^{-6})\frac{W}{kg}$ in a 4-km-broad segment.

The overall AUV-based dataset (from five successful dives) showed two major events with high fluctuations in hydrographic properties and high dissipation rates of $\mathrm{O}(10^{-6})\frac{W}{kg}$. The first was sampled during dive 2 by covering the vertical DSO plume structure. The second, was sampled during dive 9 while diving through the interfacial layer against the DSO plume for 5 hours. The scales of variability ranged from the lowest observed scales of 13 m, up to 500 m. At these scales, turbulence and internal waves should dominate the motion in the interior ocean. The advantage of horizontal profiling is that it is easier to distinguish between motions in the internal wave subrange and the inertial-convective subrange of turbulence. This is achieved by the use of spectra of isothermal displacements where the spectral slopes vary significantly ($\Phi^{IW}_{d\zeta/dx} \sim k^{-1/2}, \Phi^{IC}_{d\zeta/dx} \sim k^{1/3}$). High variances in the isothermal displacement were found on turbulent scales between 21 and 210 m in the inertial-convective subrange. Internal waves seemed to dominate the motion at less energetic segments. In addition, based on the horizontal profiling, a relation between the integrated spectra (i.e., the variances of temperature or isothermal displacement) and the dissipation was found. This supports the assumption of *Klymak and Moum* (2007a) that dissipation rates can be estimated by horizontal profiling even from a regular CTD. In the future, the fast thermistors from the MSP attached to the AUV should be exploited in the same way as the regular AUV-CTD. Due to higher temporal resolution (512 Hz

acquisition) and better exposure to the water, one should be able to expand the wave number spectra further into the inertial-diffusive subrange of turbulent motion. Another promising method still to be tested is estimating dissipation rates based on the AUV-inferred vertical motion measured by the fast acceleration sensors of the MSP.

In addition to the scales of small-scale variability it was of interest to understand the physical mechanisms initializing the high dissipation rates. Therefore, the DSO plume surroundings were studied. During dive 2 dissipation rates of $O(10^{-6})\frac{W}{kg}$ and cold, and fresh water intruding into to warm ambient water were found in the vicinity of a topographic elevation. The turbulent patch extended horizontally from the base of the topographic feature (on the upstream side) to the location of the highest elevation. Vertically the patch was visible between 50 m to 140 m above the highest point of the topographic elevation. Lowered CTD/LADCP profiles implied an eddy-induced velocity increase during this AUV dive. It is not clear whether the vertical structure of the turbulence changed over time because the DSO plume thickened. Nevertheless, it appears to that the feature did not move horizontally but kept its position on the upstream side of the hill. The topographic elevation was not present in high-resolution satellite-based topographic data sets. If a large number of such undetected elevations with similar possible permanent turbulent patches exist, associated with observed strong vertical fluxes, then they could highly contribute to entrainment by vertical mixing. In order to gain a better insight and test the robustness of the observed feature, there is a need for higher temporally resolved observations in the vicinity of such topographic elevations. If such features are permanent, a higher resolved topography of the Greenland continental shelf is needed to detect similar topographic elevations and estimate the overall contribution of the observed turbulent dissipation to vertical entrainment in the DSO plume.

The second event with AUV-inferred large vertical fluxes was similarly linked to the passage of an eddy. Here the AUV most likely encountered the edge of an eddy. Hydrographic observations showed that the contributions of salinity and temperature in terms of changing the density varied in time. Thus different source waters or entrained ambient water accounted for the observed changes. The dissipation rates of $O(10^{-6})\frac{W}{kg}$ (compared to $O(10^{-9})\frac{W}{kg}$ in the beginning of the dive) and high temperature variances implied turbulent motion in the vertical. Turbulent mixing was also suggested based on the observations of critical Ri numbers, large vertical velocity shear from LADCP profiles, and high frequency fluctuations of pressure data from the moored MCs. In addition, moored velocity data indicated the advection of ambient water towards the shelf. Consequently, both the advection of ambient water and the vertical mixing seemed to interact causing the entrainment of ambient water into the interfacial layer of the DSO plume. In future work based on the two-month-long mooring time series capturing both velocity and hydrographic properties of at least 25 eddies a typical scenario (including space and time

scales) for the exchange between DSO plume and the ambient water could be studied. Additionally it may be possible to derive dissipation rates from the moored ADCP measurements (*Wiles et al.*, 2006). All data should be used to obtain a coherent view of both lateral and vertical exchange between the DSO plume and the surrounding waters during the passage of an eddy. The dissipation rates calculated from the free-falling vertical MSP during MSM21/1b could be analyzed as well with respect to the passage of eddies based on moored and lowered CTD/LADCP data.

The use of an AUV for observations of small-scale variability in the DSO plume succeeded as it was possible to detect turbulent motion in the interfacial layer of the DSO plume. The disadvantage of the AUV measurement system is the missing vertical information. This especially accounts for the variable DSO plume region where it was shown that very large changes on small spatial scales can adjust quickly. For physical interpretation, there is a need for vertical information of the DSO plume conditions and its time evolution during each AUV mission. This was provided by the multi-platform approach used during MSM21/1b. Although it was not possible to provide e.g. stratification data instantaneously for each segment of the AUV track, the large data set enabled to embed the AUV observations into the DSO plume surrounding.

The enhanced vertical fluxes observed by the AUV in the vicinity of a topographic elevation and within the edge of an eddy imply that entrainment by diapycnal fluxes might be patchy in space and time and difficult to observe. This is also indicated by the varying occurrence of low salinity lids on top of the mixed plume. Consequently local estimates of entrainment by vertical fluxes can hardly provide representative estimates of the overall entrainment by vertical diapycnal mixing. Nevertheless, if the observed features can be shown to be robust, they indicate large entrainment of ambient water into the DSO plume by topographic- and/or eddy-induced vertical mixing. In future work it could be studied whether these mechanisms are sufficient to explain the increase in the DSO plume transport on its way downstream from the sill along the Greenland continental slope and, by the inherent water mass transformation, contribute significantly to the deep branch of the AMOC.

Bibliography

Arneborg, L., V. Fiekas, L. Umlauf, and H. Burchard (2007), Gravity Current Dynamics and Entrainment - A Process Study Based on Observations in the Arkona Basin, *Journal of Physical Oceanography*, *37*, 2095–2113.

Bacon, S., and P. Saunders (2010), NOTES AND CORRESPONDANCE. the Deep Western Boundary Current at Cape Farewell: Results from a Moored Current Meter Array, *Journal of Physical Oceanography*, *40*, 815–829.

Brearley, J., R. Pickart, H. Valdimarsson, S. Jónsson, R. Schmitt, and T. Haine (2012), The East Greenland boundary current system south of Denmark Strait, *Deep-Sea Research I*, *63*, 1–19.

Bruce, J. (1995), Eddies southwest of the Denmark Strait, *Deep-Sea Research*, *42*(1), 13–29.

Darelius, E., I. Fer, and D. Quadfasel (2011), Faroe Bank Channel Overflow: Mesoscale Variability*, *Journal of Physical Oceanography*, *41*.

Dickson, B., et al. (2008), The overflow flux west of Iceland: Variability, origins and forcing, in *Arctic-Subarctic Ocean Fluxes: defining the role of the northern seas in climate*, edited by B. Dickson, J. Meincke, and P. Rhines, chap. 19, pp. 443–474, Springer, New York.

Dickson, R., and J. Brown (1994), The production of North Atlantic Deep Water: Sources, rates, and pathways, *Journal of Geophysical Research*, *99*(C6), 12,319–12,341.

Dommenget, D. (2008), An introduction to Statistical Analysis in Climate Research, a script for statistic lecture.

Emery, W., and R. Thomsen (2001), *Data Analysis Methods in Physical Oceanography*, 2 ed., Elsevier Oceanography Series, Amsterdam.

Fer, I., G. Voet, K. Seim, B. Rudels, and K. Latarius (2010), Intense mixing of the Faroe Bank Channel overflow, *Geophyical Research Letters*, *37*(L02604).

Fischer, J., and M. Visbeck (1993), Deep Velocity Profiling with Self-contained ADCPs, *Journal of Atmospheric and Oceanic Technology*, *10*, 764–773.

Fofonoff, N., and R. Millard. (1983), *Algorithms for computation of fundamental properties of seawater*.

Girton, J., and T. Sanford (2003), Descent and Modification of the Overflow Plume in the Denmark Strait*, *Journal of Physical Oceanography*, *33*.

Grant, H., B. Hughes, W. Vogel, and A. Moilliet (1968), The spectrum of temperature fluctuations in turbulent flow, *Journal of Fluid Mechanics*, *34*(3), 423–442.

Hansen, B., S. Østerhus, D. Quadfasel, and W. Turrell (2004), Already the Day After Tomorrow?, *Science*, *305*, 953–954.

Høyer, J., and D. Quadfasel (2001), Detection of deep overflows with satellite altimetry, *Geophyical Research Letters*, *28*(8), 1611–1614.

Johnson, G., J. Toole, and N. Larson (2007), Sensor Corrcetions for Sea-Bird SBE-41CP and SBE-41 CTDs*, *Journal of Atmospheric and Oceanic Technology*, *24*, 1117–1130.

Jungclaus, J., and J. Backhaus (1994), Application of a transient reduced gravity plume model to the Denmark Strait Overflow, *Journal of Geophysical Research*, *99*(C6), 12,375–12,396.

Jungclaus, J., J. Hauser, and R. Käse (2001), Cyclogenisis in the denmark strait overflow plume, *Journal of Physical Oceanography*, *31*.

Käse, R., J. Girton, and T. Sanford (2003), Structure and variability of the Denmark Strait Overflow: Model and observations, *Journal of Geophysical Research*, *108*(C6).

Klymak, J., and J. Moum (2007a), Oceanic Isopycnal Slope Spectra. Part ii: Turbulence, *Journal of Physical Oceanography*, *37*, 1232–1245.

Klymak, J., and J. Moum (2007b), Oceanic Isopycnal Slope Spectra. Part i: Internal Waves, *Journal of Physical Oceanography*, *37*, 1215–1231.

Koehl, A. (2010), Variable source regions of Denmark Strait and Faroe Bank Channel overflow waters, *Tellus*, *62A*, 551–568.

Koszalka, I., T. Haine, and M. Magaldi (2013), Fates and travel times of Denmark Strait Overflow Water in the Irminger basin, submitted by Journal of Physical Oceanography.

Krauss, W. (1996), A note on overflow eddies, *Deep-Sea Research I*, *43*(10), 1661–1667.

Krauss, W., and R. Käse (1998), Eddy formation in the Denmark Strait overflow, *Journal of Geophysical Research*, *103*(C8), 15,525–15,538.

Lueck, R. G. (1990), Thermal Inertia of Conductivity Cells: Theory, *Journal of Atmospheric and Oceanic Technology*, *7*.

Macrander, A., R. Käse, U. Send, H. Valdimarsson, and S. Jónsson (2007), Spatial and temporal structure of the Denmark Strait Overflow revealed by acoustic observations, *Ocean Dynamics*, *57*, 75–89.

Marshall, J., and F. Schott (1999), Open-ocean convection: observations, theory, and models, *Reviews of Geophysics*, *37*(1), 1–64.

Mauritzen, C. (1996), Production of dense overflow waters feeding the North Atlantic across the Greenland-Scotland Ridge. Part 1: Evidence for a revised circulation scheme, *Deep-Sea Research I*, *43*(6), 769–806.

Paka, V., V. Zhurbas, B. Rudels, D. Quadfasel, A. Korzh, and D. Delisi (2013), Microstructure measurements and estimates of entrainment in the Denmark Strait overflow plume, *Ocean Science Discussions*, *10*, 1067–1098.

Quadfasel, D., and R. Käse (2007), Present-Day Manifestation of the Nordic Sea Overflow, in *Ocean Circulation: Mechanisms and Impacts - Past and Future Changes of Meridional Overturning*, edited by A. Schmittner, J. C. H. Chiang, and S. R. Hemming, pp. 75–89, Geophys. Monogr. Ser., Washington, D. C.

Rudels, B., P. Eriksson, H. Grönvall, R. Hietala, and J. Launiainen (1999), Hydrographic Observations in Denmark Strait in Fall 1997, and their Implications for the Entrainment into the Overflow Plume., *Geophyical Research Letters*, *26*(9), 1325–1328.

Rudels, B., E. Fahrbach, J. Meincke, G. Budéus, and P. Eriksson (2002), The East Greenland Current and its contribution to the Denmark Strait overflow, *ICES Journal of Marine Science*, *59*, 1133–1154.

Schmittner, A., J. C. H. Chiang, and S. R. Hemming (2007), Introduction: The OceanÕs Meridional Overturning Circulation, in *Ocean Circulation: Mechanisms and Impacts - Past and Future Changes of Meridional Overturning*, edited by A. Schmittner, J. C. H. Chiang, and S. R. Hemming, pp. 1–4, Geophys. Monogr. Ser., Washington, D. C.

Schott, F., and P. Brandt (2007), Circulation and Deep Water Export of the Subpolar North Atlantic, in *Ocean Circulation: Mechanisms and Impacts - Past and Future Changes of Meridional Overturning*, edited by A. Schmittner, J. C. H. Chiang, and S. R. Hemming, pp. 91–118, Geophys. Monogr. Ser., Washington, D. C.

Schott, F., R. Zantopp, L. Stramma, M. Dengler, J. Fischer, and M. Wibaux (2004), Circulation and Deep-Water Export at the Western Exit of the Subpolar North Atlantic, *Journal of Physical Oceanography*, *34*.

Seim, K., I. Fer, and J. Berntsen (2010), Regional simulations of the Faroe Bank Channel overflow using σ-coordinate ocean model, *Ocean Modelling*, *35*, 31–44.

Simpson, J., and J. Sharples (2012), *Introduction to the Physical and Biological Oceanography of Shelf Seas*, 1 ed., Cambridge University Press, New York.

Spall, M., and J. Price (1997), Mesoscale Variability in Denmark Strait: The PV Outflow Hypothesis*, *Journal of Physical Oceanography*, *28*.

Stahr, F., and T. Sanford (1998), Transport and bottom boundary layer observations of the North Atlantic Deep Western Boundary Current at the Blake Outer Ridge, *Deep-Sea Research II*, *46*, 295–243.

Tanhua, T., K. A. Olsson, and E. Jeansson (2005), Formation of Denmark Strait Overflow water and its hydro-chemical composition, *Journal of Marine Systems*, *57*, 264–288.

Thorpe, S. (2005), *The Turbulent Ocean*, 13 978-0-521-83543-5, 1 ed., Cambridge University Press, New York.

Torrence, C., and G. Compo (1998), A practical guide to wavelet analysis, *Bull. Amer. Meteor. Soc.*, *79*, 61–78.

Våge, K., et al. (2011), The Irminger Gyre: Circulation, convection, and interannual variability, *Deep-Sea Research I*, *58*, 590–614.

Voet, G., and D. Quadfasel (2010), Entrainment in the Denmark Strait overflow plume by meso-scale eddies, *Ocean Science*, *6*, 301–310.

Whitehead, J. (1998), Topographic control of oceanic flows in deep passages and straits, *Reviews of Geophysics*, *36*(3), 423–440.

Wiles, P., T. Rippeth, J. Simpson, and P. Hendricks (2006), A novel technique for measuring the rate of turbulent dissipation in the marine environment, *Geophyical Research Letters*, *33*(L21608).

Appendix

List of acronyms

AAW	Arctic Atlantic Water
ADCP	Acoustic Doppler Current Profiler
AIW	Arctic Intermediate Water
AMOC	Atlantic Meridional Overturning Circulation
AUV	autonomous underwater vehicle
AW	Atlantic Water
BL	bottom layer
CTD	conductivity-temperature-depth
DS	Denmark Strait
DSO	Denmark Strait Overflow
DSOW	Denmark Strait Overflow Water
DVL	Doppler Velocity Log
DWBC	Deep Western Boundary Current
EGC	East Greenland Current
FBC	Faroe Bank Channel
GPS	Global positioning system
IL	interfacial layer
INS	inertial navigation system
ISOW	Iceland-Scotland Overflow Water
LADCP	lowered ADCP
LBL	long baseline
LSW	Labrador Sea Water
MC	MicroCAT
MIW	Middle Irminger Water
MS	microstrucure
MSP	microstructure profiler
NADW	North Atlantic Deep Water
PIW	Polar Intermediate Water
PS	power spectrum
PSD	power spectral density
RAW	Re-circulating Atlantic Water
std	standard deviation
T	temperature
TKE	turbulent kinetic energy
S	salinity
TL	transition layer
uPDW	upper Polar Deep Water
UH	University Hamburg

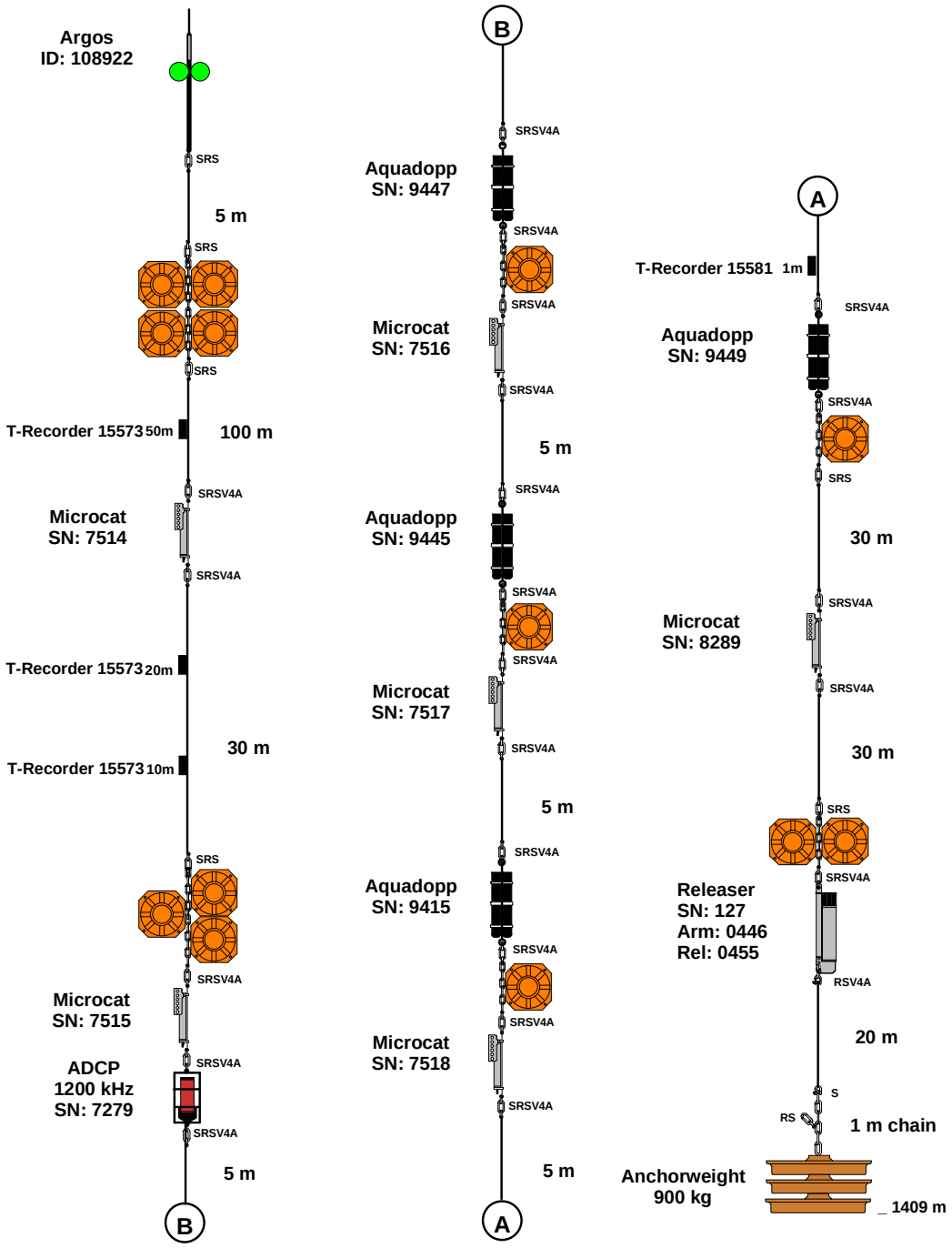

DS 19-12 Aquadopp Institut für Meereskunde Universität Hamburg	Ship : MS Merian	Cruise : MSM 21-1b
	Date : 16.06.12	Lat : 65° 14.357 N
	Depth: 1409 m	Long : 029° 57.542 W

Mooring design DS19

Acknowledgements

Foremost, I would like to express my sincere gratitude to my advisor Prof. Torsten Kanzow for the continuous support of my Master thesis. Many thanks for providing me with this topic, for the excellent supervision, for all of the input and for the continuous interest in my thesis. Your door was always open for me and you spent so much time bringing this work on the right track. I learned a lot.

Likewise, many thanks to Kerstin Jochumsen, Sandra Tippenhauer, and Nuno Nunes for providing data, Gerd Krahmann, and Johannes Hahn for the technical assistance, and Marcel Rothenbeck, for showing me the AUV.

The manuscript benefited from comments of Kerstin Kretschmer, Stacy Buschhaus, and Gunnar Pipa, Thanks to all of you.

Erklärung

Hiermit erkläre ich, dass ich die vorliegende Arbeit selbständig und ohne fremde Hilfe angefertigt und keine anderen als die angegebenen Quellen und Hilfsmittel verwendet habe. Die eingereichte schriftliche Fassung der Arbeit entspricht der auf dem elektronischen Speichermedium. (Name der Datei: Master_Thesis_Janin_Schaffer.pdf)

Weiterhin versichere ich, dass diese Arbeit noch nicht als Abschlussarbeit an anderer Stelle vorgelegen hat.

Datum, Unterschrift